Fast Scanning Calorimetry Studies of Deeply Supercooled Water and Aqueous Solutions

by Stephanie Anne McCartney

B.S. Chemistry, December 2003, University of Georgia
M.Phil. in Chemistry, May 2007, The George Washington University

A Dissertation submitted to

The Faculty of
Columbian College of Arts and Sciences
of The George Washington University
in partial fulfillment of the requirements
for the degree of Doctor of Philosophy

August 31, 2009

Dissertation directed by

Vladislav Sadtchenko

Associate Professor of Chemistry

The Columbian College of Arts and Sciences of The George Washington University certifies that Stephanie A. McCartney has passed the Final Examination for the degree of Doctor of Philosophy as of May 14, 2009. This is the final and approved form of the dissertation.

Fast Scanning Calorimetry Studies of Deeply Supercooled Water and Aqueous Solutions

Stephanie Anne McCartney

Dissertation Research Committee:

Vladislav Sadtchenko, Associate Professor of Chemistry, Dissertation Director

David Ramaker, Professor of Chemistry, Committee Member

Michael Wagner, Associate Professor of Chemistry, Committee Member

© Copyright 2009 by Stephanie Anne McCartney
All rights reserved

Dedication

To Mommy and Daddy for all the encouragement growing up

To Craigie for all the jokes about being mad crazy…not mad angry

To Donnie for his love and support, without which this would not have been completed

Acknowledgements

Although this dissertation is the culmination of five years of hard work, I could not have succeeded without the help of many great people.

First, I have to thank my parents. Since the day I was born, they have always instilled in me the belief that I have the ability to do anything. They have supported, pushed, and cheered me in all of my endeavors. I know that without them I would not have made it this far.

Next, I need to thank my husband. Donnie has always given me unconditional love and encouragement. He was and is always there to listen and help me de-stress. I can't imagine how I would have ever gotten through the past five years without him.

After I arrived at GWU I met a lot of people that helped me along the way. Shanna Roth became a good friend that would help me jump through all of the administrative red tape. Gary Reynolds was always there to guide me through the money maze when trying to allocate purchases to the correct funding sources. William (Bill) Rutkowski from the Machine Shop always took the time to help me make the intricate parts necessary for improving my experimental apparatus.

The various faculty members in the Chemistry Department also helped me to grow as a chemist and a teacher. Joan Hilderbrandt and Professor Michael Wagner gave me insights into how to become an effective teacher by gaining and maintaining the students' interest without compromising the essence of the material being taught. My candidacy exam committee, Professor David Ramaker and Professor Wagner, were influential in

helping me to expand my base knowledge in order to more fully understand the scope of my research.

I also want to acknowledge my lab mates in the Sadtchenko group. Meshe Chonde was "instrumental" in teaching me how to use the experimental apparatus. Danielle Smyla was helpful in early FTDS studies. Dr. Haiping Lu was the best lab partner that I could've hoped for to help me through my experimental studies. Together we performed experiments, crunched data, wrote journal articles, presented posters, and supported each other through our time at GWU.

Finally, I must thank my research advisor, Professor Vlad Sadtchenko. Over the past five years, Vlad has guided me through the rigors of grad school. With his patience and understanding, I have grown from simply being a student learning chemistry to a research scientist trying to understand some of the fundamental properties of water.

Dissertation Abstract

Fast Scanning Calorimetry Studies of Deeply Supercooled Water and Aqueous Solutions

This dissertation describes the results of extensive Fast Scanning Calorimetry (FSC) studies of the fundamental properties of amorphous solid water (ASW).

Motivation for fundamental studies of condensed aqueous phases, modern experimental approaches, and current terminology and theories relevant to liquids and glasses are described in Chapter 1. Chapter 2 provides an in-depth description of the experimental apparatus, along with the basic experimental procedures and critical tests. Chapters 3, 4, 5, and 6 report the essential findings of the research.

Chapter 3 describes the results of FSC experiments designed to establish quantitative relationships between the kinetic parameters of supercooled liquids (the microscopic relaxation time) and the experimental variables (the heating rate). The dynamic glass transition temperature of 1.0 ± 0.5 micrometer thick films of 1-propanol, toluene, pentanol, decalin, and 2-ethyl-1-hexanol was measured by the FSC at a heating rate of 10^5 K/s. When compared with the corresponding temperature values derived from dielectric spectroscopy data, the glass transition temperatures correlated within a few degrees for both techniques. Thus, the central assumption of the FSC approach, i.e., the assumption that the inverse of the heating rate is equal to the relaxation time at the temperature where the glass transition is observed, was validated.

In Chapter 4, the FSC was employed to investigate the glass transition phenomena in vapor deposited amorphous solid water (ASW) films doped with acetic acid, pentanol, ethanol, and carbon tetrachloride. In all four cases, the FSC thermograms of doped ASW films show well pronounced glass transitions at temperatures near 177 K. Systematic FSC measurements of the glass transition temperature and the excess heat capacity dependence on the concentration of impurities indicate the possible existence of two distinct non-crystalline phases of H_2O in binary aqueous solutions. According to our conjecture, bulk pure ASW is a glass at temperatures up to its crystallization at temperatures near 205 K. However, a guest molecule in the ASW matrix may be enveloped in ultraviscous liquid water at temperatures as low as 136 K. In the case of CH_3COOH, we estimate that such a viscous shell contains approximately 25 H_2O molecules. I discuss the implications of these findings for past studies of molecular kinetics in pure vitreous water and in binary aqueous solutions.

Chapter 5 presents and discusses the results of FSC experiments utilized to investigate the glass transition phenomena in ~2 μm thick ASW films doped with a 0.1 molar ratio of CH_3COOH with heating rates varying from 5 kK/s to 650 kK/s. Increasing the heating rate resulted in a significant shift in the onset temperature of the glass transition from 155 ± 3 K to 178 ± 3 K, as well as an increase in the glass endotherm magnitude (ΔC_p). The microscopic relaxation times (τ_h) derived from the inverse of the heating rates were $2 * 10^{-4}$ s, $4 * 10^{-5}$ s, $8 * 10^{-6}$ s, $1.5 * 10^{-6}$ s. The dependence of these τ_h's with temperature closely follows an Arrhenius dependence with an apparent activation energy of 55 ± 2 kJ/mol. Furthermore, the temperature dependence of specific heat capacity at

constant pressure derived from the glass endotherms of doped ASW coincides with that of supercooled water in silica nanopores. Based on the Adams-Gibbs analysis of these results, I argue that the impact of impurities on the molecular kinetics in supercooled water is similar to that of nanopore confinement and that it can be rationalized in terms of limitations imposed on water's cooperative rearrangement scale by dopant species. In the context of these conclusions and their analysis, I also discuss a possible explanation for the sporadically observed endothermic features in some DSC studies of supposedly pure vitreous water samples.

In Chapter 6, variable rate FSC was used to estimate the characteristic crystallization time (τ_{CR}) of ASW during rapid heating with rates from $3 \cdot 10^3$ K/s to $1.6 \cdot 10^6$ K/s. The resulting dependence of τ_{CR} on temperature conforms to Arrhenius Law with an apparent activation energy of 68 ± 2 kJ/mol. Furthermore, the τ_{CR} values derived from variable rate FSC measurements can be connected to similar data obtained in past studies at temperatures ranging from 130 K to 150 K via the same Arrhenius dependence. Based on this observation, I argue that pure ASW is a strong (glassy) phase over the entire temperature range from the singularity point (228 K) down to cryogenic temperatures.

Table of Contents

Dedication iv

Acknowledgements v

Dissertation Abstract vii

Table of Contents x

List of Figures xiv

Chapter 1: Introduction 1

1.1 Experimental Research on Fundamental Physics and Chemistry of Condensed Aqueous Phase: Utility and Challenge 1

1.2 New Approach to Studies of Physics and Chemistry of Condensed Aqueous Phase 4

1.3 Supercooled Liquids and Glasses: Essential Agreed Upon Views and Definitions 7

1.3.1 Nature of Supercooled Liquids and Glasses from Thermodynamic Standpoint: Kauzmann's Ideal Glass Hypothesis 8

1.3.2 Nature of Supercooled Liquids and Glass from a Practical (Laboratory) Standpoint: Laboratory Glass and Laboratory Glass Transition 11

1.3.3 Strong and Fragile Liquids: Dependence of Microscopic Kinetic Parameters on Temperature 15

1.3.4. Amorphous Solids 18

1.3.5 Characteristic Crystallization Time of a Supercooled Liquid 19

1.3.6 Anatomy of a Fast Scanning Calorimetry Experiment 22

1.4 Studies of Deeply Supercooled Water: A Key to the Understanding of Water Structure and Dynamics 25

References 33

Chapter 2: Experimental Techniques: Fast Scanning Calorimetry 44

2.1 Experimental apparatus 44

2.1.1 Outline 44

2.1.2 Detector 46

2.1.3 Vapor Deposition System 49

2.1.4 Data Acquisition and Process Control System 51

2.2 Fundamentals of a Fast Scanning Calorimetry Experiment: Technique Demonstration and Critical Tests 55

2.3 Brief Summary and Conclusions 67

References 68

Chapter 3: Fast Scanning Calorimetry Studies on the Enthalpy Relaxation Time of Vitreous Molecular Solids 69

3.1 Introduction 69

3.2 Enthalpy Relaxation Time of Vitreous Molecular Solids 70

3.3 Widths of Glass Endotherms 78

3.4 Summary 78

References and Notes 80

Chapter 4: Fast Scanning Calorimetry Studies of the Glass Transition in Doped Amorphous Solid Water: Evidence for the Existence of a Unique Vicinal Phase 81

4.1 Introduction 81

4.2 Results and Discussion 88

4.2.1 FSC Thermograms of Doped ASW 88

4.2.2 Interpretation of the FSC Thermograms of Doped ASW from the Standpoint of the Cooperative Domain Theory 96

4.2.3 Vicinal ASW Hypothesis 99

4.2.4 Extrapolation of T_g for Pure ASW from Past Solution Studies 103

4.3 Summary and Afterword 106

References 107

Chapter 5: Insights into the Physical Nature of Vicinal Amorphous Solid Water from Variable Rate Fast Scanning Calorimetry 110

5.1 Introduction 110

5.2 Experimental Arrangement and Results 111

5.3 Variable Rate FSC Thermograms of ASW Doped with Acetic Acid 114

5.4 Temperature Dependence of the Enthalpy Relaxation for Highly Perturbed ASW 118

5.5 Analysis of the Relaxation Data Based on the Adam–Gibbs Theory 120

5.6 Heat Capacity of Vicinal ASW at Various Temperatures 126

5.7 Molecular Structure and Dynamics in ASW in the Case of Low Concentration of Impurities 129

5.8 Origins of Weak Endothermic Features in Conventional DSC Thermograms Observed at 137 K 133

5.9 Summary 136

References 137

Chapter 6: Variable Rate Fast Scanning Calorimetry Studies of Pure Amorphous Solid Water Crystallization 138

6.1 Introduction 138

6.2. Experimental Arrangement 139

6.3 Analysis and Discussion 140

6.4 Summary and Afterword 150

References 152

Chapter 7: Conclusions and Future Research Projects 153

List of Figures

Figure 1.1. The number of scientific articles published over the last several years that take into account aqueous phase physics and chemistry. 2

Figure 1.2. The essential steps involved in a basic FTDS-FSC experiment. 6

Figure 1.3. The entropy of a stable liquid decreases with temperature up to its freezing/melting point, where it undergoes a first order phase transition to form a crystalline solid (blue line). When the crystallization of a liquid is suppressed and its temperature is lowered past $T_{melting}$, it is considered a supercooled liquid. The entropy of this state is represented by a linear extrapolation of the entropy of the thermodynamically stable liquid (dashed line). As this line extends, it approaches the entropy of the crystalline state and becomes equal at the Kauzmann temperature, T_K. This temperature marks the greatest degree of supercooling achievable by any stable liquid, which is termed a "glass" under these conditions. 9

Figure 1.4. Top panel: As a stable liquid is lowered past $T_{melting}$, it enters a supercooled state. Based on the observation time, it appears as though the configurational entropy of the liquid's constituents continues to decrease up to a certain temperature, T_g, at which point the configurational entropy appears to be temperature invariant. Bottom panel: As the kinetics of the liquid's constituents (molecules, atoms, etc.) slow down, there is a decrease in the heat capacity of the liquid. At the point where the observation time becomes shorter

than the microscopic relaxation time, there is a sudden drop in heat capacity at T_g. The temperature at which this drop occurs is dependant upon the length of the observation time of the experimental technique. 14

Figure 1.5. The kinetic parameters of a "strong" liquid demonstrate an Arrhenius dependence with temperature (straight arrow); whereas, the kinetic parameters of a "fragile" liquid do not exhibit such a dependence (curved arrow). It the case of water, it is suggested that there may be a "fragile-to-strong" crossover (dashed arrow) based on the rate of its microscopic relaxation time. 17

Figure 1.6. Temperature dependence of the crystallization time (τ_{CR}) for a supercooled liquid. At temperatures just below $T_{melting}$, τ_{CR} is infinitely slow, due to a high Gibbs free energy barrier. As the temperature continues to decrease, this energy barrier decreases; thereby, allowing crystallization to occur faster. If the temperature is cooled to cryogenic temperatures, then the slowdown in constituent kinetics leads to an infinite increase in the crystallization time (slower crystallization). 20

Figure 1.7. Top panel: Heating a laboratory glass at a finite rate initially resembles crystal-like entropy. As the configurational rearrangement of the glass' constituents "unfreezes," the entropy of the glass increases quickly to match that of a deeply supercooled liquid (T_{g1}). Since the experimental observation time decreases with an increasing heating rate, the temperature of the glass transition measured with a higher heating rate manifests at a higher temperature (dotted line, T_{g2}). As the temperature continues to increase, the characteristic

crystallization time of the liquid becomes comparable to the experimental observation time, causing the entropy to drop to that of the liquids crystalline solid. Again the temperature at which the crystallization occurs is dependant upon the heating rate. Bottom panel: The heat capacity of a laboratory glass initially follows that of its crystalline solid up to the point of its glass transition. The glass transition appears as an endothermic feature on the thermogram. As the temperature of the supercooled liquid continues to increase, the liquid crystallizes, which results in an exothermic feature on the thermogram. 23

Figure 1.8. The essential features of an FSC thermogram (glass transition temperature, crystallization, etc.) are observed when experimental observation time becomes equal to the microscopic relaxation time (T_g) or the characteristic crystallization time (T_{CR}). During a slow scan rate, the temperature of the glass transition (T_{g1}) and crystallization (T_{CR1}) are lower than their corresponding temperatures (T_{g2} and T_{CR2}) from a faster scan rate..... 26

Figure 1.9. Two opposing hypotheses about the properties of water over the temperature range known as "No Man's Land" (160 K – 235 K). Type I (dotted line) illustrates the continuity conjecture, which assumes water is a fragile liquid over the entire temperature range from cryogenic to ambient. Type II (dashed line) illustrates a counter hypothesis that postulates that water undergoes an anomalous transition from a fragile to a strong liquid in the vicinity of T_s (228 K). 28

Figure 2.1. The outline of the experimental apparatus. The calorimeter consists of a filament array which is mounted on a LN-cooled support block. The ends of the filament are clamped between flat resistive heaters and 0.5 mm thick sapphire plates. The temperature of the filament support assembly is measured with two T-type thermocouples. The calorimeter is situated inside a high vacuum chamber that maintains a pressure of $5 * 10^{-7}$ Torr. A QMS is ~10 cm above the filament array measures the vaporization fluxes of volatiles during experiments..... 45

Figure 2.2. The mass spectrum of water. 47

Figure 2.3. The detector signal obtained for an ASW film doped with CH_3COOH. The ratio of water molecules to acetic acid molecules can be calculated by integrating the area under the curves and dividing the values. 48

Figure 2.4. The outline of the vapor deposition system. This system consists of two independent stainless steel tubes terminated by solenoid valves. The valves are positioned 4 cm above the filament array. The vapor sources for each line are vials filled with volatile liquids and maintained at a temperature of 14 °C. Each vial is also connected to a mechanical pump via a LN trap to ensure that the vapor source is constantly pumped during all stages of the experiment. In the case of ASW films doped with miscible volatile liquids, the vapor line is connected to a glass bulb containing a pre-mixed dopant/water solution. In the case of ASW films doped with immiscible volatile liquids, a separate vapor

source is utilized to co-deposit water vapor with the immiscible liquid vapor directly onto the filament..... 50

Figure 2.5. The outline of the data acquisition and process control system (DAQPC). An experiment begins when the vapor deposition time and sequence are input into the LabView program on the PC. The valve drivers of the vapor deposition system are engaged by several timed TTL pulses from the DAQ board. Upon completion of the film deposition, the FSC scan is initiated by a TTL trigger pulse to a standalone pulse generator. The generator closes the electronic switch of the filament circuit and sends an electric current through the filament. After the ASW film vaporizes, the voltage, current, and QMS signals are collected by the DAQ and sent to the PC..... 52

Figure 2.6. The schematic of the electronic switch and current measurement circuit. The electronic switch is essentially comprised of two pnp transistors, whose primary base input is terminated with a 10 kΩ resistor. The current measurement sensor in the circuit is designed around a single operational amplifier (TI OpAmp 749 or similar), which is utilized to monitor the voltage drop across a 0.5 Ω shunt resistor (R_{sense}). The current and voltage waveforms from the filament are sent to a differential analog input of the DAQ board and are stored in the on-board memory buffer after analog-to-digital (ADC) conversion..... 54

Figure 2.7. The current (upper panel) and voltage (lower panel) data collected for a 1 μm thick ASW film that was desorbed using a heating rate of 10^5 K/s..... 56

Figure 2.8. Using Ohm's Law and its corollary (Equation 2.1), the current and voltage data (from Figure 2.7) can be used to calculate the resistance and temperature of the film/filament system. 58

Figure 2.9. Resistance and corresponding temperature of the filament during rapid heating. The solid line shows resistance of the filament covered by a 1 μm thick ASW film. The resistance of an ice-free filament is shown for comparison. In the case of the ice-covered filament, the heating rate is lower, and the heating curve shows a number of inflection points indicative of multiple exo- or endothermic transitions in the ASW film/filament system. The data demonstrate that heating rates up to 105 K/s are easily accessible with the experimental setup and that the sensitivity of the calorimeter is sufficient to detect exo- and endothermic transitions in thin films of amorphous ice used in our experiments.... 60

Figure 2.10. The effective heat capacity of the bare filament and an ice film vapor deposited at 120K and, then, annealed by raising the temperature to 240 K for 5 ms. The data obtained from heat capacity thermograms makes it possible to obtain a good estimate of the ice film's overall thickness and mass. For this particular thermogram, the film was 2.2 ± 0.3 μm thick. 63

Figure 2.11. FSC thermograms of vapor deposited ASW films prepared under various conditions. The heating rate is (1.3 ± 0.2) *10^5 K/s. The mass of all three films is nearly identical and corresponds to a film thickness of 1.0 ± 0.1 μm. Lower panel: the thermogram of an ASW film vapor deposited at 110 K. Middle panel: the thermogram of ASW film vapor deposited at 140 K. Top panel: the

thermogram of a film deposited at 170 K. The endothermic upswing in the heat capacity at temperatures above 250 K, present in all three thermograms, is due to the onset of the rapid desorption..... 64

Figure 2.12. Heat capacities of ASW (solid line) and crystalline (dotted line) ice films of nearly identical mass (the accuracy of relative measurements of ice sample mass is better than 3%). The deposition temperature was 140 K and was chosen to ensure complete relaxation of strained ASW sample without its extensive crystallization. The most important feature of the thermogram is the near match in the heat capacities of the crystalline and the ASW samples up to the temperature of ASW crystallization. 66

Figure 3.1. USC thermograms of toluene measured at three distinct rates. The thickness of toluene films was 1.0 ± 0.5 micrometers. The temperature of the onset of the glass transition was determined from the intersection of the dashed line. As shown in the figure, higher heating rates result in higher temperature of the glass transition..... 71

Figure 3.2. Relaxation data obtained by several techniques. Solid diamonds represent the relaxation times calculated as the inverse of the heating rates used for each of the toluene thermograms in Figure 3.1. The figure also shows the dielectric relaxation data (solid circles), deuteron spin-lattice relaxation data (open squares) as well as the relaxation data from microwave spectroscopy (solid squares). The dotted line describes the temperature dependence of τ_h obtained from diffusion and viscosity data, as well as that from deuteron spin alignment

(open circles and crosses) data. Note that the figure was constructed from Figure 4 of Reference 2. 72

Figure 3.3. FSC thermograms of several organic glass-formers. Thin (0.5 – 1.5 μm) films were vapor-deposited on the surface of the tungsten filament at 10 – 20 degrees above their standard glass transition temperatures to ensure formation of a well-annealed, low enthalpy layers. After deposition, the temperature of the films was lowered to 120 K and a rapid calorimetry scan was initiated. The intersections of dotted lines designate the dynamic glass transition temperatures, i.e., the temperatures where the enthalpy relaxation time reaches the value numerically equal to the inverse of the heating rate. The standard glass transition temperatures, i.e., those obtained in conventional DSC experiments, are listed under the name of each compound along with the heating rate of the FSC scan. 74

Figure 3.4. Relaxation time data for several organic glass-formers. The data shown in this figure was taken from a myriad of different dielectric spectroscopy studies (References 2 – 6). The dotted line originating at 10^{-5} s is the inverse of the typical heating rate (10^{5} K/s); therefore, the point at which the dotted line intersects with the data is the temperature of the expected glass transition using FSC..... 76

Figure 3.5. Correlation between the dynamic glass transition temperatures from FSC thermograms and those derived from the dielectric spectroscopy data. The points represent temperatures where the dielectric relaxation time is numerically

equal to the inverse of the heating rate of the corresponding FSC scan. The horizontal bars mark the temperature range where the dielectric relaxation time is within an order of magnitude of the value numerically equal to the inverse of the heating rate of the corresponding FSC scan. With the exception of pentanol, the dynamic glass transition temperatures in FSC scans deviate from those derived from the dielectric spectroscopy data by less then five degrees. 77

Figure 4.1. Two opposing interpretations of the state of water over the entire temperature range from cryogenic to ambient. The continuity conjecture (dotted line) follows the VFT equation where the Vogel temperature is 124 K. According to the continuity conjecture, water is assumed to be a fragile liquid at any temperature above 136 K. An alternate viewpoint (solid line) assumes a fragile-to-strong transition in the vicinity of 228 K (T_s). 82

Figure 4.2. Fast scanning thermograms of pure (dotted) and doped (solid) ASW samples deposited under nearly identical conditions. Pure ASW does not undergo a glass transition at temperatures below 200 K, where it crystallizes. When doped with acetic acid, ASW shows a well pronounced glass transition at 177 ± 5 K. 85

Figure 4.3. According to the continuity hypothesis (dotted line), a glass transition for pure water should be observed around 175 K when using a heating rate of 10^5 K/s. The grey circle represents the glass transition observed from the doped-ASW film from Figure 4.2. In this case, the continuity hypothesis is consistent,

but only in the case of heavily doped ASW and, therefore, cannot be correct for pure ASW. 86

Figure 4.4. FSC thermograms of ASW doped with varying molar fractions of acetic acid. Each thermogram corresponds to a doped ASW film that is approximately 1 μm thick. The films were grown using co-deposition of water with acetic acid at 128 ± 2 K and measured at a heating rate of 10^5 K/s. A cursory comparison shows that T_g increases and the magnitude of the endothermic upswing decreases in the case of more dilute CH_3COOH/H_2O films. 89

Figure 4.5. FSC thermograms of ASW doped with acetic acid, pentanol, ethanol, and carbon tetrachloride, respectively. Each thermogram corresponds to a doped ASW film that is 1-2 μm thick. The films were grown using a molar fraction of dopants near 0.04 for each impurity and measured at a heating rate of $5 \cdot 10^4$ K/s. Despite the use of such distinct chemical species as dopants, each thermogram shows a well pronounced glass transition at 177 ± 3 K. 91

Figure.4.6. A FSC thermogram of a dilute solution of CH_3COOH (top panel), an FSC thermogram of a strong CH_3COOH solution (middle panel), and an FSC thermogram of nearly pure vitreous CH_3COOH (lower panel). The estimated concentrations are shown next to each thermogram. 93

Figure 4.7. The FSC thermograms of dilute pentanol/ASW samples and pure pentanol films. As shown in figure, pure $C_5H_{11}OH$ films undergo a glass transitions at temperatures more than 30 degrees lower than $C_5H_{11}OH$ doped ASW films during rapid scans. 94

Figure 4.8. Illustration of the vicinal glass transition hypothesis. According to the hypothesis, FSC thermograms reflect a linear combination of the heat capacities from the fragile liquid which surrounds each dopant molecule (vicinal ASW – dotted line), and from the strong glass of the bulk (unperturbed ASW – dashed line). A gradual increase in the concentration of impurities leads to a linear increase in the fraction of vicinal ASW, so long as the solvation shells surrounding each molecular impurity do not overlap. This increase results in a linear increase in ΔC_P and a constant T_g. In the limit of high concentration of impurities, the solvation shells begin to overlap, resulting in "strongly perturbed" ASW (bold, solid line). 102

Figure 4.9. *Top panel:* The relative magnitude of the endothermic upswing ($\Delta C_P/C_p$) from doped ASW films as a function of molar fraction of acetic acid to water. In the limit of low concentrations, ΔC_P is directly proportional to the mole fraction of CH_3COOH. As the molar fraction increases beyond 0.04, the relative endothermic upswing approaches its maximum value of approximately 0.9. *Lower panel:* The glass transition temperature of doped ASW films as a function of molar fraction of acetic acid to water. As the concentration of CH_3COOH is reduced from 0.18 to 0.04, T_g increases from 167 ± 2 K to 177 ± 2 K. In the limit of low concentrations, i.e., less than 0.04 mole fraction, the glass transition temperature approaches its maximum value of 177 ± 3 K. 104

Figure 5.1. Heating curves of a ~2 μm ASW films from variable rate FSC experiments. By systematically changing the biasing voltage from 2V to 9V

across the filament, the heating rates were varied from 5 kK/s to 650 kK/s; thereby, varying the onset and duration of crystallization of the ASW film. 113

Figure 5.2. Thermogram of a ~2 μm CH3COOH-doped ASW film from a heating rate of approximately 5 kK/s (black line) and the average of thirteen thermograms of similar films, all using the same heating rate (white line). The average of the 13 scans made it possible to sufficiently improve the S/N ratio in order to more accurately determine the onset of the glass transition (T_g) to be 155 ±3 K and the jump in the endothermic upswing (ΔC_p) to be 0.4 ± 0.2 μJ/K. 116

Figure 5.3. Thermograms of ~2 μm CH_3COOH-doped ASW films with heating rates varying from 25 kK/s to 600 kK/s. This increase in the heating rate results in a significant shift in the onset of the temperature of the glass transition from approximately 155 K to near 178 K and an increase in the value of ΔC_p. 117

Figure 5.4. Dependence of the enthalpy relaxation time of ASW films doped with 0.1 mole fraction CH_3COOH (black circles) and a value derived from DSC thermograms for bulk vitreous H_2O phase that was assumed to be "pure vitreous water" (open circle) on temperature. The values of the enthalpy relaxation time are assumed to be numerically equal to the inverse of the heating rate. The ASW points closely follow Arrhenius law and have an apparent activation energy of 55 ± 2 kJ/mol. Furthermore, the Arrhenius fit of the FSC data, when extrapolated to 137 K, gives values of the enthalpy relaxation times, which are close to those derived from DSC measurements of supposedly pure water. 119

Figure 5.5. The Adams-Gibbs theory (AGT) of confinement. As the temperature of a bulk liquid increases, its relaxation time decreases to fit a Vogel-Fulcher-Tammann (VFT) equation and exhibits a strong, non-Arrhenius variation as the temperature approaches the liquid's postulated standard glass transition. In the case of a confined liquid, the relaxation time decreases identically to that of a "free" bulk liquid up to the "cut off" temperature, at which point the cooperative domain of the liquid's molecules reaches its maximum possible confinement and results in a strong Arrhenius behavior. 123

Figure 5.6. Comparison of the enthalpy relaxation time values of ASW films doped with a 0.1 mole fraction of CH_3COOH (black circles) with the dielectric relaxation time data of bulk, pure water at ambient temperatures (open circles). The doped ASW exhibits a strong Arrhenius behavior with an activation energy of 55 ± 5 kJ/mol (dotted line). The solid line represents the power law fit of the dielectric spectroscopy data. According to the Adams-Gibbs theory, the size of the cooperatively rearranging domains in our CH_3COOH doped ASW is expected to be between 8 and 3 molecules, which is similar to those of water confined to nanoscale dimensions (nanopores). 124

Figure 5.7. Thermogram comparing the heat capacities of doped ASW films employed in FSC studies (black circles) with the heat capacity of water confined in silica gel nanopores ranging from 3 to 50 nm (blue circles) and that of polycrystalline ice (dashed line). The most striking feature is the close match between the doped ASW films and that of the pure, confined water, which leads to the

conclusion that the addition of dopants in the ASW matrix impacts the structure and kinetics of ASW in ways that are similar to those characteristic of nanoconfined water. 127

Figure 5.8. The Adams-Gibbs theory of confinement with films of dopant concentrations varying from 0.1 to 0.04 mole fraction. A reduction in the concentration of impurities must result in an increase in the maximum size of the cooperatively rearranging H_2O domains, and, according to the Adam-Gibbs theory, an increase in the apparent activation energy. 132

Figure 5.9. The enthalpy relaxation times of vicinal ASW doped with 0.1 mole fraction of CH_3COOH (black circles with dotted line) and at mole fractions below 0.04 (solid line). The shaded region between the two lines in the figure represents the range of possible relaxation time values which would be expected for a contaminated vitreous water sample that may have an arbitrarily low number of impurity species. The DSC (open square) and dielectric spectroscopy data (open circles) from Johari's studies of "pure" water fall neatly within the shaded region. Thus, data from "pure" water samples that sporadically display endothermic features may actually come from unintended impurities. 135

Figure 6.1. Heating curves of ASW films from variable rate FSC experiments. By systematically changing the biasing voltage from 1.5 V to 10 V across the filament, the heating rates were varied from 3 kK/s to 1 MK/s; thereby, varying the onset and duration of crystallization of the ASW film. The crystallization of

each ASW film is manifested on the heating curves as a sudden increase in the temperature of the films (marked by intersecting dashed lines). 141

Figure 6.2. Characteristic crystallization time as a function of temperature derived from data in Figure 6.1. The black circles represent the results of FSC experiments, while the grey circles represent similar data obtained from temperature programmed desorption (TPD) experiments of thin (200 nm – 500 nm) ASW films. As demonstrated by the solid line, τ_{CR} values measured with FSC at temperatures near 200 K and those estimated from TPD experiments near 140 K, can be interpolated using a simple Arrhenius function, despite the differences between ASW sample geometry, dimensions, and the experimental techniques employed. 142

Figure 6.3. Based on the assumption of the continuity hypothesis, when using a heating rate within the range of 10^3 K/s to 10^6 K/s in an FSC experiment, the laboratory glass transition must occur over the range of temperatures from 160 K to 180 K (shaded area). 147

Figure 6.4. Based on the assumption that water is a fragile liquid over the temperature range from cryogenic to ambient, the existence of a glass transition in the range of 160 K to 180 K (shaded area) would cause the crystallization kinetics of ASW at temperatures above 180 K to be distinctly different from those at temperatures below150 K (dashed lines). However, the data maintains a strong Arrhenius dependence over the entire temperature range (solid line); thereby, discrediting the continuity hypothesis. 149

Chapter 1: Introduction

1.1 Experimental Research on Fundamental Physics and Chemistry of Condensed Aqueous Phase: Utility and Challenge

Condensed aqueous phases, liquid and glassy water, ice, solid and liquid solutions are involved in a vast array of environmental, biological and industrial processes[1-20]. The importance of research into water and ice can hardly be overstated. As shown in Figure 1.1, the number of scientific articles that take into account aqueous phase physics and chemistry has steadily increased in the past and now ranges in the tens of thousands per year. The sheer magnitude of the current research involving water reveals the significance of the physics and chemistry of the various forms of water.

Despite centuries of scientific inquires, there are still significant gaps in our understanding of the most fundamental properties of various condensed aqueous phases. Indeed, a comprehensive description of the hydrogen bond network in water, ice, and aqueous solutions remains an elusive goal, as demonstrated by a limited success of current theoretical models to accurately reproduce the physical and chemical properties of water across a wide temperature range. The lack of fundamental understanding of aqueous phase physics and chemistry is primarily due to the inability of current experimental techniques to provide extensive, molecular level information on the dynamics and reactions in water and ice at various temperatures. This is not surprising considering the seemingly incompatible

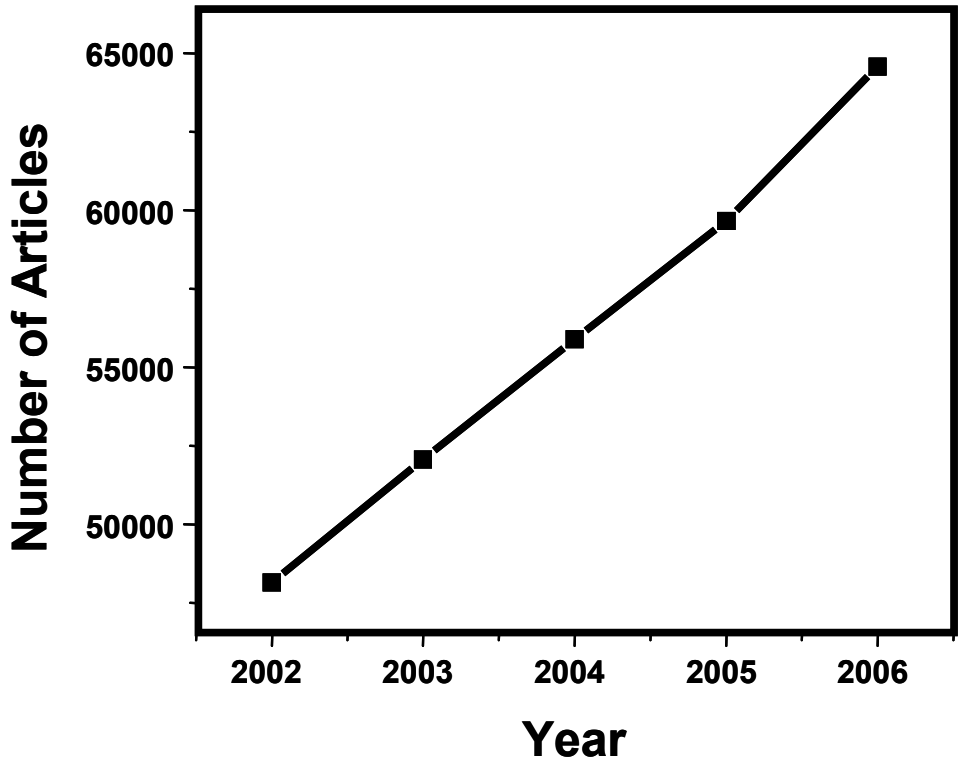

Figure 1.1. The number of scientific articles published over the last several years that take into account aqueous phase physics and chemistry.

set of requirements imposed on experimental techniques for broad range physical chemistry studies of water. Ideally, such techniques would be highly sensitive to a particular property of an aqueous system, capable of distinguishing physical processes at various interfaces (such as grain boundaries in polycrystalline ice) from those which occur in the bulk of an aqueous sample, and capable of precise characterization and control of aqueous sample structure. Furthermore, such techniques would be capable of studies of the physical and chemical properties of water over a wide range of temperatures from cryogenic to ambient.

Over the past few decades, an impressive arsenal of experimental methods has been developed and successfully applied to studies of aqueous phase phenomena. Examples of core physical chemistry studies of interest to aqueous phase chemistry now include interrogation of ice and water surfaces with non-linear vibrational spectroscopy techniques[21-23]; FTIR spectroscopy of ice nanocrystals[24]; studies of adsorption and reactions of various chemical species on surfaces of H_2O clusters generated with a molecular beam source[25]; studies of phase transitions and chemical reactions in single microscopic aqueous particles suspended in electrodynamic balance[26]; studies of uptake of various species on aqueous surfaces with droplet train and bubble train reactors[27], experiments on molecular beam scattering from liquid surfaces[28]; photoelectron spectroscopy studies of microscopic water jet surfaces in vacuum[29]; and, finally, the high vacuum thermal desorption spectroscopy studies of ice and amorphous solid water under cryogenic conditions[30-47].

Although these and other successful studies resulted in significant progress toward the understanding of physics and chemistry of the aqueous phase, very few current

techniques combine the entire set of "ideal" capabilities, i.e., sensitivity, selectivity, control over the aqueous sample structure, and a broad accessible temperature range. For example, traditional surface science thermal desorption methods provide unmatched capabilities for aqueous phase characterization and control, as well as excellent sensitivity; however, their applications are limited to a cryogenic temperature range where the vaporization rates of volatile aqueous phases are low. Furthermore, under certain conditions, direct experimental studies of water are hindered simply by its unusual physical properties. Indeed, the challenges involved in experimental studies of water are reflected in the current terminology, where "No Man's Land"[48] is often used to emphasize a lack of experimental studies of non-crystalline (amorphous, glassy) aqueous phases in the temperature range from 160 to 235 K.

1.2 New Approach to Studies of Physics and Chemistry of Condensed Aqueous Phase

Several years ago, motivated by a wide range of intriguing and challenging problems in the field of physical chemistry of aqueous phases, Professor Sadtchenko's group and I undertook the further development of a new, comprehensive, versatile experimental approach to fundamental studies of aqueous phase phenomena known as Fast Thermal Desorption Spectroscopy – Fast Scanning Calorimetry (FTDS-FSC)[49-56] . This approach is based on the extensive modification and fusion of two powerful analytical techniques: temperature programmed desorption/reaction (TPD) spectroscopy, and differential scanning calorimetry (DSC), which have been used successfully in the past to study aqueous phases *at cryogenic temperatures*.

As shown in Figure 1.2, the core of the experimental apparatus is a thin, tungsten filament positioned in a vacuum chamber and initially set at temperatures from 120 to 175 K[49-56]. The filament serves as a substrate for the vapor-deposition of pure and doped aqueous films with thicknesses ranging from a submonolayer to a few micrometers, i.e., similar to those used traditionally in surface science experiments. A low deposition temperature ensures that virtually no molecular transport or reactions take place during film preparation. As in conventional temperature program desorption studies, the vapor deposition allows a great degree of control over the structure and phase composition of the aqueous film. Furthermore, the structure of the aqueous films can be studied and characterized by standard high vacuum surface science techniques[49-56].

Following deposition, the aqueous film can be rapidly heated by passing an electrical current through the filament. The applied voltage and the current through the filament are monitored continuously, thus, making it possible to infer the temperature and heat capacity of the filament/film system. Due to the small mass of the wire and aqueous sample, heating rates in excess of 10^5 K/s can be easily achieved, making it possible to bring the temperature of a micrometer thick ice film to a value as high as 273 K before a significant fraction of the film vaporizes. Furthermore, because the overall heat capacity of the microscopic filament is comparable to that of the aqueous film, scanning calorimetry can be used to study phase transitions in aqueous films during rapid heating at temperatures from 110 K to 220 K[49-56].

After the initial rapid heating, the temperature of the film can be stabilized at any value from 230 K to 273 K, thus resulting in *near isothermal zero-order desorption* of the

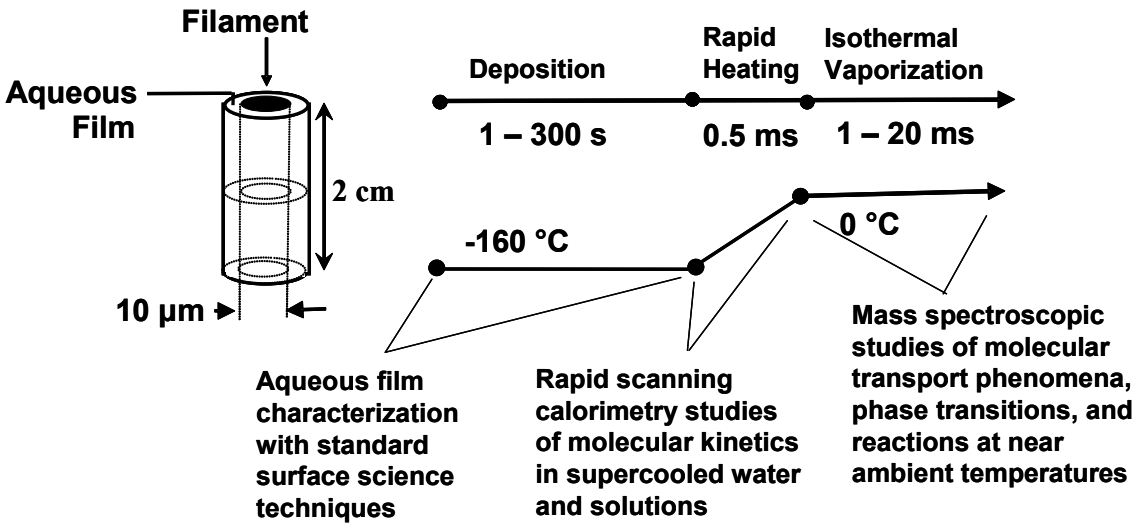

Figure 1.2. The essential steps involved in a basic FTDS-FSC experiment.

multilayer aqueous sample. In a doped aqueous film, vaporization near ambient temperatures is accompanied by molecular transport of guest chemical species and their reactions. The small physical dimensions of the substrate ensure that reaction/desorption products undergo only a few collisions in the gas phase even at temperatures approaching the ice melting point[53]. Thus, the reaction/desorption products *can be analyzed directly* by mass spectrometry, time-of-flight (TOF) mass spectrometry, or other sensitive analytical techniques[49-50].

In summary, while retaining many advantages of the traditional TPD and DSC techniques, the FTDS-FSC is capable of detailed studies of the molecular kinetics, transport phenomena, phase transitions, and chemical reactions at temperatures near ambient in condensed aqueous phase over a temperature range from cryogenic to ambient. This dissertation thesis describes the application of the FTDS-FSC approach to studies of amorphous solid water, i.e., ASW.

1.3 Supercooled Liquids and Glasses: Essential Agreed Upon Views and Definitions

As noted by Andersen[57], the theory of the nature of glass and glass transition is "the deepest and most interesting *unsolved* problem in solid state theory." Although almost 15 years have passed since this historic quote, a comprehensive theoretical understanding of supercooled liquids is just beginning to emerge. Because the interpretation of the results of my Fast Scanning Calorimetry studies is based on the current advances in the field of physical chemistry of supercooled and glassy condensed phases, I must first discuss the currently accepted general views and essential definitions relevant to the experimental results and analysis presented in this thesis.

1.3.1 Nature of Supercooled Liquids and Glasses from Thermodynamic Standpoint: Kauzmann's Ideal Glass Hypothesis

From the purely thermodynamic point of view, neither supercooled liquids nor glasses are supposed to exist. As shown in Figure 1.3 (gray line), a thermodynamically stable liquid must undergo a first order phase transition at a well defined temperature, $T_{melting}$. Unlike a crystal, where the primary contribution to the entropy of the ordered phase is from lattice vibration, a liquid is characterized by a large number of accessible structural configurations and, therefore, has greater specific entropy[58]. Thus, the crystallization of a liquid is characterized by a significant decrease in entropy.

Although freezing of a pure liquid must occur at a temperature well-defined by the substance's phase diagram, an infinite observation time is required to observe it. Indeed, the size of a critical nucleolus diverges at temperatures slightly below $T_{melting}$, thus, resulting in an extremely low probability of spontaneous formation of the crystalline phase[59]. In other words, any relatively pure liquid can be "supercooled" under realistic conditions.

For a simple molecular liquid in which crystallization is somehow prevented, the entropy of the supercooled state can be represented as a linear extrapolation of the entropy of the thermodynamically stable liquid through the temperature region below $T_{melting}$ (dashed line in Figure 1.3)[60]. The lowering of the temperature of the liquid below $T_{melting}$ must be accompanied by a slow-down in molecular kinetics, i.e., by an increase typical time required for structural rearrangement of the liquid constituents toward a state of progressively lower entropy. Nevertheless, if the cooling rate during such an imaginary

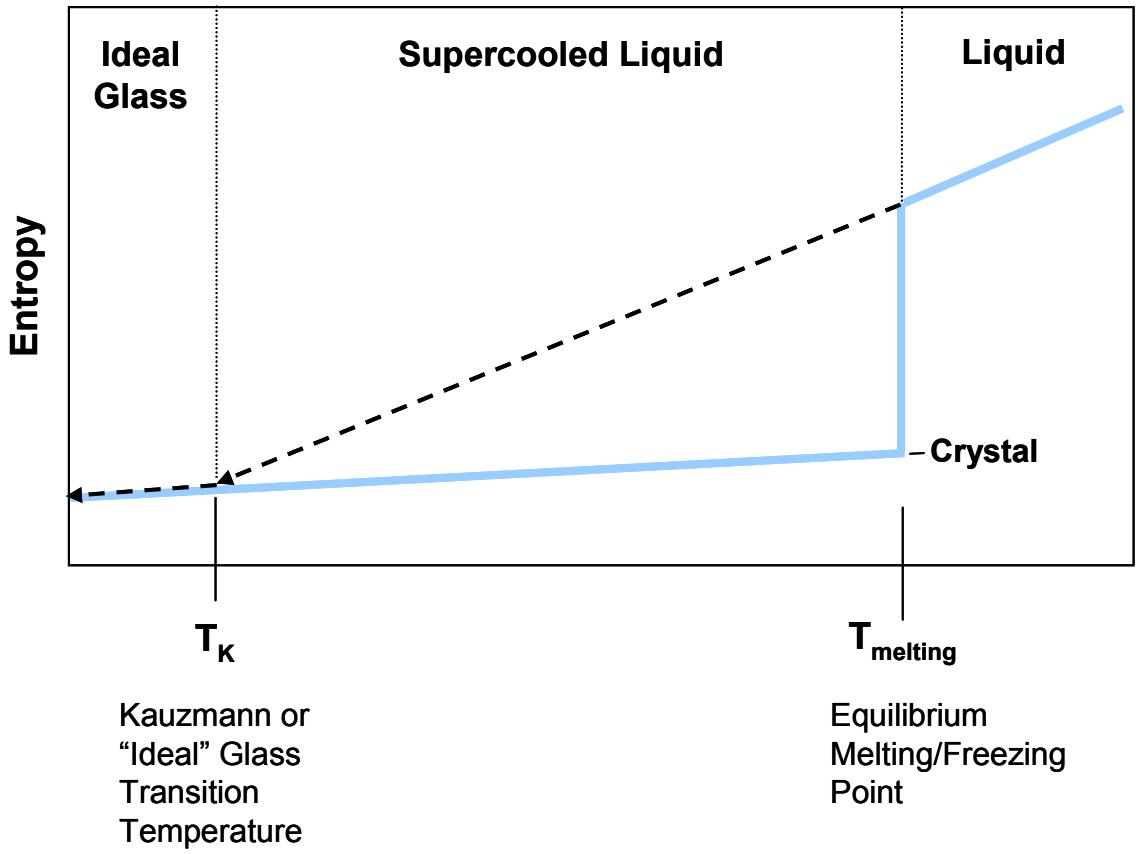

Figure 1.3. The entropy of a stable liquid decreases with temperature up to its freezing/melting point, where it undergoes a first order phase transition to form a crystalline solid (blue line). When the crystallization of a liquid is suppressed and its temperature is lowered past $T_{melting}$, it is considered a supercooled liquid. The entropy of this state is represented by a linear extrapolation of the entropy of the thermodynamically stable liquid (dashed line). As this line extends, it approaches the entropy of the crystalline state and becomes equal at the Kauzmann temperature, T_K. This temperature marks the greatest degree of supercooling achievable by any stable liquid, which is termed a "glass" under these conditions.

experiment is infinitely slow, the entropy of the supercooled liquid will continue to decrease until it approaches the entropy of the crystal at some point as shown in Figure 1.3. The hypothetical temperature at which the entropy of a supercooled liquid becomes equal to that of a crystal is known as the "Kauzmann Temperature" (T_K)[60,61].

Although a slight decrease in the entropy of the supercooled liquid with respect to that of a crystal is possible[60], in principle, further extrapolation of the entropy of a liquid to a temperature range below T_K would sooner or later result in a violation of the Third Law of Thermodynamics by producing zero or negative entropy at temperatures well above 0 K. The so-called "entropy crises"[60] described immediately above lead Kauzmann to postulate the existence of an "ideal glass", i.e., a deeply supercooled liquid whose entropy is indistinguishable from that of a crystal. Such an ideal glass would need to have a vibrational entropy lower than that of its corresponding crystal in order to compensate for its greater configurational entropy. However, the variations in the overall entropy of the ideal glass would be identical to those of a crystal at temperatures below T_K. In summary, within the framework of the Kauzmann paradigm, T_K marks the greatest degree of supercooling achievable with ideal conditions. At temperatures below T_K, the configurational entropy of a supercooled liquid and other thermodynamic variables are "frozen in" and cannot be described as a low temperature extrapolation of those of equilibrium liquid. As the result a new, thermodynamically distinct "glassy" phase must occur.

1.3.2 Nature of Supercooled Liquids and Glass from a Practical (Laboratory) Standpoint: Laboratory Glass and Laboratory Glass Transition

The entire line of Kauzmann's thermodynamic reasoning described in the preceding section relies on *idealized* conditions such as an infinitely slow cooling and lack of crystallization.

As a result, the physical properties of a supercooled phase can never be directly observed at temperatures near T_K. Although the Kauzmann paradigm is still a matter of a debate, there is a certain consensus about the fundamental origins of *experimentally observed* variations in such properties of supercooled liquids, such as heat capacity, has been achieved, albeit only over the past decade[60,62,63].

The key to understanding the essential definitions in the field of fundamental studies of supercooled liquids is not the thermodynamics but kinetics. Indeed, as previously mentioned neither "glass" nor "supercooled liquid" are supposed to exist at temperatures below $T_{melting}$. If a supercooled liquid appears to be "stable" under certain experimental conditions, the immediate conclusion is that the experimental observation time is significantly short compared to the characteristic time of relaxation of the out-of-equilibrium liquid toward its equilibrium state, i.e., crystal[62]. In short, any current experimental results with *laboratory* "supercooled liquids" or *laboratory* "glasses" must be interpreted by taking into account the characteristic time scale of the experimental observation.

As mentioned above, the essential distinction between the liquid phase and the crystalline phase lies in the entropy of these phases. While the main contribution to the

entropy of a crystal is from vibrational degrees of freedom, the overall entropy of a liquid is defined by the ability of its constituents (molecules, atoms, ions etc.) to form a wide range of distinct structural microstates by means of translational and rotational motion. The ability of a liquid to assume a large number of structures at a particular temperature results in large "configurational" contribution to the overall entropy of the non-crystalline phase (configurational entropy)[58].

As the temperature of a liquid is lowered below its equilibrium freezing point, the translational and rotational motion, i.e., the *constituent kinetics*, slows down. A fundamental variable which is used to characterize the rate of structural rearrangement in a liquid is referred to as "*microscopic relaxation time"* (τ). *The microscopic relaxation time is the characteristic time required for the thermodynamic system (in this case liquid), to reestablish the most probable structural configuration after a small perturbation*[60]. For toluene near ambient temperatures, the microscopic relaxation time is approximately 10^{-11} – 10^{-12} seconds. Nevertheless, it increases to values as high as 100 seconds near 117 K[64]. While the picosecond time scale of a liquid's microscopic relaxation at ambient temperatures is sufficiently short for most of the experimental techniques, the interplay between the experimental observation time and the microscopic relaxation time becomes important at cryogenic temperatures. The possible impact of long microscopic relaxation times on outcomes of laboratory measurements is illustrated immediately below.

Imagine an experiment where a liquid is cooled with a certain rate and the heat capacity is continuously monitored. Let us also assume for the sake of simplicity that this experiment is designed so that the crystallization of the liquid is physically impossible. In

this case, the entropy of supercooled liquid *under conditions of infinitely slow cooling* is the equilibrium entropy of the supercooled liquid (see the dashed line in top panel of Figure 1.4). As shown in Figure 1.4, at high temperatures (above the point marked T_g), where the microscopic relaxation time is much shorter than the observation time, the liquid will be able to assume a new equilibrium configuration as the temperature is lowered. However, due to the slowdown in its constituents' kinetics, the microscopic relaxation time must ultimately become greater than the observation time at some temperature marked as T_g in Figure 1.4. At temperatures below T_g, the configurational entropy of the liquid would not be able to change significantly on the observational time scale. Therefore, *from the point of view of the observer*, the liquid's microscopic structure must *appear* to become temperature invariant at temperatures below T_g[62]. Due to such inability of a liquid to assume distinct structural microstates on the time scale of observation, the heat capacity must *appear* to undergo a sudden decrease at T_g. Note however that such a decrease in the heat capacity does *not* reflect any fundamental change in the nature of the liquid and is simply a result of the limitation of the experimental technique (short observation time)[62].

In summary, the so-called "glass transition" manifested in scanning calorimetry experiments as a sudden decrease in the *apparent* heat capacity of supercooled liquid at a particular temperature does not represent the formation of any new phase such as an the ideal glass hypothesized by Kauzmann. Nevertheless, due to the past use of the term "glass" in material engineering, deeply supercooled liquids whose microscopic relaxation time is greater that an arbitrary value of 100 s are commonly referred to as "laboratory glasses". A supercooled liquid where the microscopic relaxation time is shorter than 100 s

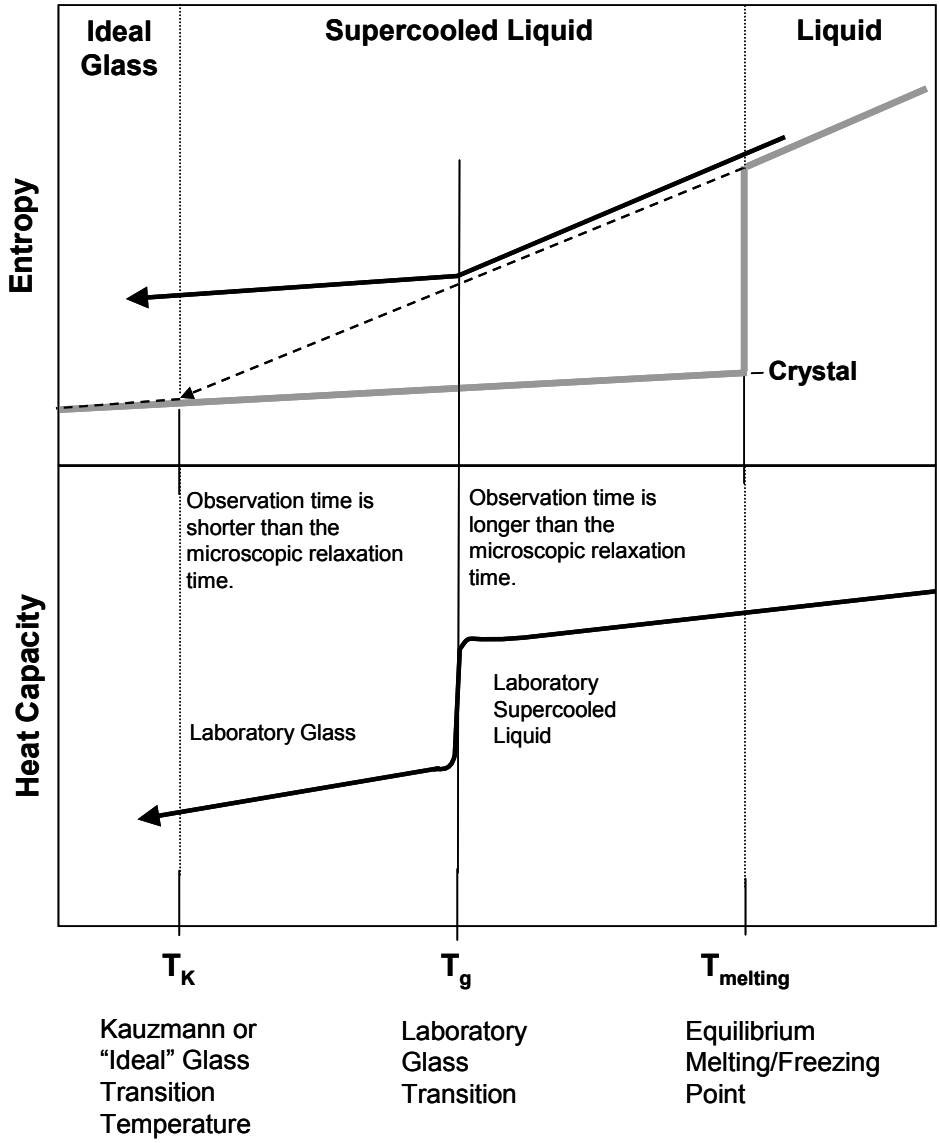

Figure 1.4. Top panel: As a stable liquid is lowered past $T_{melting}$, it enters a supercooled state. Based on the observation time, it appears as though the configurational entropy of the liquid's constituents continues to decrease up to a certain temperature, T_g, at which point the configurational entropy appears to be temperature invariant. Bottom panel: As the kinetics of the liquid's constituents (molecules, atoms, etc.) slow down, there is a decrease in the heat capacity of the liquid. At the point where the observation time becomes shorter than the microscopic relaxation time, there is a sudden drop in heat capacity at T_g. The temperature at which this drop occurs is dependant upon the length of the observation time of the experimental technique.

but is significantly longer than a nanosecond is sometimes referred as a "ultraviscous liquid" or simply as a "viscous liquid"[60,62].

Although the heat capacity measurements described above (essentially a scanning calorimetry experiment), may not provide any thermodynamic data at temperatures near laboratory T_g, it may still be used to characterize constituent kinetics in a supercooled liquid. Indeed, by varying the cooling rate and monitoring the resulting changes in laboratory T_g, the dependence of a microscopic relaxation time on temperature can be determined. For example, in Chapter 5 of this thesis, I describe a conceptually similar experimental approach that made it possible to estimate the microscopic relaxation time of binary aqueous solutions at several selected temperatures.

1.3.3 Strong and Fragile Liquids: Dependence of Microscopic Kinetic Parameters on Temperature

In addition to the variable rate scanning calorimetry method described in the preceding section, the microscopic relaxation time can be measured by other techniques, where the time of a detectable variation in a structure dependent property of a liquid is monitored after a small and controlled structural perturbation. An example of such a technique is the broadband dielectric spectroscopy (BDS or DS), which makes it possible to determine the relaxation time, i.e., the characteristic time of dipole rearrangement in a molecular liquid by monitoring the variations in the permittivity of the dielectric liquid resulting from variations in an external electric field[60,63,65]. Because the microscopic relaxation time is essentially a measure of the rotational and translational mobility of liquid constituents, the temperature dependence of other kinetic parameters (self-diffusivity,

viscosity) show a strong correlation with that of the microscopic relaxation time. For instance, a self-diffusion coefficient in a liquid can be estimated (within an order of magnitude) from the microscopic relaxation time at a particular temperature using the Einstein-Smoluchowski equation with a characteristic diffusion length equal to average intermolecular distance[66].

Over the past half a century numerous measurements of viscosity, self-diffusivity, and relaxation time have been conducted with a myriad of supercooled liquids at various temperatures. According to these studies, the temperature dependence of the kinetic parameters, such as the microscopic relaxation time, often follows three distinct scenarios[60,63]. As illustrated in the Figure 1.5, the slowdown in constituent kinetics (increase in relaxation time and viscosity, and corresponding decrease in self-diffusivity) may or may not follow Arrhenius law. Thus, a classification of liquids based on the temperature dependence of their microscopic kinetic properties has emerged: 1) a liquid which demonstrates an Arrhenius dependence of a kinetic parameter on temperature is referred to as "strong"; 2) a liquid characterized by non-Arrhenius variations in molecular kinetics with temperature is referred to as "fragile". While most of the liquids show a "simple fragile" behavior at temperatures below $T_{melting}$, in the case of water, a possibility of an anomalous crossover from fragile to strong behavior has been suggested[63]. A "fragile-to-strong" crossover in the temperature dependence of the microscopic relaxation time is illustrated in Figure 1.5 by the dashed line.

The origins of liquids' "fragility" (deviation of temperature dependence of kinetic parameters from the Arrhenius law) are currently a very active research area[63,67-71].

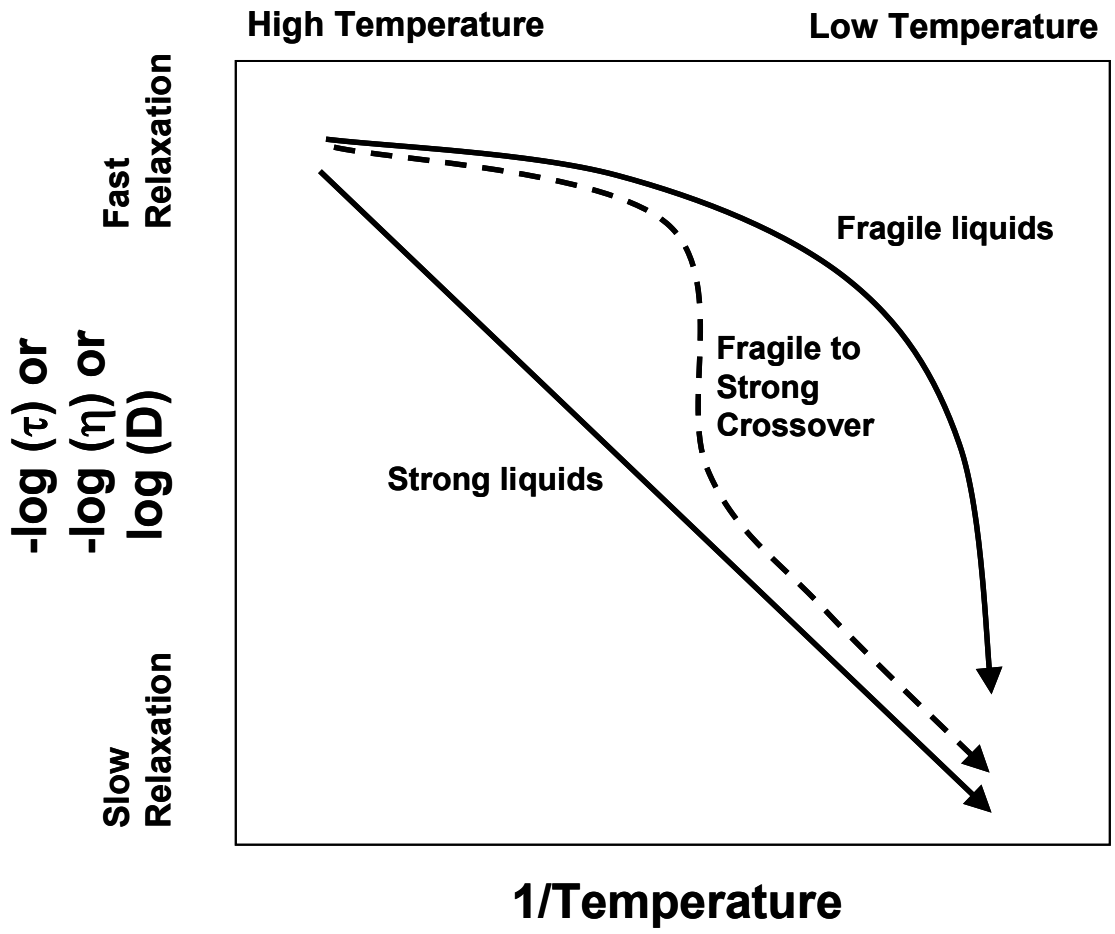

Figure 1.5. The kinetic parameters of a "strong" liquid demonstrate an Arrhenius dependence with temperature (straight arrow); whereas, the kinetic parameters of a "fragile" liquid do not exhibit such a dependence (curved arrow). It the case of water, it is suggested that there may be a "fragile-to-strong" crossover (dashed arrow) based on the rate of its microscopic relaxation time.

Although a new theory of "viscous slowdown" would typically appear in the literature every year or so, the most generally accepted model is that developed by Adam and Gibbs in the late 1960s[72,73]. Note that the Adam-Gibbs theory (AGT) is explained in detail in Chapter 5 of this thesis.

1.3.4. Amorphous Solids

Most of the examples and imaginary experiments described in Sections 1.3.1 through 1.3.3, focused on the case where non-crystalline, out-of-equilibrium, condensed phase is created by gradually lowering the temperature of a liquid below $T_{melting}$. However, a number of other methods may be used to create these unique, disordered phases at temperatures significantly below laboratory T_G. Such disordered phases, while maintained at extremely low temperatures, are often referred to as amorphous or vitreous solids[74]. An amorphous solid phase can be produced from a crystal as a result of subjecting it to intense mechanical shocks or radiation[75]. Alternatively, a disordered, condensed phase can also be created by vapor deposition of the phase constituents (atoms or molecules) on a substrate maintained at temperature significantly below laboratory T_g[74,76]. For instance, supersonic or effusive beam deposition of water molecules on amorphous platinum substrate at temperatures below 100 K in vacuum may lead to a highly microporous disordered H_2O phase whose density can be as low as 20% of the density of water under ambient conditions[66,76-78].

Although the enthalpy and entropy of these structurally unique amorphous solids may be significantly higher than that of a supercooled liquid, slow annealing of such a phase at cryogenic temperatures typically results in its relaxation into a non-crystalline

phase structure and is otherwise indistinguishable from a supercooled liquid. For example, low density, amorphous solid H_2O converts into supercooled water in matter of minutes at 130 K[74].

As a result of extensive studies of the physical properties of thin (a few nanometers) vapor deposited H_2O films by Kay's group[66,76-78], the use of the term "pore-free amorphous solid water" or simply "amorphous solid water" (ASW) became widespread approximately 10 years ago. The "amorphous solid" part of the designation serves to emphasize the vapor deposition route used to create supercooled water in this type of studies. Because vapor deposition upon a cold substrate is the method employed in my FTDS-FSC experiments, I use the "ASW" acronym for the supercooled water employed in all of my experiments.

1.3.5 Characteristic Crystallization Time of a Supercooled Liquid

So far, in my description of the general thermodynamic and kinetic features of supercooled liquids, I have avoided any discussion of supercooled liquid crystallization. However, crystallization of deeply supercooled liquids at temperatures as far as a hundred degrees from the equilibrium freezing point is, by itself, an interesting physical phenomenon, and is important for the understanding results of the FSC studies of supercooled water described in this thesis. Immediately below, I describe the general features of supercooled liquid crystallization at temperatures below $T_{melting}$.

Figure 1.6 shows the typical temperature dependence of the *characteristic crystallization time* (τ_{CR}) for a supercooled liquid. The characteristic crystallization time is defined as the time required for the crystallization of a certain fraction of a non-crystalline

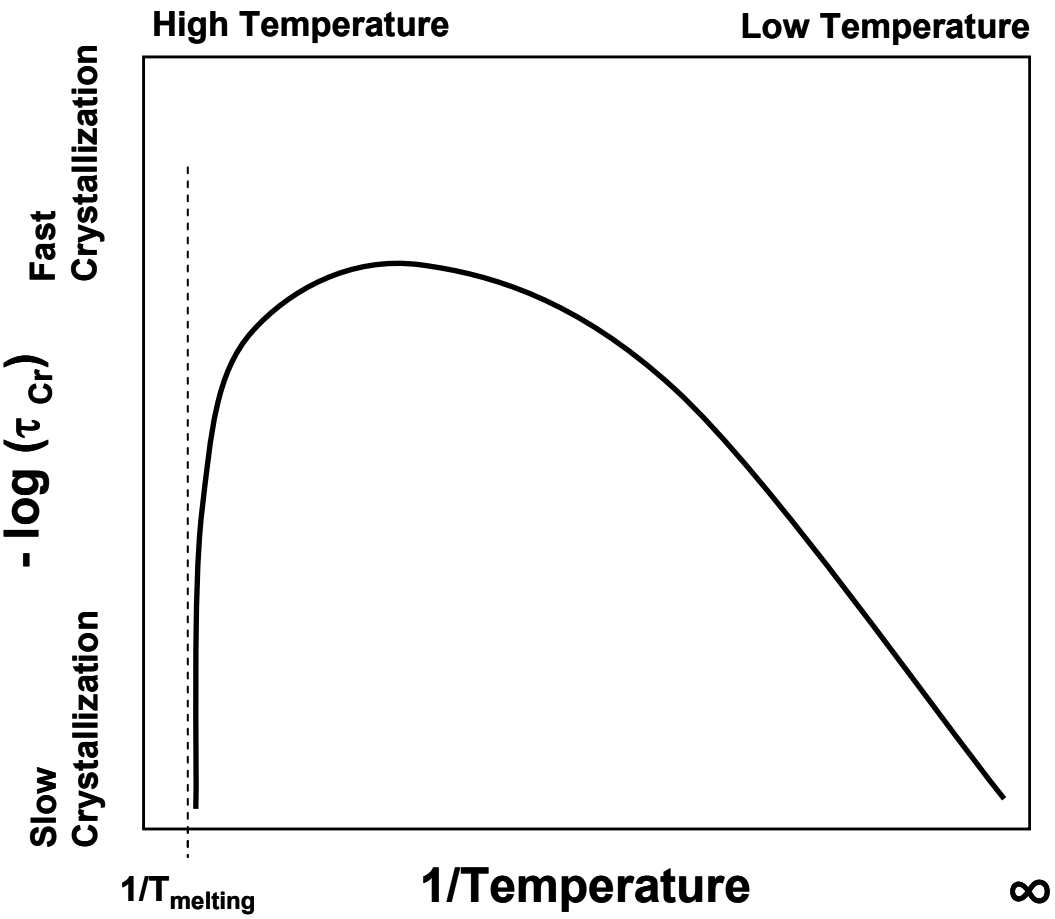

Figure 1.6. Temperature dependence of the crystallization time (τ_{CR}) for a supercooled liquid. At temperatures just below $T_{melting}$, τ_{CR} is infinitely slow, due to a high Gibbs free energy barrier. As the temperature continues to decrease, this energy barrier decreases; thereby, allowing crystallization to occur faster. If the temperature is cooled to cryogenic temperatures, then the slowdown in constituent kinetics leads to an infinite increase in the crystallization time (slower crystallization).

sample[59]. For instance, the crystallization half-time is the time which is necessary for conversion of 50% of the volume of a non-crystalline sample to stabilize into the crystalline phase. As shown in the figure, τ_{CR} is a complex function of temperature which has a broad *minimum* at certain temperature below $T_{melting}$. Also note that τ_{CR} approaches infinity at cryogenic temperatures and at temperatures slightly below $T_{melting}$.

Although the particular range of crystallization time and the fine details of its variation with temperature depend on the nature of the supercooled liquid, the general features of crystallization kinetics depicted in Figure 1.6 are observed almost universally. Furthermore, the "U-shaped" curve shown in the figure is rationalized surprisingly well by the classical homogeneous nucleation theory (HNT)[59]. According to HNT, the high Gibbs free energy barrier (a consequence of low supercooling) results in extremely low values of the crystallization rate and consequently in the long crystallization time. As the temperature is lowered, the barrier to crystallization decreases. In an extreme case of large supercooling, the crystallization kinetics approach a spinoidal phase decomposition limit, i.e., the range of temperatures where the size of critical crystalline nucleus is less than a single molecule. At this point, the crystallization rate is essentially limited only by constituent self-diffusion. A further decrease in the temperature, however, leads to the slowdown of the constituent kinetics in a supercooled liquid/crystal mixture, and consequently, an increase in the crystallization times.

The variations in the characteristic crystallization time depicted in Figure 1.6 serve to once again emphasize the interplay between the experimental observation time scale and the characteristic time scale of a physical process. Imagine an experiment in which the

crystallization is only detectable if a certain fraction of the supercooled liquid is crystallized. An example of such an experiment is a calorimetry scan where an amorphous solid is heated with a certain rate. On the scanning calorimetry thermogram, crystallization is manifested as a decrease in apparent heat capacity, i.e., by an exothermic downswing in the heat capacity-temperature curve. However, the exotherm can only be detected when the characteristic crystallization time is comparable to the experimental observation time. Because the experimental observation time is inversely proportional to the heating rate, and because the characteristic crystallization time is a strong function of temperature, the onset of crystallization (i.e., the temperature where crystallization becomes detectable) must increase with the heating (scan) rate. In other words, in a fast thermogram of a deeply supercooled liquid or an amorphous solid, a relatively high temperature may be reached before a significant fraction of the sample is crystallized.

1.3.6 Anatomy of a Fast Scanning Calorimetry Experiment

To summarize the concepts and definitions described in Sections 1.3.1 – 1.3.5 and to put them in the context of the Fast Scanning Calorimetry studies presented in this thesis, I would now like to discuss the possible outcomes of two FSC experiments conducted with a hypothetical supercooled liquid initially maintained at low temperatures. Let us assume that the liquid's entropy is near that of the ideal Kauzmann's glass and that two FSC thermograms are measured with distinct heating rates (slow and fast).

As shown in Figure 1.7, heating a supercooled liquid with a finite rate must first result in a crystal-like temperature dependence of the apparent entropy and heat capacity on temperature. Indeed, as described in Section 1.3.2, due to long (compared to experimental observation time) microscopic relaxation times, the contribution to the overall entropy of

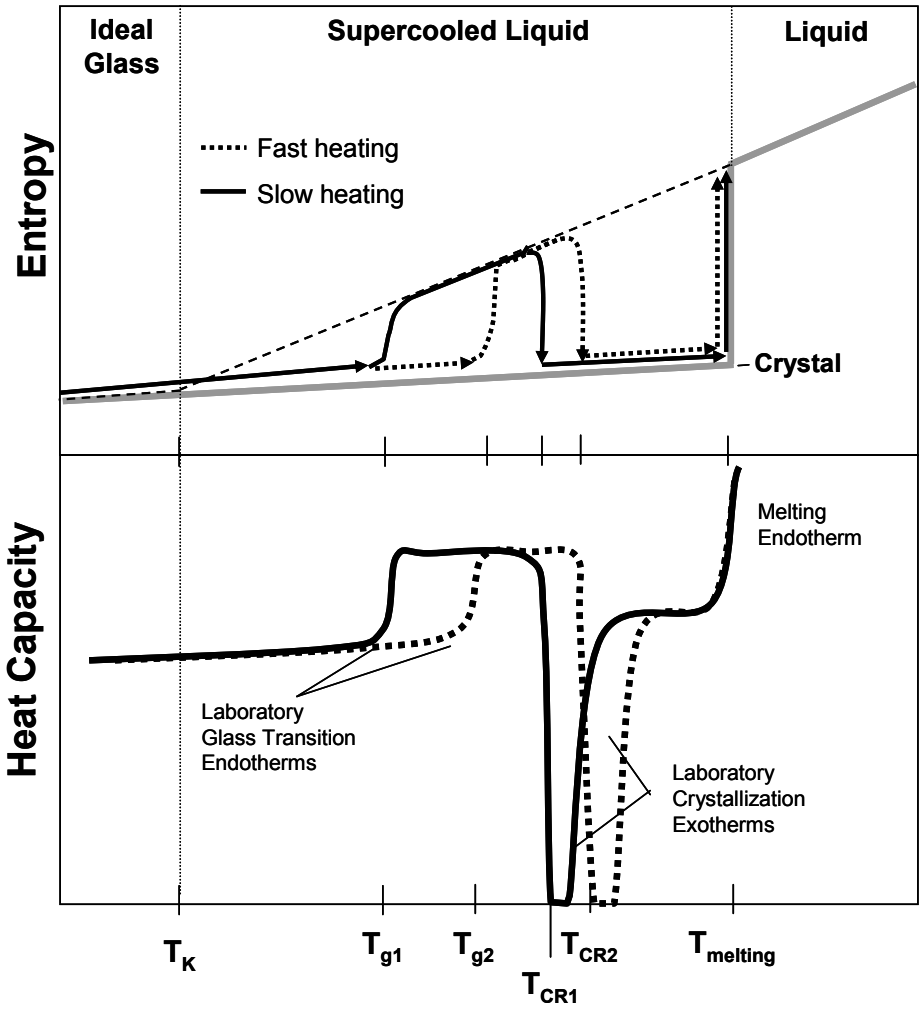

Figure 1.7. Top panel: Heating a laboratory glass at a finite rate initially resembles crystal-like entropy. As the configurational rearrangement of the glass' constituents "unfreezes," the entropy of the glass increases quickly to match that of a deeply supercooled liquid (T_{g1}). Since the experimental observation time decreases with an increasing heating rate, the temperature of the glass transition measured with a higher heating rate manifests at a higher temperature (dotted line, T_{g2}). As the temperature continues to increase, the characteristic crystallization time of the liquid becomes comparable to the experimental observation time, causing the entropy to drop to that of the liquids crystalline solid. Again the temperature at which the crystallization occurs is dependant upon the heating rate. Bottom panel: The heat capacity of a laboratory glass initially follows that of its crystalline solid up to the point of its glass transition. The glass transition appears as an endothermic feature on the thermogram. As the temperature of the supercooled liquid continues to increase, the liquid crystallizes, which results in an exothermic feature on the thermogram.

the supercooled liquid would be limited to its vibrational degrees of freedom. Nevertheless, a progressive decrease in the microscopic relaxation time with temperature must ultimately result in the "unfreezing" of the configurational rearrangement of the liquid structure and a consequent jump in apparent heat capacity (i.e. in laboratory glass transition). Because the experimental observation time must be a monotonically decreasing function of the heating rate, the laboratory glass transition in the FSC thermogram measured with a higher heating rate must be manifested at higher temperatures.

Due to its out-of-equilibrium nature, the deeply supercooled liquid would also undergo progressively more rapid crystallization during the entire FSC experiment. Nevertheless, as shown in Figure 1.7, the crystallization heat release during the initial stages of an FSC scan may be far below detection limits of the calorimeter until the temperature reaches a value where the characteristic crystallization time is comparable to the experimental observation time (i.e. where the crystallization rate is fast). Because the characteristic crystallization time decreases monotonically with temperature (at low temperatures), and because the experimental observation time is inversely proportional to the heating rate, the crystallization isotherm must be manifested at higher temperatures in the fast scan.

Finally, note that in both cases, the FSC thermograms must show an endothermic feature due to the melting of the crystalline phase at $T_{melting}$. However, in the case of a FSC experiment conducted under high vacuum conditions, the endothermic melting of the crystalline phase may be preceded by sublimation, which would be also manifested as an endothermic upswing at temperature lower than $T_{melting}$.

Figure 1.8 provides further explanations for the essential features of the hypothetical FSC thermograms in Figure 1.7, by illustrating the complex interplay of three characteristic time scales of the scanning calorimetry experiments, i.e., the characteristic experimental observation time, the liquid's microscopic relaxation time, and liquid's characteristic crystallization time. As shown in Figure 1.8, the essential features of an FSC thermogram and the glass endotherm must be observed at a temperature where the experimental observation time (dashed line) becomes equal to the characteristic time of the corresponding processes. As it follows from Figure 1.8, an increase in the heating rate of an FSC experiment must result in an increase in the onset temperatures of both features: the laboratory glass transition and crystallization. Also note that the glass transition endotherm does *not* have to precede the crystallization exotherm. As I have mentioned in Section 1.3.5, the characteristic crystallization time may, in principle, be shorter than the microscopic relaxation time in a certain temperature range. Therefore, crystallization of certain liquids may be manifested in scanning calorimetry thermograms prior to the laboratory glass transition. As noted by Angell, the crystallization exotherm would make observation of the laboratory glass endotherm virtually impossible in this case.

1.4 Studies of Deeply Supercooled Water: A Key to the Understanding of Water Structure and Dynamics

It has long since been noticed that water, the most common solvent on Earth, has very few physical and chemical properties in common with other molecular fluids. The anomalous properties of water are manifested most noticeably when it is supercooled below the equilibrium freezing point near 273 K. For example, the constant-pressure heat

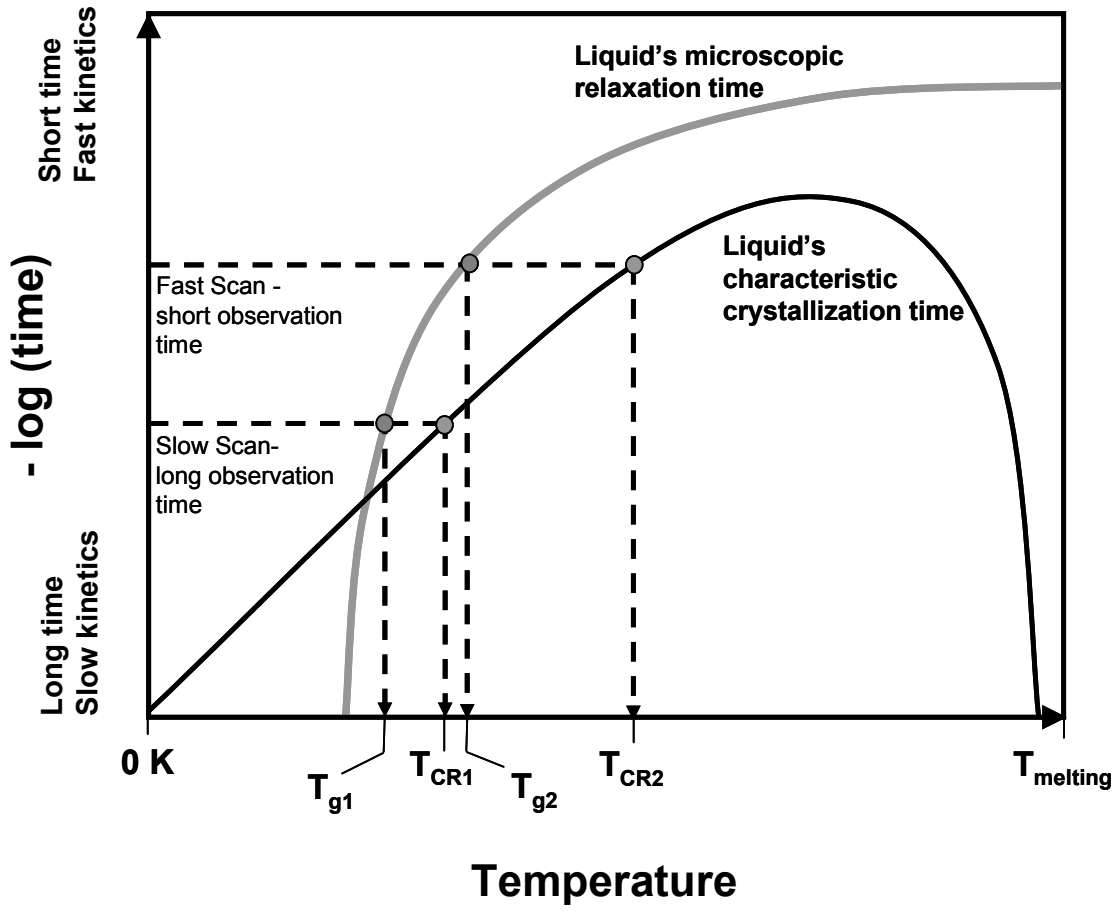

Figure 1.8. The essential features of an FSC thermogram (glass transition temperature, crystallization, etc.) are observed when experimental observation time becomes equal to the microscopic relaxation time (T_g) or the characteristic crystallization time (T_{CR}). During a slow scan rate, the temperature of the glass transition (T_{g1}) and crystallization (T_{CR1}) are lower than their corresponding temperatures (T_{g2} and T_{CR2}) from a faster scan rate.

capacity, coefficient of thermal expansion, and isothermal compressibility of water begin to diverge (increase dramatically) as the temperature approaches 228 K (spinoidal temperature, T_s)[79-81].

Over the past several decades, there have been numerous theoretical attempts to provide a consistent physical picture of the structural and dynamic properties of water under various conditions. For instance, the rapid increase in the heat capacity of supercooled water near T_s can be explained by the stability limit hypothesis, which postulates the existence of a thermodynamic singularity point near 228 K[82]. An alternative explanation is provided by a singularity-free conjecture, which predicts a rapid rise, but not a true discontinuity in thermodynamic functions at this temperature[83]. Finally, the existence of a liquid-liquid phase transition (LLPT) was proposed to explain the rapid change in the thermodynamic functions near T_s[84]. Although the LLPT hypothesis postulates a critical point on the water phase diagram at P_c=100 MPa and T_c = 220 K, at pressures below the critical point it predicts a λ−like continuous dependence of the heat capacity near T_s.

Despite decades of intense theoretical and experimental efforts, a consistent view of the interrelationships between non-crystalline phases of H_2O has just started to arise. A vivid example of the lack of understanding in the field is the controversy surrounding a specific interpretation of a rather large set of experimental results, i.e., "the continuity conjecture"[85,86]. As shown in Figure 1.9 (dotted lines), within the framework of the continuity hypothesis, various dynamic properties of ASW such as self diffusivity, viscosity, and enthalpy relaxation time, can be related to those measured for liquid water at temperatures above 260 K via a simple Vogel-Fulcher-Tammann (VFT) equation ($T_{vogel} \approx$

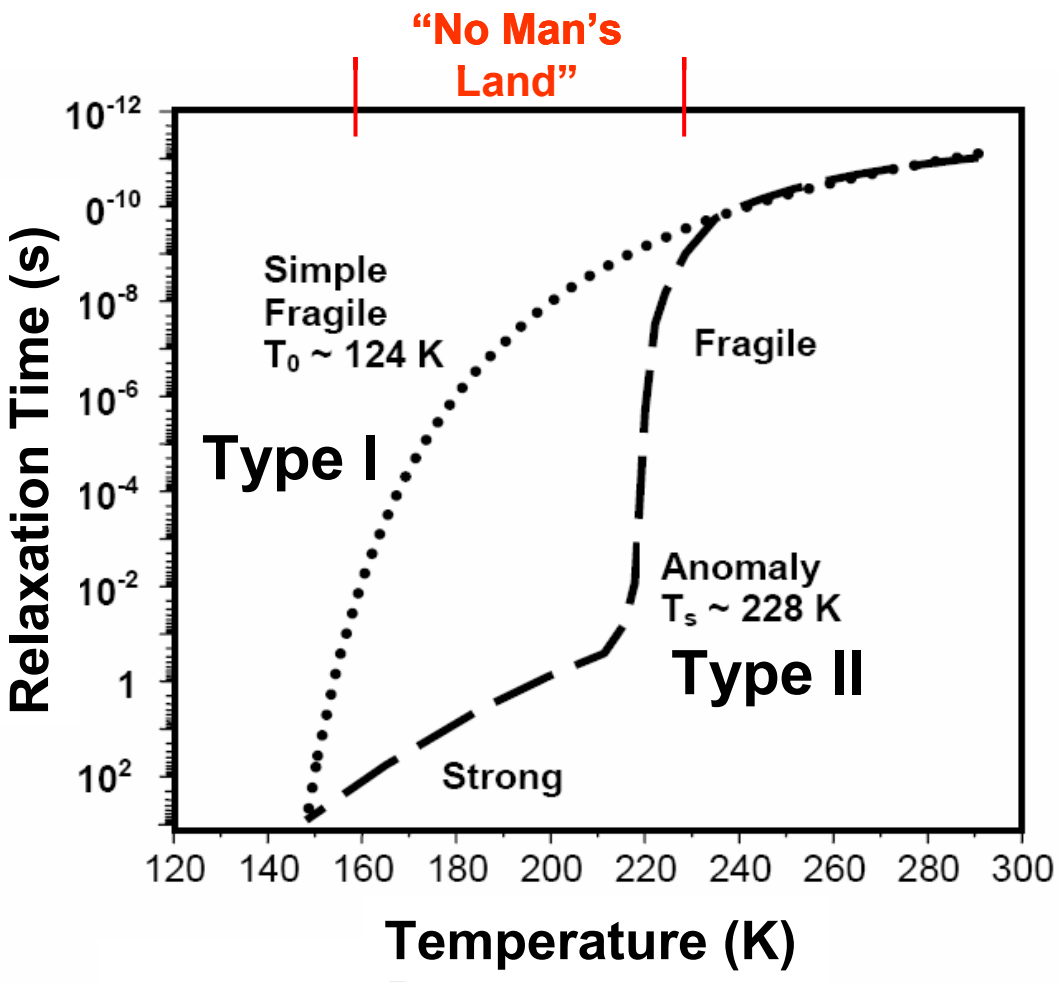

Figure 1.9. Two opposing hypotheses about the properties of water over the temperature range known as "No Man's Land" (160 K – 235 K). Type I (dotted line) illustrates the continuity conjecture, which assumes water is a fragile liquid over the entire temperature range from cryogenic to ambient. Type II (dashed line) illustrates a counter hypothesis that postulates that water undergoes an anomalous transition from a fragile to a strong liquid in the vicinity of T_s (228 K).

124 K)[85,86]. In other words, water is assumed to be simply a *fragile* liquid over the entire temperature range from cryogenic to ambient. The cornerstone of such interpretation of water properties is the original claim of observation of "calorimetric glass transition" at 136 K[87].

Experimental evidence, cited in support of the continuity conjecture, is substantial and includes traditional DSC experiments with pure and doped ASW, dielectric relaxation times measurements of ASW in Poly (HEMA) matrix[88]; water self-diffusivity studies in ultrathin (< 30 nm) ASW films[89], investigations of ASW's mechanical properties[90]; and selected FTIR experiments[91]. While some of these experiments (e.g., "blunt indenter" studies of amorphous ice deformation) were relatively simple, others relied on complex, state-of-the art experimental apparta and sophisticated sample preparation procedures. An example of the later approach is a recent electron spin resonance study of 4-hydroxy-TEMPO in amorphous ice obtained by flash freezing water samples in glass capillaries[92].

The continuity conjecture described above has been the subject of considerable debate, primarily due to the fact that it excludes the possibility of anomalous variations in kinetic parameters (diffusivity, viscosity, relaxation time) near T_s. In particular, Angell and coworkers argued consistently that water may undergo an anomalous transition from a fragile to a strong liquid in the vicinity of T_s (see Figure 1.9, dashed line), and that postulated T_g of 136 K is incorrect, and must be reassigned to a higher value[93-95]. Recent experimental results provided further bases for this alternative argument. For example, Mullins and coworkers demonstrated that abnormally high values of water self-diffusivity

measured by Smith *et. al.* between 140 K and 160 K may be explained by rupturing of the ASW samples due to concurrent crystallization[96,97].

The continuity conjecture also seems to contradict the liquid-liquid phase transition hypothesis[98]. According to LLPT interpretation, T_s is a point of a relatively rapid change in the ratio of high and low density liquid (HDL and LDL) components of water due to isobaric (low pressure) crossing of the Widom line (supercritical fluctuations line) on water's phase diagram[98,99]. The contradiction arises partially from the possible nature of the LDL phase of liquid water.

According to the current models[98,100], the principle structural differences between LDL and HDL consist in the nature of hydrogen bond network. While HDL, a dominant phase of water at high temperatures, is characterized by a low degree of coordination of water molecules, LDL can be viewed as a cohesive tetrahedral hydrogen bond network[99], albeit one lacking long range order. In other words, a low density-low temperature phase of water is *ice-like* in terms of the average coordination of water molecules and, consequently, in terms of its transport and kinetic properties such self-diffusivity, viscosity, and relaxation time.

The LLPT hypothesis has recently received support from the results of the extensive studies of water confined in silica nanopores[99,101], where its crystallization is completely suppressed and, consequently, where it can be studied at temperatures near T_s. For instance, at temperatures *below* 224 K, water self-diffusivity and average translational relaxation time vary according to Arrhenius law, i.e., in a way similar to that in crystalline ice. Meanwhile, at temperatures above T_s, these parameters demonstrate a pronounced

"super-Arrhenius" behavior. According to the author's interpretation of FTIR spectra[99,102] of confined water, T_s is also characterized by a rapid rise in the LDL fraction (at lower temperatures). Thus, the observed temperature dependence of the kinetics and structure in confined water appears to be in contradiction with the continuity conjecture.

Although recent studies of water in confinement certainly shed light on the structure and physical properties of water in a previously inaccessible temperature range, one has to admit that these results may be a subject to critique based on a possible impact of confinement on water structure and properties. To summarize: in the framework of the discussion on dynamic properties of water under conditions of supercooling, there is a divided body of experimental evidence which makes it difficult to develop a comprehensive fundamental view of this extremely important condensed phase. While recent results seem to tip the balance in favor of the hypothesis postulating "strong-to-fragile" transitions near $T_{s,}$ the experimental evidence in contrast with such a view of supercooled water cannot be simply discarded or ignored. Thus, a program of experimental studies specifically designed to provide new experimental results on the dynamic and structural properties of supercooled water, and to investigate the possible fundamental causes of the disagreement would greatly benefit current theoretical trust toward better understanding of water's many unusual properties.

The principle scientific goals of the research program described in this dissertation are:

1. To facilitate development of a comprehensive fundamental description of water's thermodynamics and molecular kinetics by providing

experimental data on its properties in a previously inaccessible temperature range;

2. To gain insights into the molecular kinetics and structure of water in the vicinity of various hydrated chemical species;

3. To verify the results of recent studies of water in confinement;

4. To reconcile the results of past experimental studies which employed doped ASW samples with those obtained with pure ASW. In short, the experimental research described in this dissertation strives to eliminate gaps in the current understanding of the molecular dynamics and structure of water and aqueous solutions.

References

1. "Ice Physics and the Natural Environment" (ed. J. S. Wettlaufer, J. G. Dash & N. Untersteiner), pp. 11-22, NATO ASI Series I, vol. 56, Springer 1999.

2. Petrenko, V. F. and Whitworth, R. W. "Physics of Ice", (Oxford University Press, 1999).

3. Wettlaufer, J. S. "Ice Surfaces: Macroscopic effects of microscopic structure", *Phil. Trans. Roy. Soc. A*, 1999, 357, 1.

4. Tsai, V.C., and Wettlaufer, J. S. "Star patterns on lake ice", *Phys. Rev. E* 75, 066105 (2007)

5. Dash, J.G.; Rempel, A. W.; and Wettlaufer, J. S. "The physics of premelted ice and its geophysical consequences", *Rev. Mod. Phys.* 78, 695 (2006)

6. Sherwood, S. C.; Phillips, V. T. J.; Wettlaufer, J. S. "Small ice crystals and the climatology of lightning", *Geophys. Res. Lett.*, 33, L05804, doi:10.1029/2005GL025242 (2006).

7. "Glacier Science and Environmental Change", edited by P. Knight, Blackwell, Malden, MA, 2006.

8. Elmore, W. M. "Water purification by natural freezing", M. Sc. thesis, University of Wyoming, 1968.

9. "Physics of Ice-Covered Seas", edited by M. Leppranta, University of Helsinki Press, Helsinki, 1998, pp. 25–104.

10. Historical Perspectives of Frost Heave Research, Historical Perspectives in Frost Heave Research: The Early Works of S. Taber and G. Beskow, edited by P. B. Black and M. J. Hardenberg, CRREL Special Report No. 91-23 (CRREL, Hanover, NH, 1991), p. 37.

11. Oppenheimer, M. “Global warming and the stability of the West Antarctic Ice Sheet”, *Nature*, (London) 393, 325, (1998)

12. National Academy of Science, “Sea-Level Change” (National Academy Press, Washington, DC, 1990).

13. Rempel, A.W.; Wettlaufer, J. S.; Worster, M. G. Premelting dynamics in a continuum model of frost heave, *J. Fluid Mech.* 498, 227-44 (2004)

14. Grannas, A. M.; Jones, A. E.; Dibb, J.; Ammann, M.; Anastasio, C. et. al. “An overview of snow photochemistry: evidence, mechanisms and impacts”, *Atmospheric Chemistry and Physics* **7** (16): 4329-4373 2007.

15. Arguez, A.; Waple, A. M.; Sanchez-Lugo, A. M. State of the climate in 2006 BULLETIN OF THE AMERICAN METEOROLOGICAL SOCIETY **88** (6): S8-S135 Suppl. S JUN 2007.

16. “Climate change and trace gases” Author(s): Hansen J (Hansen, James), Sato M (Sato, Makix), Kharecha P (Kharecha, Pushker), Russell G (Russell, Gary), Lea DW (Lea, David W.), Siddall M (Siddall, Mark). PHILOSOPHICAL TRANSACTIONS OF THE ROYAL SOCIETY A-MATHEMATICAL PHYSICAL AND ENGINEERING SCIENCES **365** (1856): 1925-1954 JUL 15 2007.

17. Paull, C. K. (editor); Dillon, William P. (editor), 2000; Natural gas hydrates; occurrence, distribution, and detection. Geophysical Monograph 124, American Geophysical Union. Washington, D.C., United States. Pages: 315.

18. Bindschadler, R. Future of the west Antarctic ice sheet, *Science*, **282**, 428, (1998).

19. Zhang, R.; Leu, M. T.; Molina, M. Formation of polar stratospheric clouds on preactivated background aerosols, *Geophys. Res. Lett.* **23**, 1669, (1996).

20. Chalmers, B. "How water freezes", *Sci. Am.* **200** (2), 114, (1959).

21. Shultz, M. J.; Schnitzer, C.; Simonelli, D.; Baldelli, S. "Sum frequency generation spectroscopy of the aqueous interface: ionic and soluble molecular solutions" INTERNATIONAL REVIEWS IN PHYSICAL CHEMISTRY **19** (1): 123-153 JAN-MAR 2000.

22. Allen, H. C; Raymond, E. A., Richmond, G. L. "Nonlinear Vibrational Sum Frequency Spectroscopy of Atmospherically Relevant Molecules at Aqueous Solution Surfaces", Current Opinion in Colloid and Interface Science, 2000, **V5** (2), 74.

23. Wei X, Shen YR Vibrational spectroscopy of ice interfaces APPLIED PHYSICS B-LASERS AND OPTICS **74** (7-8): 617-620 MAY 2002

24. V. Buch, J. Sadlej, N. Aytemiz-Uras, and J. P. Devlin, "Solvation and ionization stages of HCl on ice nanocrystals", *J. Phys. Chem. A* **106**, 9374 (2002).

25. Ahmed, M.; Apps, C. J.; Hughes, C.; Watt, N. E.; Whitehead, J. C. "Adsorption of Organic Molecules on Large Water Clusters", *J. of Phys. Chem. A,* **1997**, 101, 1250.

26. Electrodynamic Trapping and Manipulation of Ice Crystals Brian D. Swanson, Neil Bacon, E. James Davis and Marcia B. Baker, (1999) Q. J. Roy. *Meteor. Soc*. **125**, 1039-58.

27. Davidovits, P; Kolb, C. E.; Williams, L. R., et. al. "Mass accommodation and chemical reactions at gas-liquid interfaces." *Chemical Reviews*. **106** (4): 1323-1354 APR 2006.

28. Glass, S.V.; Park S. C.; Nathanson, G. M. "Evaporation of water and uptake of HCl and HBr through hexanol films at the surface of supercooled sulfuric acid" *J. Phys. Chem. A*. **110** (24): 7593-7601 JUN 22 2006.

29. Hydrogen bonds in liquid water studied by photoelectron spectroscopy Author(s): Winter B (Winter, Bernd), Aziz EF (Aziz, Emad F.), Hergenhahn U (Hergenhahn, Uwe), Faubel M (Faubel, Manfred), Hertel IV (Hertel, Ingolf V.) Source: *J. Chem. Phys.* **126** (12): Art. No. 124504 MAR 28 2007.

30. McClure, S. M.; Barlow, E.T.; Akin, M. C.; Tanaka, P. L.; Safarik, D. J.; Truskett, T. M.; Mullins, C. B. Effect of dilute nitric acid on crystallization and fracture of amorphous solid water films *J. Phys. Chem. C.* **111** (28): 10438-10447 JUL 19 2007.

31. Sadtchenko, V.; Knutsen, K.; Gentry, W. R.; Giese, C. "Interaction of Hydrogen Chloride with Thin Ice Films: The Effect of Ice Morphology and Evidence for Unique Surface Species on Crystalline Vapor-Deposited Ice" *J. Phys. Chem. B*, **104**, 2511, 2000.

32. Sadtchenko, V.; Knutsen, K.; Gentry, W. R.; Giese, C. "Interactions of CCl_4 with Thin D_2O Amorphous Ice Films. 2. Variation of Desorption Kinetics with Ice Preparation Conditions and Evidence for Distinct Structures of Low-Density Amorphous Ice", *J. Phys. Chem. B*, **104**, 4894, 2000.

33. Sadtchenko, V.; Gentry, W. R.; Giese, C. "Interactions of CCl_4 with Thin D_2O Amorphous Ice Films, Part I: A Nanoscale Probe of Ice Morphology" *J. Phys. Chem. B*, **104**, 9421, 2000.

34. Graham, J. D.; Roberts, J. T.; Anderson, L. D.; Grassian, V. H. "The 367 nm Photochemistry of OClO Thin Films and OClO Adsorbed on Ice" *J. Phys. Chem.* **100**, 19551, 1996.

35. Graham, J. D.; Roberts, J. T. “Chemical reactions of organic molecules adsorbed at ice: 2. chloride substitution in 2-methyl-2-propanol” Langmuir, **16**, 3244, 2000.

36. Graham, J. D.; Roberts, J. T. “Chemical Reactions of Organic Molecules Adsorbed at Ice 1. Chlorine Addition to Propene” *J. Phys. Chem.* **104**, 978, 2000.

37. Graham, J. D.; Roberts, J. T. “Interactions of Hydrogen Chloride with an ultrathin ice film: observation of adsorbed and absorbed states” *J. Phys. Chem.*, **98**, 5974, 1994.

38. Livingston, F.E.; George, S.M. “Effect of HNO_3 and HCl on D_2O desorption kinetics from crystalline D_2O ice” *J. Phys. Chem. A*, **102**, 10280, 1998.

39. Livingston, F.E. and George, S. M. "Effect of HNO_3 and HCl on HDO diffusion on crystalline D_2O ice multilayers" *J. Phys. Chem. B*, **103**(21), 4366, 1999.

40. Foster, K.L.; Tolbert, M.A.; George, S.M. “Surface sensitive studies of the reactive uptake of chlorine nitrate on ice” *J. Phys. Chem. A*, 4979, 1997.

41. Berland, B.S.; Tolbert, M. A. and George, S. M. "Surface sensitive studies of the reactive uptake of chlorine nitrate on ice" *J. Phys. Chem. A*, **101**(51), 9954, 1997.

42. Andersson, Patrik U.; Ngrd, Mats B.; Pettersson, Jan B. C. “Molecular beam studies of HCl interactions with pure and HCl-covered ice surfaces” *J. Phys. Chem. B*, **104** (7), 1596, 2007.

43. Isakson, M. J.; Sitz, G. O. “Adsorption and desorption of HCl on ice” *J. Phys. Chem. A*, **103** (13), 2044, 1999.

44. 44 Bournel, F.; Mangeney, C.; Tronc, M.; Laffon, C.; Parent, P. “Acidity of hydrogen chloride at the surface of low-temperature (40-150 K) water-ice films” Phys. Rev. B, 2002, 65(20), 201404/1.

45. Haq, S.; Harnett, J.; Hodgson, A. "Adsorption and Solvation of HCl into Ice Surfaces" *J. Phys. Chem. B*, **106** (15), 3950, 2002.

46. Everest, M, A.; Pursell, C. J. "Isotope exchange of D2O on H2O ice: Surface versus bulk reactivity" *J. Chem. Phys.*, **115** (21), 9843, 2001.

47. Smith, R. S; Huang, C.; Wong, E. K. L.; Kay, B. D. "The molecular volcano: abrupt CCl_4 desorption driven by the crystallization of amorphous solid water" *Phys. Rev. Lett.* **79** (5), 909, 1997.

48. Osamu Mishima & H. Eugene Stanley, "The relationship between liquid, supercooled and glassy water", *Nature*, **396**, 329 (1998).

49. Lu, H.; McCartney, S. A.; Sadtchenko, V. "H/D Exchange Kinetics in Pure and HCl-Doped Polycrystalline Ice at Temperatures near Its Melting Point: Structure, Chemical Transport, and Phase Transitions at Grain Boundaries" *J. Chem. Phys.*, **130**, 054501 (2009).

50. 49. Lu, H.; McCartney, S. A.; Sadtchenko, V. "Fast Thermal Desorption Spectroscopy Study of H/D Isotopic Exchange Reaction in Polycrystalline Ice near Its Melting Point" *J. Chem. Phys.* **127**, 184701 (2007).

51. Sadtchenko, V. "Fast Thermal Desorption Spectroscopy and Ultrafast Microcalorimetry: New Tools to Uncover Mysteries of Ice" in "Physics and Chemistry of Ice", Royal Society of Chemistry, Cambridge, UK (2007).

52. Lu, H.; McCartney, S. A.; Chonde, M; Smyla, D.; Sadtchenko, V. "Fast Thermal Desorption Spectroscopy Study of Morphology and Vaporization Kinetics of Polycrystalline Ice Films" *J. Chem. Phys.* **125**, 044709 (2006).

53. Sadtchenko, V.; Brindza, M.; Chonde, M.; Palmore, B.; Eom, R. "The Vaporization Rate of Ice at Temperatures near Its Melting Point" *J. Chem. Phys.* **121**, 11980 (2004).

54. McCartney, S. A.; Sadtchenko, V. "Fast Scanning Calorimetry Studies of the Glass Transition in Doped Amorphous Solid Water: Evidence for the Existence of a Unique Vicinal Phase" *J. Chem. Phys*. submitted (2007).

55. Sadtchenko, V.; Lu, H.; McCartney, S. A. "Response to "Comment on `Glass transition in pure and doped amorphous solid: An ultrafast microcalorimetry study' [J. Chem. Phys. 125, 094501 (2006)]", *J. Chem. Phys.* **127**, 157102 (2007). NOTE: this reply describes results of extensive new experiments.

56. Brindza, M.; Chonde, M.; Sadtchenko, V. "Glass Transition in Pure and Doped Amorphous Solid Water: an Ultrafast Microcalorimetry Study" *J. Chem. Phys.* **125**, 094501(2006).

57. Weintraub, H.; Ashburner, M.; Goodfellow, P. N.; Lodish, H. F.; Arntzen, C. J.; Anderson, P. W.; Rice, T. M.; Geballe, T. H.; Means, A. R.; Ranney, H. M.; Cech, T. R.; Colwell, R. R.; Bourne, H. R.; Richter, B.; Singer, I. M.; Marrack, P.; Fearon, D. T.; Penzias, A.; Bard, A. J.; Brinkman, W. F.; Marks, P. A.; Vogelstein, B.; Kinzler, K. W.; Bishop, J. M.; Zare, R. N.; Schatz, G.; Benkovic, S. J.; Gray, H. B.; Valentine, J. S.; Crutzen, P. J.; Choi, D. W.; Nakanishi, S.; Kosslyn, S. M.; Brauman, J. I.; Rees, D. C.; Brill, W. J.; Schell, J.; Luhrmann, R.; Will, C. L.; Wulf, W.; Vermeij, G. J.; Arrow, K. J.; Smelser, N. J.; Anderson, D. L.; Abelson, P. H. *Science* **267**, 1609 (1995).

58. Johari, G. P. *J. Chem. Phys*. **112**, 10957 (2000).

59. Kashchiev, D. *Nucleation: Basic Theory with Applications* Butterworth-Heinemann: Oxford 2000.

60. Ediger, M. D.; Angell, C. A.; Nagel, S. R. *J. Phys. Chem*. **100**, 13200 (1996).

61. Kauzmann, W. *Chemical Reviews* **43**, 219 (1948).

62. Gupta, P. K.; Mauro, J. C. *J. Chem. Phys*. **126**, 9 (2007).

63. Angell, C. A. *Chemical Reviews* **102**, 2627 (2002).

64. Alba, C.; Busse, L. E.; List, D. J.; Angell, C. A. *J. Chem. Phys*. **92**, 617 (1990).

65. Minoguchi, A.; Richert, R.; Angell, C. A. *Phys. Rev. Lett*. **93**, 4 (2004).

66. Smith, R. S.; Dohnalek, Z.; Kimmel, G. A.; Stevenson, K. P.; Kay, B. D. *J. Chem. Phys.* **258**, 291 (2000).

67. Kurita, R.; Tanaka, H. *Phys. Rev. Lett*. **95**, 4 (2005).

68. Marques, M. I.; Stanley, H. E. *Physica A* **345**, 395 (2005).

69. Priya, M.; Das, S. P. *Phys. Rev. E* **76**, 8 (2007).

70. Scopigno, T.; Ruocco, G.; Sette, F.; Monaco, G. *Science* **302**, 849 2003.

71. Yannopoulos, S. N.; Johari, G. P. *Nature* **442**, E7 (2006).

72. Hodge, I. M. J. *Res. Natl. Inst. Stand. Technol*. **102**, 195 (1997).

73. Gibbs, J. A. a. J. H. *J. Chem. Phys*. **45** (1965).

74. Angell, C. A. *Annu. Rev. Phys. Chem*. **55**, 559 (2004).

75. Johari, G. P. *J. Phys. Chem. B* **102**, 4711 (1998).

76. R Smith, Z. D., G. Kimmel, G. Teeter, B. Kay. *Water in confining geometries*; eds. V. Bush, P. Devlin, Cluster Physics, Springer, New-York 2003.

77. Dohnalek, Z.; Kimmel, G. A.; Ayotte, P.; Smith, R. S.; Kay, B. D. *J. Chem. Phys*.**118**, 364 (2003).

78. Speedy, R. J.; Debenedetti, P. G.; Smith, R. S.; Huang, C.; Kay, B. D. *J. Chem. Phys*. **105**, 240 (1996).

79. Angell, C. A.; Oguni, M.; Sichina, W. J. "Heat-Capacity Of Water At Extremes Of Supercooling And Superheating" *J. Phys. Chem.* **86**, 998, 1982.

80. Debenedetti, P. G.; Stanley, H. E. "Supercooled and glassy water" *Phys. Today* **56**, 40, 2003.

81. Mishima, O.; Stanley, H. E. "The relationship between liquid, supercooled and glassy water" *Nature* **396**, 329, 1998.

82. Speedy, R. J. "Stability limit conjecture an interpretation of properties of water" *J. Phys. Chem.* **86**, 982, 1982.

83. Sastry, S.; Debenedetti, P. G.; Sciortino, F.; Stanley, H. E. "Singularity-free interpretation of the thermodynamics of supercooled water" *Phys. Rev. E* **53**, 6144, 1996.

84. Poole, P. H.; Sciortino, F.; Essmann, U.; Stanley, H. E. "Phase behavior of metastable water" *Nature* **360**, 324, 1992.

85. Johari, G. P.; Fleissner, G.; Hallbrucker, A.; Mayer, E. "Thermodynamic Continuity between Glassy And Normal Water" *J. Phys. Chem.* **98**, 4719, 1994.

86. Speedy, R. J.; Debenedetti, P. G.; Smith, R. S.; Huang, C.; Kay, B. D. "The evaporation rate, free energy, and entropy of amorphous water at 150 K" *J. Chem. Phys.* **105**, 240, 1996.

87. Hallbrucker, A.; Mayer, E.; Johari, G. P. "Glass-Liquid Transition And The Enthalpy Of Devitrification Of Annealed Vapor-Deposited Amorphous Solid Water - A Comparison With Hyperquenched Glassy Water" *J. Phys. Chem.* **93**, 4986, 1989.

88. Johari, G. P. "Water's character from dielectric relaxation above its T-g" *J. Chem. Phys.* **105**, 7079, 1996.

89. Smith, R. S.; Dohnalek, Z.; Kimmel, G. A.; Stevenson, K. P.; Kay, B. D. "The self-diffusivity of amorphous solid water near 150 K" *Chem. Phys.* **258**, 291, 2000.

90. Johari, G. P. "Liquid state of low-density pressure-amorphized ice above its T-g" *J. Phys. Chem. B* **102**, 4711, 1998.

91. Drobyshev, A.; Aldiyarov, A.; Zhumagaliuly, D.; Kurnosov, V.; Tokmoldin, N. "Thermally stimulated transformations in cryovacuum water ices" *Low Temp. Phys.* **33**, 355, 2007.

92. Bhat, S. N.; Sharma, A.; Bhat, S. V. "Vitrification and glass transition of water: Insights from spin probe ESR" *Phys. Rev. Lett.* **95**, 4, 2005.

93. Angell, C. A. "Insights into phases of liquid water from study of its unusual glass-forming properties" *Science* **319**, 582, 2008.

94. Angell, C. A. "Amorphous water" *Annu. Rev. Phys. Chem.* **55**, 559, 2004.

95. Giovambattista, N.; Angell, C. A.; Sciortino, F.; Stanley, H. E. "Glass-transition temperature of water: A simulation study" *Phys. Rev. Lett.* **93**, 4, 2004.

96. McClure, S. M.; Barlow, E. T.; Akin, M. C.; Safarik, D. J.; Truskett, T. M.; Mullins, C. B. "Transport in amorphous solid water films: Implications for self-diffusivity" *J. Phys. Chem. B* **110**, 17987, 2006.

97. McClure, S. M.; Safarik, D. J.; Truskett, T. M.; Mullins, C. B. "Evidence that amorphous water below 160 K is not a fragile liquid" *J. Phys. Chem. B* **110**, 11033, 2006.

98. Stanley, H. E.; Kumar, P.; Franzese, G.; Xu, L.; Yan, Z.; Mazza, M. G.; Buldyrev, S. V.; Chen, S. H.; Mallamace, F. "Liquid polyamorphism: Possible relation to the anomalous behaviour of water" *Eur. Phys. J.-Spec. Top.* **161**, 1, 2008.

99. Mallamace, F.; Branca, C.; Broccio, M.; Corsaro, C.; Gonzalez-Segredo, N.; Spooren, J.; Stanley, H. E.; Chen, S. H. "For review see: Transport properties of supercooled confined water" *Eur. Phys. J.-Spec. Top.* **161**, 19, 2008.

100. Shiratani, E.; Sasai, M. "Molecular scale precursor of the liquid-liquid phase transition of water" *J. Chem. Phys.* **108**, 3264, 1998.

101. Oguni, M.; Maruyama, S.; Wakabayashi, K.; Nagoe, A. "Glass transitions of ordinary and heavy water within silica-gel nanopores" *Chem.-Asian J.* **2**, 514, 2007.

102. Mallamace, F.; Broccio, M.; Corsaro, C.; Faraone, A.; Majolino, D.; Venuti, V.; Liu, L.; Mou, C. Y.; Chen, S. H. "Evidence of the existence of the low-density liquid phase in supercooled, confined water" *Proc. Natl. Acad. Sci. U. S. A.* **104**, 424, 2007.

Chapter 2: Experimental Techniques: Fast Scanning Calorimetry

2.1 Experimental apparatus

2.1.1 Outline

The outline of the experimental apparatus for fast scanning calorimetry (FSC) studies of the glass transition in amorphous solid water (ASW) films is shown in Figure 2.1. The calorimeter consists of a filament array (up to 3 filaments) which is mounted on a LN-cooled support block. The ends of the filaments are clamped between flat resistive heaters and 0.5 mm thick sapphire plates on top of the support block. The sapphire plates electrically isolate the filament array from the rest of the apparatus, while maintaining a good thermal contact with the LN-cooled support block. The resistive heaters are capable of generating up to 10 W of power and are used to adjust the temperature of the entire filament support during deposition from 110 K to 170 K by carefully balancing the heating of the block with the resistive heaters against the cooling of the LN. Two T-type thermocouples glued to the surface of the support block measure the temperature of the filament support assembly during ASW film deposition.

The calorimeter is positioned inside a high vacuum chamber, pumped with a 1500 L/s turbomolecular pump and a diffusion pump. The diffusion pump is capped with a LN baffle to prevent the oil from back streaming into the calorimeter chamber and to increase the effective pumping speed of the vacuum system in respect to water and other volatiles.

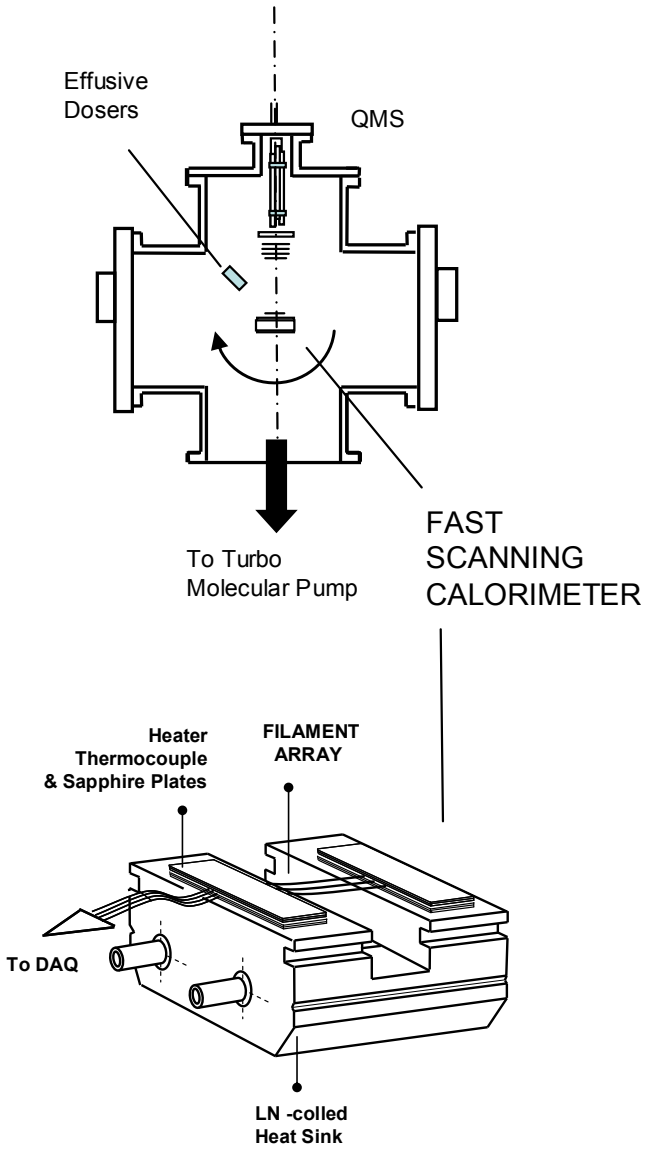

Figure 2.1. The outline of the experimental apparatus. The calorimeter consists of a filament array which is mounted on a LN-cooled support block. The ends of the filament are clamped between flat resistive heaters and 0.5 mm thick sapphire plates. The temperature of the filament support assembly is measured with two T-type thermocouples. The calorimeter is situated inside a high vacuum chamber that maintains a pressure of $5 * 10^{-7}$ Torr. A QMS is ~10 cm above the filament array measures the vaporization fluxes of volatiles during experiments.

During experiments, both pumps are typically used to maintain an oil-free pressure inside the calorimetry chamber at 5 * 10^{-7} Torr. The pressure inside the chamber is measured with an ion gauge.

2.1.2 Detector

The calorimetry chamber is equipped with a quadrupole mass spectrometer (QMS) to monitor and analyze vaporization products in FSC experiments. The QMS is a residual gas analyzer (RGA 300, Stanford Research Instruments), which is placed ~10 cm above the filament array inside the calorimetry chamber. The QMS is used to measure the vaporization fluxes of volatiles from the filament array in a manner similar to traditional temperature-programmed desorption studies[1]. Fast thermal desorption spectra, i.e., the mass spectrometer signal variations with time during film vaporization, are recorded at various masses to calculate the mole fractions of dopants in the doped-ASW films. The relative uncertainty of these determinations is on the order of 5%.

The mass-to-charge ratio (m/z) used to detect water and each dopant molecule was chosen using the highest relative abundance peak from their respective mass spectra. Figure 2.2 shows the mass spectrum of water[2]. Although peaks appear at m/z = 16, 17, 18, 19, and 20, the peak with the highest relative abundance is at m/z = 18. When the QMS is tuned to this mass-to-charge ratio, it has the greatest detection sensitivity to water desorbing from the film.

In a doped ASW sample, the ratio of dopant molecule to ASW molecules can be determined by integrating the area under the detector curves for both molecules and then calculating the ratio. For example, Figure 2.3 shows the detector data obtained for an ASW

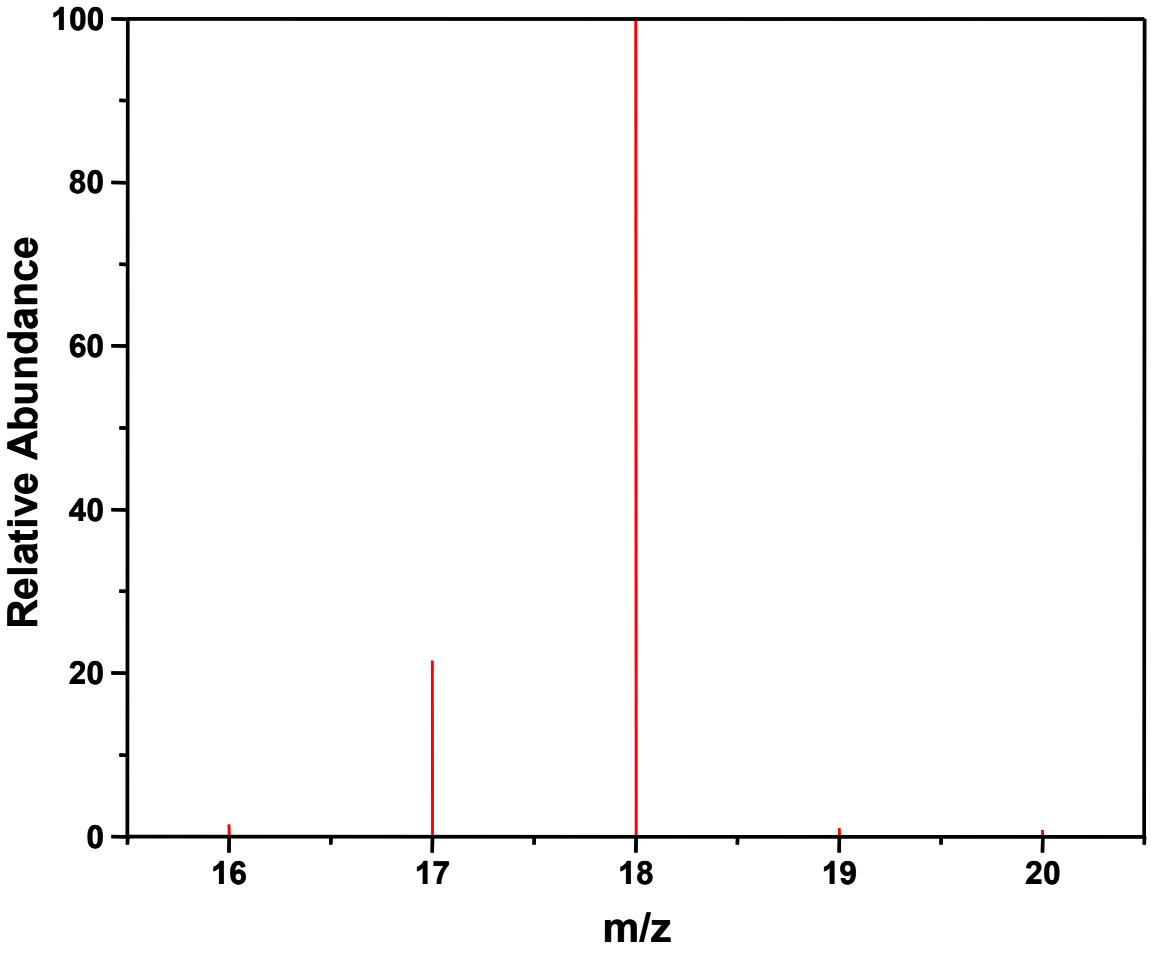

Figure 2.2. The mass spectrum of water.

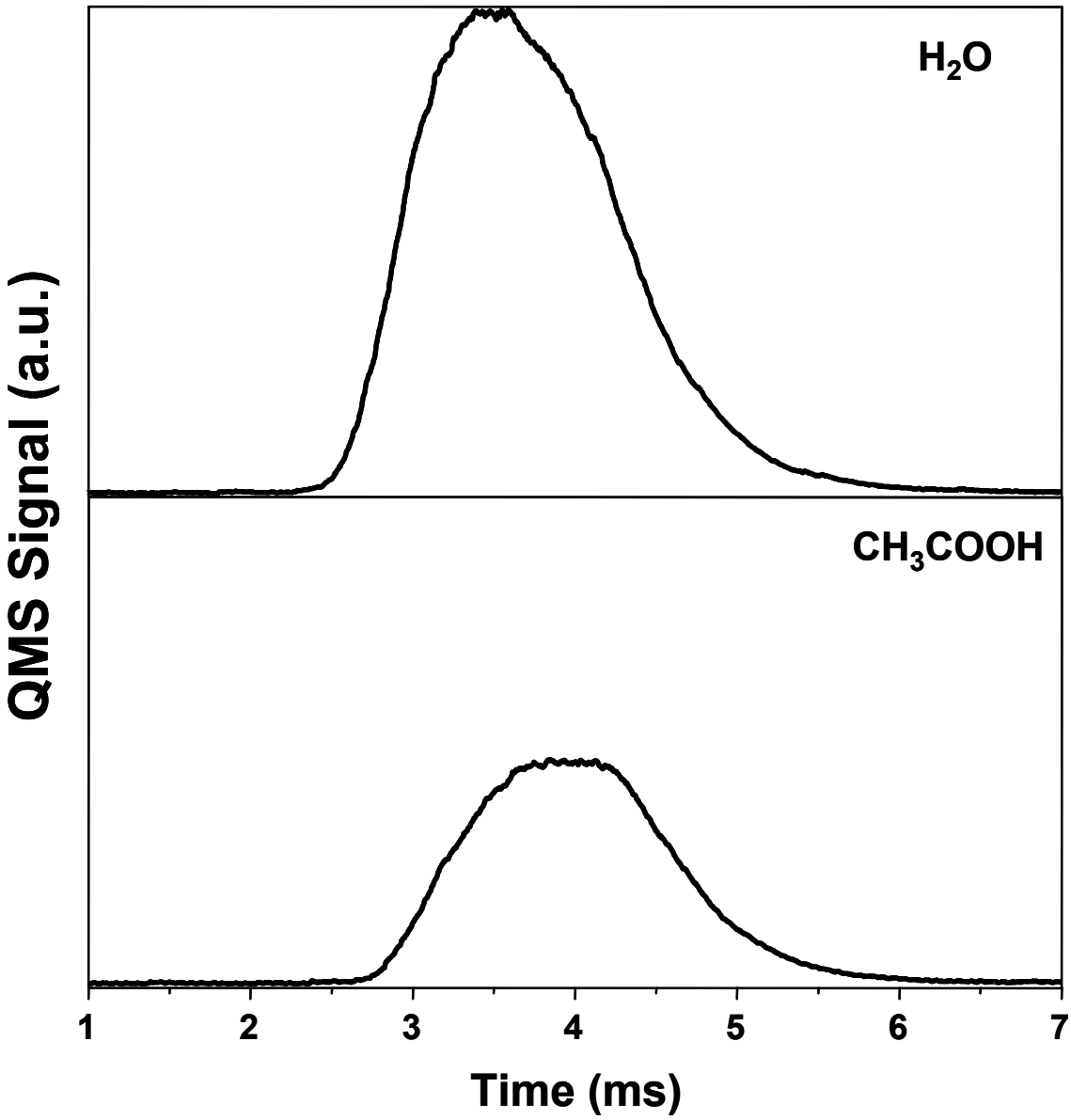

Figure 2.3. The detector signal obtained for an ASW film doped with CH_3COOH. The ratio of water molecules to acetic acid molecules can be calculated by integrating the area under the curves and dividing the values.

film doped with acetic acid. By integrating the area under the curves, the ratio for this sample was calculated to be 0.18, i.e., 2 acetic acid molecules for every 11 water molecules.

2.1.3 Vapor Deposition System

The vapor deposition system (schematic found in Figure 2.4) for the preparation of the ASW films consists of two independent stainless steel tubes terminated by solenoid valves. The valves are positioned approximately 4 cm above the filament array.

The vapor sources (H_2O, CH_3COOH, etc.) are vials filled with volatile liquid and maintained at temperatures near 14 °C. Each vial is also connected to a mechanical pump via a LN trap to ensure that the vapor source is constantly pumped during all stages of the experiment. Pumping on the vapor lines creates two advantages. First, the source vacuum system ensures that there is no buildup of background pressures in the vapor source during the time delays between experiments. Second, actively pumping on the vapor source prevents vapor flux surges during the first few seconds of film deposition.

In the case of ASW films doped with miscible volatile liquids, i.e., acetic acid, ethanol, etc., the vapor line is connected to a glass bulb containing a pre-mixed dopant/water solution. In other words, the vapors of both liquids were pre-mixed prior to deposition on the filament's surface.

In the case of ASW films doped with immiscible volatile liquids, i.e., pentanol, carbon tetrachloride, etc., a separate vapor source is utilized to co-deposit water vapor with the immiscible liquid vapor directly onto the filament. A separate vapor line for these

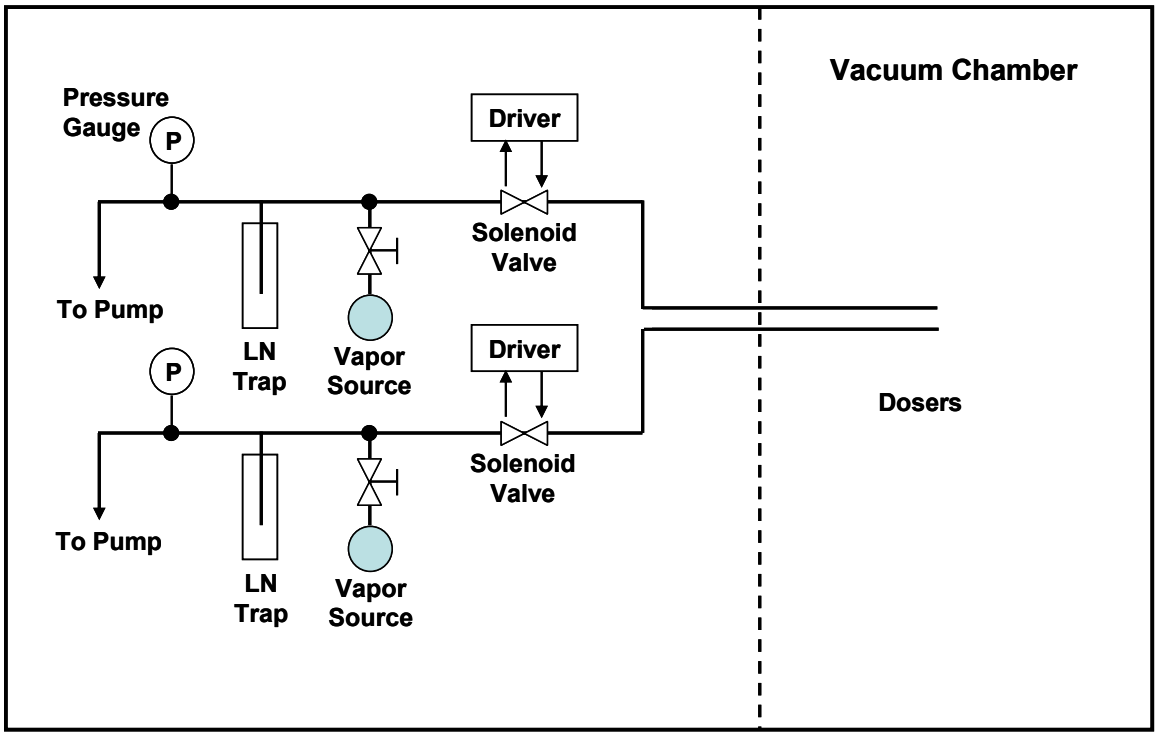

Figure 2.4. The outline of the vapor deposition system. This system consists of two independent stainless steel tubes terminated by solenoid valves. The valves are positioned 4 cm above the filament array. The vapor sources for each line are vials filled with volatile liquids and maintained at a temperature of 14 °C. Each vial is also connected to a mechanical pump via a LN trap to ensure that the vapor source is constantly pumped during all stages of the experiment. In the case of ASW films doped with miscible volatile liquids, the vapor line is connected to a glass bulb containing a pre-mixed dopant/water solution. In the case of ASW films doped with immiscible volatile liquids, a separate vapor source is utilized to co-deposit water vapor with the immiscible liquid vapor directly onto the filament.

experiments facilitated better control over dopant concentration within the doped ASW film.

The performance of the vapor deposition system is routinely monitored before beginning and in between experiments. Essential calibration procedures, which are discussed in Section 2.3, rely extensively on FSC and mass spectrometry for the determination of the ASW film's overall thickness and chemical composition. The general capabilities of the vapor deposition are:

1. Sample growth rate is estimated as 10 to 20 nm/s.
2. Long-term deposition rate stability is 2 nm/s*hr.
3. Accuracy of ultrathin layer deposition (short term fluctuations) is ±0.5 nm for films with thicknesses from 5 to 50 nm.

2.1.4 Data Acquisition and Process Control System

The data acquisition and process control system (DAQPC) are based on a single PC that contains a plug-in general purpose data acquisition board (National Instruments). This board is controlled by a specially designed LabView program, which fully automates all stages of the experiments. A schematic of the essential components and signal flow of the DAQPC system is illustrated in Figure 2.5.

The experimental parameters such as vapor deposition time and sequence are input by the computer operator. The valve drivers of the vapor deposition system are engaged by several timed TTL pulses from the DAQ board. Upon completion of film deposition, the

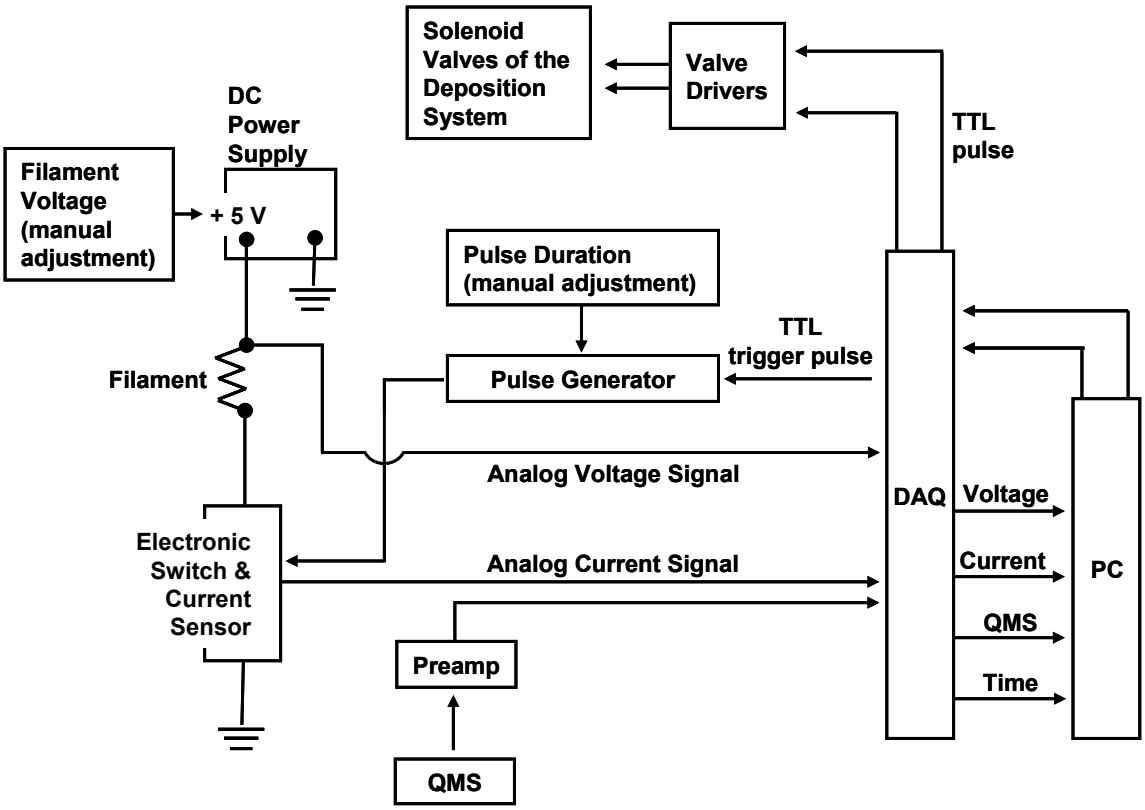

Figure 2.5. The outline of the data acquisition and process control system (DAQPC). An experiment begins when the vapor deposition time and sequence are input into the LabView program on the PC. The valve drivers of the vapor deposition system are engaged by several timed TTL pulses from the DAQ board. Upon completion of the film deposition, the FSC scan is initiated by a TTL trigger pulse to a standalone pulse generator. The generator closes the electronic switch of the filament circuit and sends an electric current through the filament. After the ASW film vaporizes, the voltage, current, and QMS signals are collected by the DAQ and sent to the PC.

FSC scan is initiated by a TTL trigger pulse to a standalone pulse generator (Exact Electronics). The generator closes the electronic switch of the filament circuit by emitting a single square pulse and, thus, sending an electrical current through the filament. Variables such as the pulse duration, its amplitude, and voltage offset can be manually adjusted directly on the pulse generator. The pulse duration ultimately determines the overall timescale of the FSC experiment, which can be varied from a few microseconds to 40 milliseconds.

A schematic of the electronic switch and current measurement circuit can be found in Figure 2.6. The electronic switch is essentially comprised of two *pnp* transistors, whose primary base input is terminated with a 10 kΩ resistor. The circuit is designed to minimize current leaks through the filament at base voltages below 2 V, while allowing the adjustment of current through the filament by the base voltage waveform with amplitudes above 2 V. The other circuitry components were selected to create a characteristic response time for the switch to be less than one microsecond.

The current measurement sensor in the circuit found in Figure 2.6 is designed around a single operational amplifier (TI OpAmp 749 or similar), which is utilized to monitor the voltage drop across a 0.5 Ω shunt resistor (R_{sense}). The bandwidth of the amplifier is ~3 MHz. The current sensor is calibrated using a resistor with a known value to facilitate software conversion of voltage drop data at R_{sense} into current values. The current and voltage waveforms from the filament are sent to a differential analog input of the DAQ board and are stored in the on-board memory buffer after analog-to-digital (ADC) conversion.

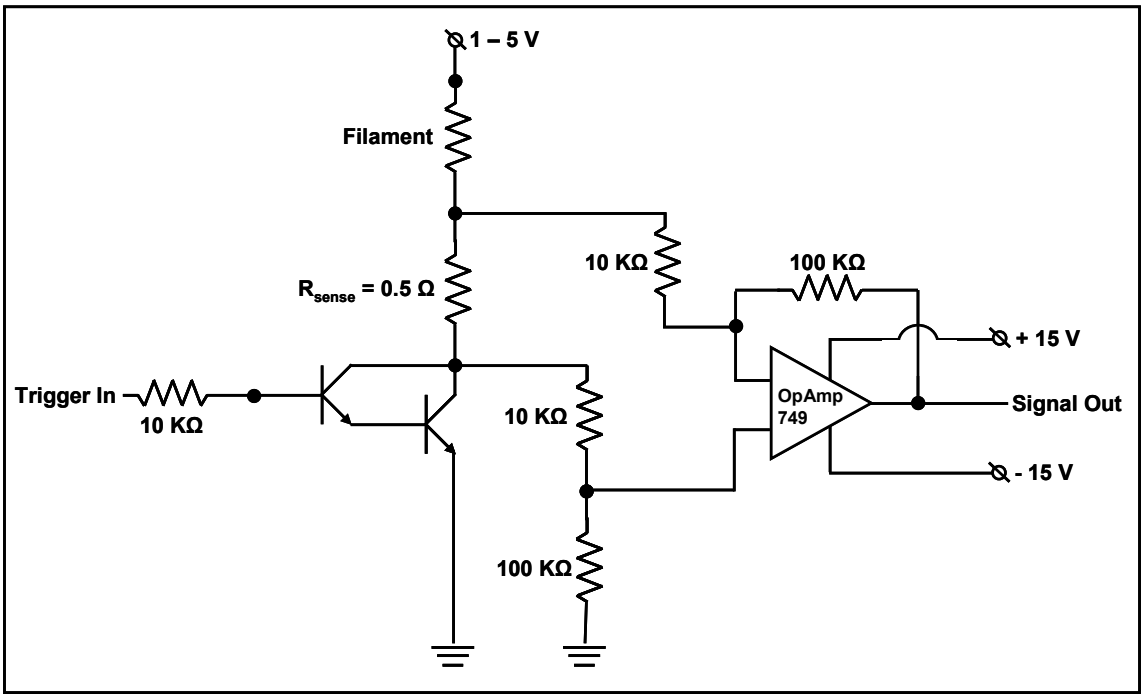

Figure 2.6. The schematic of the electronic switch and current measurement circuit. The electronic switch is essentially comprised of two pnp transistors, whose primary base input is terminated with a 10 kΩ resistor. The current measurement sensor in the circuit is designed around a single operational amplifier (TI OpAmp 749 or similar), which is utilized to monitor the voltage drop across a 0.5 Ω shunt resistor (R_{sense}). The current and voltage waveforms from the filament are sent to a differential analog input of the DAQ board and are stored in the on-board memory buffer after analog-to-digital (ADC) conversion.

The analog voltage signals from the QMS detector are preamplified, then digitized by ADC of the DAQ board The overall time resolution of the DAQ system is one microsecond per channel (current, voltage, and QMS).

2.2 Fundamentals of a Fast Scanning Calorimetry Experiment: Technique Demonstration and Critical Tests

Prior to a USC experiment, the filament is flashed several times to 800 – 1500 °C for a few milliseconds in order to ensure that any volatile contaminants are removed from the substrate's surface. After baking the filament, it is allowed to cool (over several seconds) to the chosen deposition temperature i.e., 110 K to 130 K.

Each experiment is initiated by depositing water vapor to form an ASW film. The deposition takes between 10 s and 300 s depending on the specific experiment. Upon completion of deposition, a delay of 5 to 10 s allows the excess water vapor within the chamber to be evacuated and regain its usual background pressure.

After deposition, a 1.5 V to 7.0 V potential difference is applied across the filament to initiate rapid isothermal desorption of the ASW film. The DAQPC system records the voltage across the filament and the current through the filament every 4 μs over the entire timescale of the experiment, i.e., for 10 – 40 ms. Figure 2.7 illustrates the voltage and current data collected for a 1 μm thick ASW film that was desorbed using a heating rate of 10^5 K/s. With this data, the effective resistance of the film/filament system is calculated using Ohm's Law (Figure 2.8).

In order to determine the most accurate resistance values, the current data undergoes a thorough calibration procedure. In order to calibrate the current, a "dummy

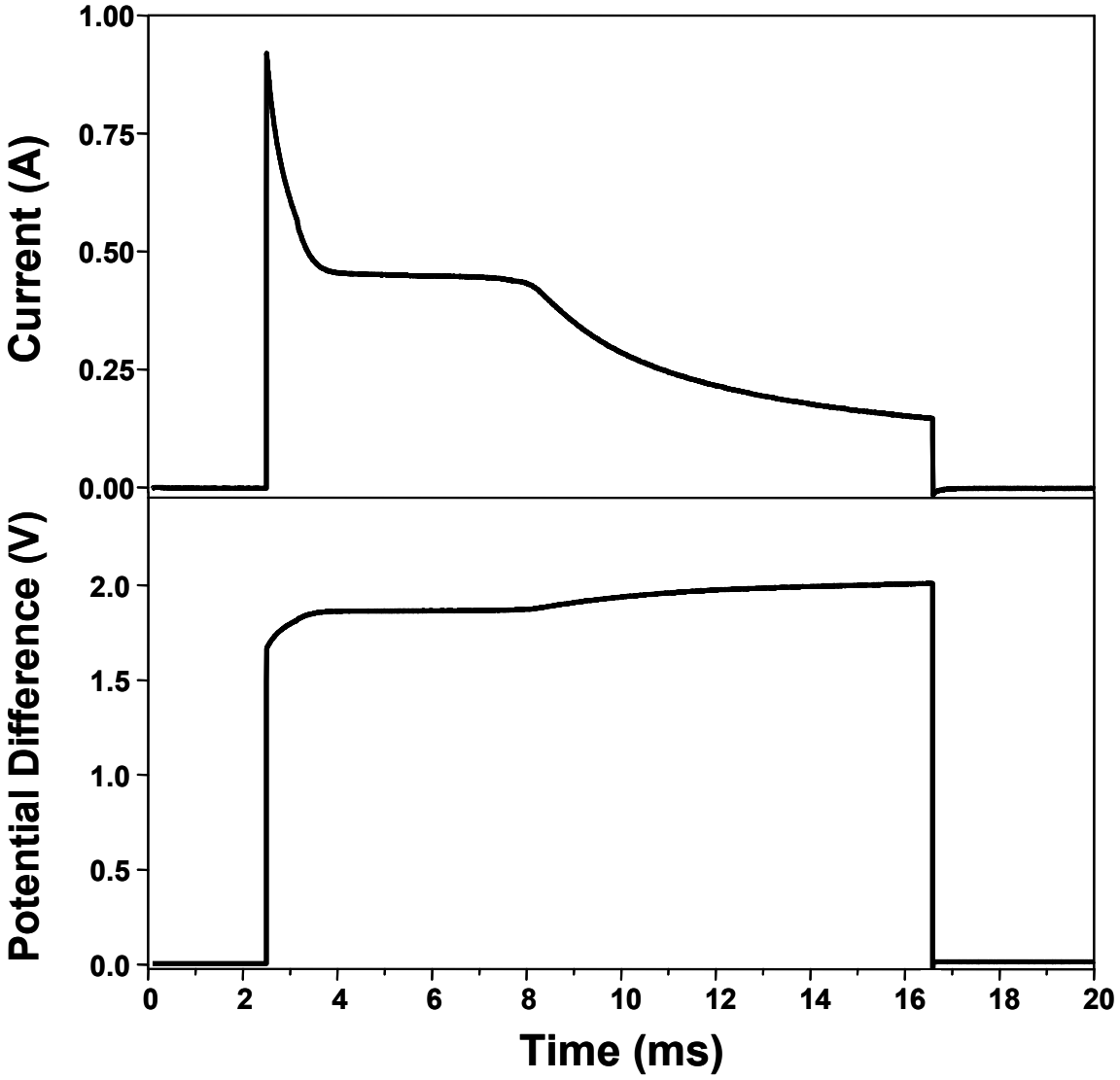

Figure 2.7. The current (upper panel) and voltage (lower panel) data collected for a 1 μm thick ASW film that was desorbed using a heating rate of 10^5 K/s.

resistor" with a known resistance (10 Ω) is connected to the DAQPC system in lieu of the tungsten filament. Potential differences ranging from 1.5 V to 7.0 V are applied across the "dummy resistor" and the current data is recorded. Using this current and voltage data along with the known resistance of the dummy resistor, the actual current through the resistor, and subsequently the filament, is calculated, and used to determine the resistance of the film/filament system.

The temperature of the film/filament system in Figure 2.8 is calculated using Equation 1:

$$T(R) = T_0 - \left(\frac{1}{\alpha}\right)\left(1 - \frac{R - R_p}{R_0 - R_p}\right) \tag{2.1}$$

where α is the temperature coefficient of electrical resistivity of tungsten $(0.0045\ °C^{-1})$[3], R_0 is the effective filament resistance at a known temperature T_0, and R_p is an empirical parameter. The empirical parameter, R_p, is included in Equation 2.1 in order to account for the "parasitic" resistances of the wire connections from the filament to the DAQ board and the nonlinearities in the dependence of filament resistances on temperature.

The conversion of resistance data into temperature values of the film/filament system requires accurate measurements of the effective filament resistance, R_0, at a specific temperature T_0; therefore, a point calibration is performed daily before beginning experiments. The calibration is performed by several sequential steps. First, the resistance of the filament ($R_{ambient}$) is determined with a multimeter at ambient temperatures ($T_{ambient}$). The value of $T_{ambient}$ is that temperature measured by the thermocouples before cooling the filament assembly with liquid nitrogen. Next, the resistance of the filament (R_{cryo}) is measured after balancing the heating of the filament assembly via its resistors with the

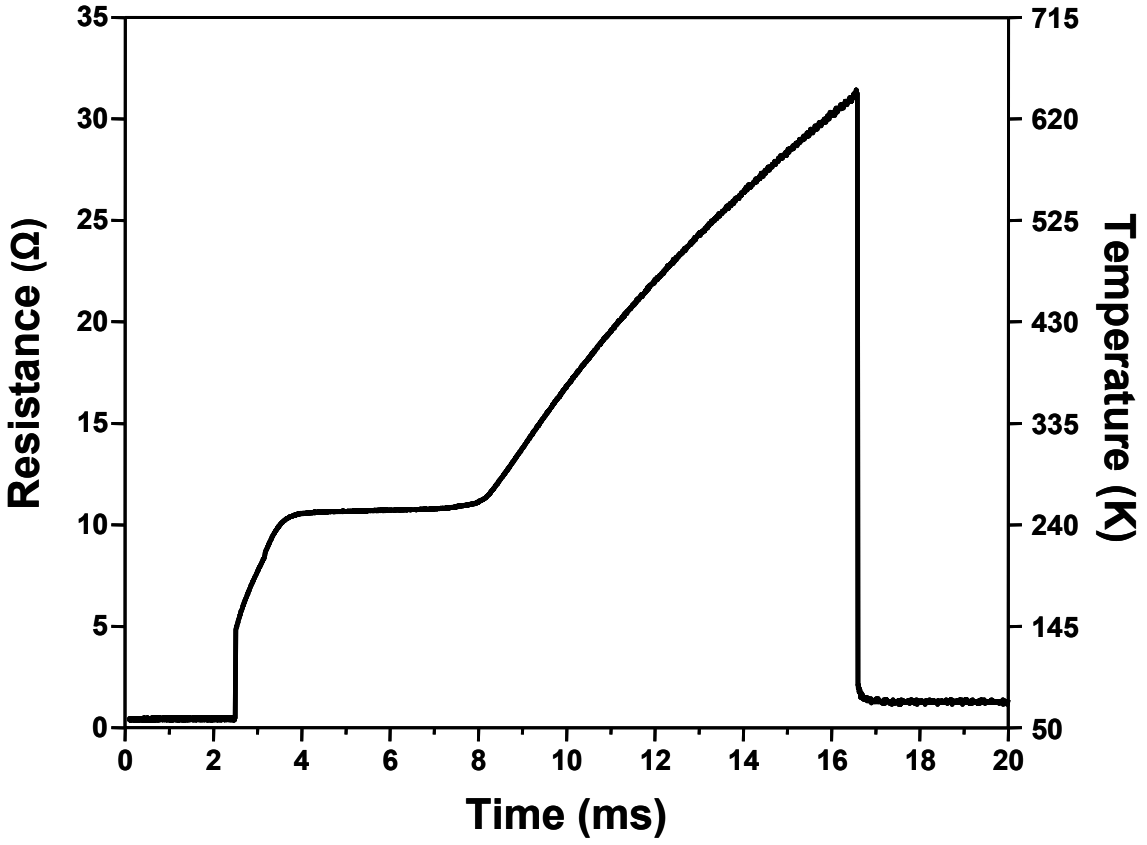

Figure 2.8. Using Ohm's Law and its corollary (Equation 2.1), the current and voltage data (from Figure 2.7) can be used to calculate the resistance and temperature of the film/filament system.

cooling of liquid nitrogen to reach the desired deposition temperature (T_{cryo}). With these four measurements, Equation 2.1 can be solved to determine the value of R_p. Finally, with the value of the empirical parameter, the temperature of the filament is calculated using Equation 1 using $T_{ambient}$ and $R_{ambient}$ in place of T_0 and R_0, respectively.

The validity of resistance-based temperature calculations were thoroughly studied and verified by Palmore and Lu using fast thermal desorption spectroscopy (FTDS)[1,4,5]. The temperature values are calculated from the filament resistance according to Equation 1 for every experiment. In order to determine the accuracy of these calculations, a value of the effective filament resistance at a known temperature is obtained. With the known value of $T_{melting}$ (273 K) and the resistance value measured during the melting of the ice film, $R_{melting}$ (13.2 Ω), the temperature of the filament near its surface can be determined with a precision of ± 1.5 K. Palmore and Lu estimated the overall precision of the filament temperature measurements (± 1.5 K) by comparing the temperature values for the entire filament assembly measured with the filament acting as a resistance temperature device and those measured with the thermocouples attached to the filament support block[1,4,5].

Figure 2.9 shows the typical results when a potential voltage of a few volts is applied across the filament when it is both bare and covered with an ASW film. In both cases there is a rapid rise in the temperature; however, in the case of an ASW-covered filament, the heating rate is significantly slower and shows a number of inflection points, which are indicative of thermal transitions in the ASW film/filament system. Thus, Figure 2.9 demonstrates that heating rates on the order of 10^5 K/s are attainable this experimental setup.

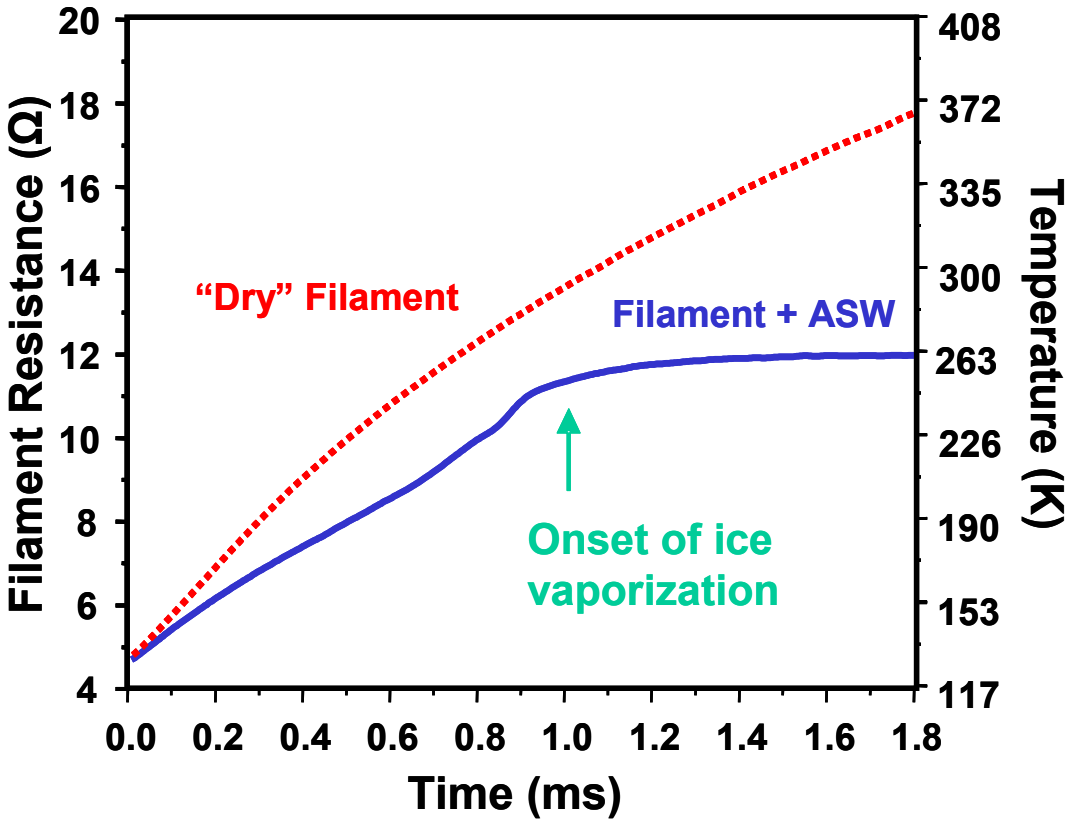

Figure 2.9. Resistance and corresponding temperature of the filament during rapid heating. The solid line shows resistance of the filament covered by a 1 μm thick ASW film. The resistance of an ice-free filament is shown for comparison. In the case of the ice-covered filament, the heating rate is lower, and the heating curve shows a number of inflection points indicative of multiple exo- or endothermic transitions in the ASW film/filament system. The data demonstrate that heating rates up to 105 K/s are easily accessible with the experimental setup and that the sensitivity of the calorimeter is sufficient to detect exo- and endothermic transitions in thin films of amorphous ice used in our experiments.

As shown in Figure 2.9, the rapid rise in temperature during the first few milliseconds of the experiment is followed by a region where the temperature of the ASW film-filament system is nearly constant ($\Delta T < 1$ K). As described by Lu, this is due to the onset of rapid vaporization of the ASW film, which follows zero-order kinetics[1,5]. Essential conclusions from the observation of zero-order kinetics are listed immediately below.

1. ASW films grown under the pre-stated conditions have a neat cylindrical geometry, which fully covers the entire filament surface. Upon rapid vaporization near 0°C, the film does *not* collapse into clusters or droplets on the timescale of the experiment. Indeed, any such changes in the overall geometry of the ASW film would result in nonzero-order kinetics and a rapid increase in the temperature.

2. The longitudinal temperature gradient during vaporization is negligible except within a fraction of a millimeter near the ends of the filament. If there were any "warmer" sections of the filament, it would vaporize at a greater rate, leading to changes in the overall surface area of the film, which would again result in nonzero-order kinetics.

3. The transverse temperature gradient, i.e., the temperature gradient through the ASW film, is less than a few degrees per micrometer. If there

were a significant gradient through the film, then there would be a significant increase in the temperature of the ASW film surface during vaporization and again result in nonzero-order kinetics.

The effective heat capacity of the ASW film/filament system is calculated as the ratio of the power generated by the filament to the first time derivative of the temperature. Assuming that the film has the specific heat capacity and density of hexagonal ice, and that the vapor deposited ASW forms a neat film along the entire surface of the filament, then the data obtained from heat capacity thermograms makes it possible to obtain a good estimate of the ice film's overall thickness and mass. For example, Figure 2.10 shows the effective heat capacity of the "dry" filament and an ice film vapor deposited at 120K and then annealed by raising the temperature to 240 K for 5 ms. Analysis of the data determines that the film was 2.2 ± 0.3 μm thick. With this value and the total deposition time, the deposition rate of H_2O on the filament's surface is approximately 11 nm/s or ~30 hexagonal ice monolayers per second.

Figure 2.11 shows thermograms of ASW films prepared at varying deposition temperatures. The mass of the films was nearly identical and each had a thickness of 1.0 ± 0.1 μm. The lower panel shows the thermogram of an ASW film vapor deposited at 110 K. The heating rate was (1.3 ± 0.2) $*10^5$ K/s. The scan reveals three exothermic features marked as A, B, and C at 200, 210, and 220 K, respectively. The middle panel of Figure 2.11 shows the thermogram of ASW film vapor deposited at 140 K. While an increase in the deposition temperature did not lead to noticeable changes in the magnitude or position

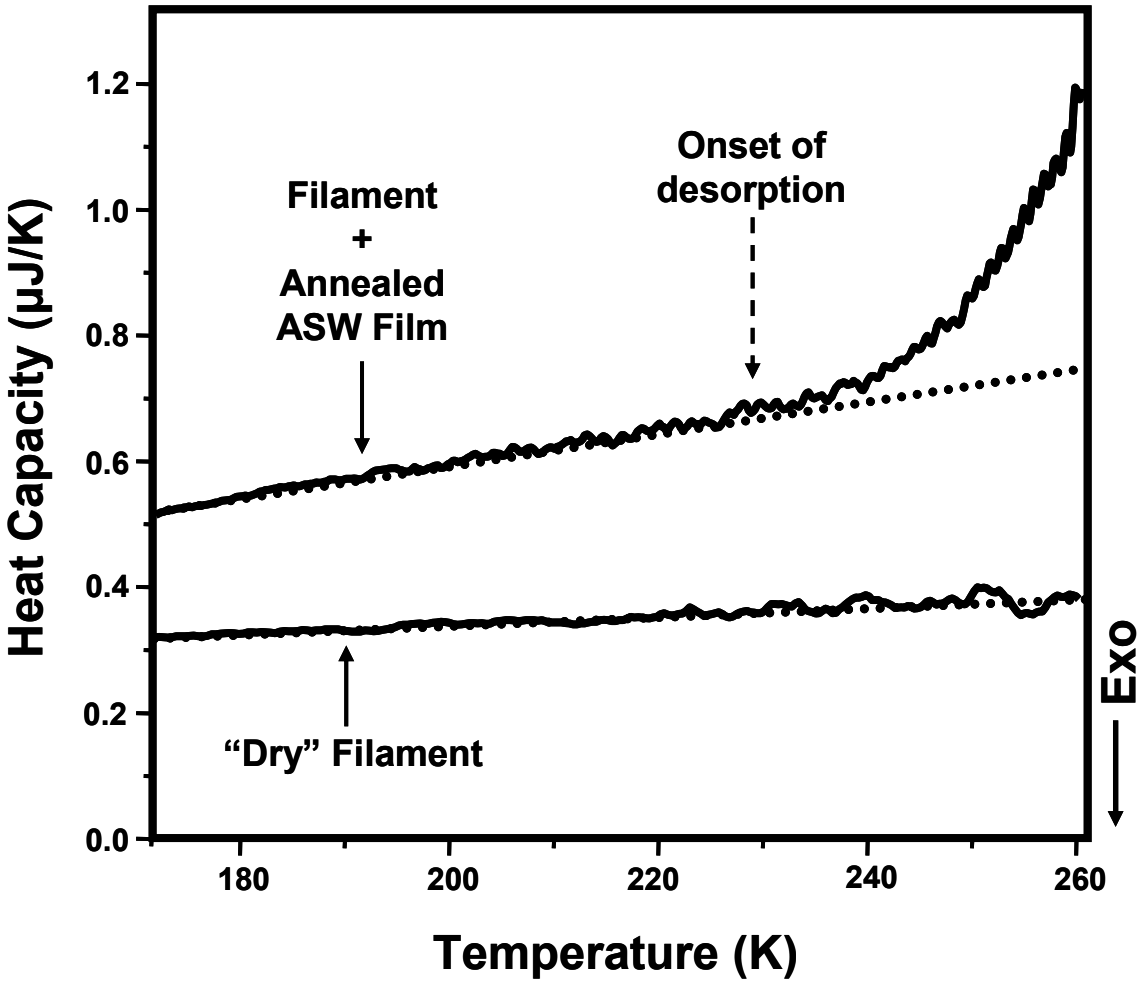

Figure 2.10. The effective heat capacity of the bare filament and an ice film vapor deposited at 120K and, then, annealed by raising the temperature to 240 K for 5 ms. The data obtained from heat capacity thermograms makes it possible to obtain a good estimate of the ice film's overall thickness and mass. For this particular thermogram, the film was 2.2 ± 0.3 μm thick.

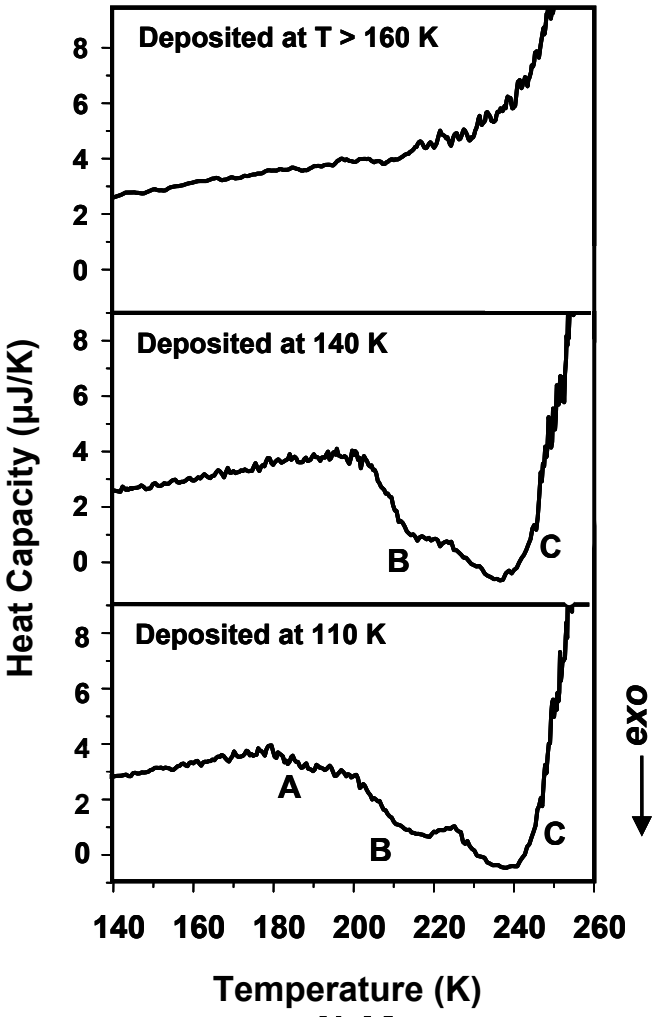

Figure 2.11. FSC thermograms of vapor deposited ASW films prepared under various conditions. The heating rate is (1.3 ± 0.2) *10^5 K/s. The mass of all three films is nearly identical and corresponds to a film thickness of 1.0 ± 0.1 μm. Lower panel: the thermogram of an ASW film vapor deposited at 110 K. Middle panel: the thermogram of ASW film vapor deposited at 140 K. Top panel: the thermogram of a film deposited at 170 K. The endothermic upswing in the heat capacity at temperatures above 250 K, present in all three thermograms, is due to the onset of the rapid desorption.

of the exothermal B and C peaks, it resulted in the complete disappearance of peak A. Finally, the top panel of Figure 2.11 shows the thermogram of a film vapor deposited at 175 K. In this case, the thermogram completely lacks any exothermal features. The endothermic upswing in the heat capacity at temperatures above 250 K, present in all three thermograms, is due to the onset of the rapid desorption.

The interpretation of Figure 2.11 is straight forward given the abundance of data available about the microstructure and phase transition in vapor deposited ASW films. When water vapor is deposited upon a cold substrate at temperatures less than 120 K, the resulting ASW film is highly strained and microporous. In scanning calorimetry experiments, such a film would produce a thermogram with a broad enthalpy relaxation peak. As the deposition temperature is increased, i.e., to temperatures around 140 K, the loss of the A peak from the film leads to its assignment as the enthalpy release during initial relaxation of microporous ASW, i.e., pore collapse[6]. When the deposition temperature is significantly higher (175 K), there is a complete lack of any exothermic peaks; therefore, the B and C peaks are assigned to the crystallization of the ASW film; specifically as crystallite nucleation and crystallite growth, respectively[6]. It is important to note here that a relaxed, low-crystalline ASW film can be grown by careful selection of the deposition temperature[6].

Figure 2.12 directly compares the heat capacities of ASW and crystalline ice films of nearly identical mass. The ASW film's deposition temperature was chosen so that peak A completely disappeared from the thermogram, while exothermic features B and C remained unchanged. The most important feature of the thermogram in Figure 2.12 is the

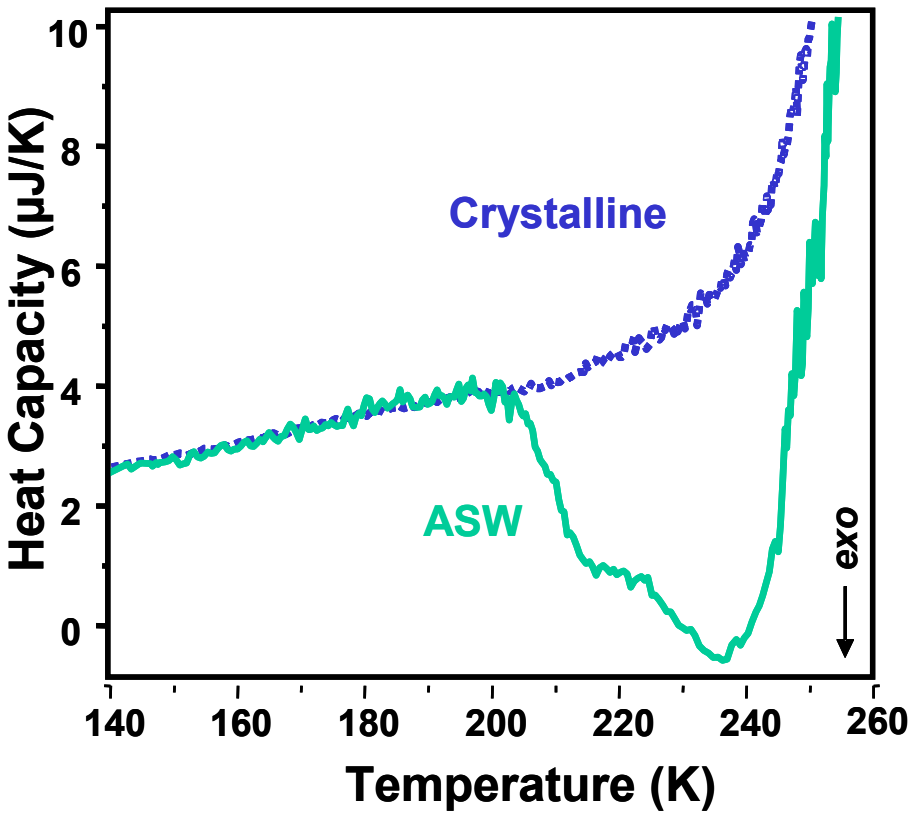

Figure 2.12. Heat capacities of ASW (solid line) and crystalline (dotted line) ice films of nearly identical mass (the accuracy of relative measurements of ice sample mass is better than 3%). The deposition temperature was 140 K and was chosen to ensure complete relaxation of strained ASW sample without its extensive crystallization. The most important feature of the thermogram is the near match in the heat capacities of the crystalline and the ASW samples up to the temperature of ASW crystallization.

near match in the heat capacities of the crystalline and the ASW samples up to the temperature of ASW crystallization.

2.3 Brief Summary and Conclusions

The experimental apparatus and the basic procedures described in this chapter represent the foundation of the Fast Scanning Calorimetry (FSC) technique. Although the following experiments detailed throughout this dissertation may seem more complex than the simple calorimetry experiments described here, they are all based on the same experimental sequence: vapor deposition of an ASW film, rapid heating, and complete vaporization at near constant temperatures. As shown in the next several chapters, FSC is a simple experimental approach which is able to accurately measure many fundamental properties of ASW that are far from being completely understood.

References

1. Sadtchenko, V.; Brindza, M.; Chonde, M.; Palmore, B.; Eom, R. *J. Chem. Phys.* **121**, 11980 (2004).
2. NIST Mass Spec Data Center, S. E. Stein, director, "Mass Spectra" in **NIST Chemistry WebBook, NIST Standard Reference Database Number 69**, Eds. P. J. Linstrom and W. G. Mallard, National Institute of Standards and Technology, Gaithersburg, MD, 20899, http://webbook.nist.gov, (retrieved April 13, 2009).
3. **Properties of Tungsten**, Midwest Tungsten Service, Willowbrook, IL, 60527, http://www.tungsten.com/mtstung.html, (retrieved April 29, 2009).
4. B. Palmore, Master's Thesis "Thermal Desorption Spectroscopy, Time of Flight Mass Spectrometry and Microcalorimetry Studies of Ice Vaporization", The George Washington University, 2005.
5. H. Lu, Doctoral Thesis "Studies of Polycrystalline Ice near Its Melting Point with Fast Thermal Desorption Spectroscopy: Vaporization Kinetics, Molecular Trasnport, Reactions, and Phase Transitions", The George Washington University, 2008.
6. For a review, see R. A. Baragiola, in *Water in Confining Geometries*, Springer Series in Cluster Physics, edited by V. Buch and J. P. Devlin (Springer-Verlag, Berlin, 2003), pp. 359–395.

Chapter 3: Fast Scanning Calorimetry Studies on the Enthalpy Relaxation Time of Vitreous Molecular Solids

3.1 Introduction

The previous chapter discussed how fast scanning calorimetry (FSC) can be used as an experimental approach to measure the properties of amorphous solid water (ASW). An initial study performed by Sadtchenko, et. al.[1] utilized this technique in order to gain insights into the properties of amorphous solid water (ASW) at temperatures in the "No Man's Land" region (160 K to 235 K). The essential data obtained in their experiments consisted of the glass transition temperature in rapidly (up to 10^5 K/s) heated films of vitreous CH_3COOH/ASW phase. According to the central assumption of the experimental approach, such a *dynamic glass transition* (i.e., an endothermic upswing in fast scanning calorimetry experiments) must be observed at a temperature, where the enthalpy relaxation time (τ_h) becomes numerically equal to the inverse of the heating rate. In other words, the dynamic glass transition must be observed when τ_h becomes comparable to the typical observation time of the experiments.

In order to test the aforementioned assumption of FSC, Sadtchenko, et. al. obtained an FSC thermogram of vitreous toluene. The thermogram, collected at a heating rate of $1.3 \cdot 10^5$ $K \cdot s^{-1}$, showed a glass transition at 135 ± 5 K. They concluded that the enthalpy relaxation time in vitreous toluene was $8 \cdot 10^{-6}$ seconds near 135 K. Taking into account the uncertainties in the temperature measurements during rapid heating of the toluene samples,

they claimed that this result was in excellent agreement with previously reported relaxation time data[2]. Although this preliminary measurement was in good agreement with the central assumption of FSC, it was not a systematic study. Therefore, in this chapter I demonstrate that the FSC technique is capable of providing correct (within an order of magnitude) estimates of the enthalpy relaxation time at a particular temperature for a *variety* of vitreous molecular solids. In addition to these experiments, I have also conducted *variable rate* studies of the dynamic T_g dependence on the scanning rate.

3.2 Enthalpy Relaxation Time of Vitreous Molecular Solids

Figure 3.1 shows thermograms of approximately one micrometer thick vitreous toluene films measured at three different heating rates: $1.2 \cdot 10^4$, $1.2 \cdot 10^5$, and, $4.1 \cdot 10^5$ K/s. The experimental setup used for these additional experiments was the same as those described in Chapter 2. The thicknesses of the toluene films were between 0.5 and 1.5 micrometers. Using the data from the thermogram, I determined the enthalpy relaxation times in toluene at temperatures of 129 ± 3 K, 133 ± 3 K, and 137 ± 3 K to be $8.3 \cdot 10^{-5}$, $8.3 \cdot 10^{-6}$, and, $2.4 \cdot 10^{-6}$ s, respectively.

Figure 3.2 compares the results of the relaxation time measurements in toluene with the FSC technique to those obtained using other methods[2]. Note that the graph used for this analysis was constructed from Figure 4 of Reference 2, which combines relaxation time data obtained via several techniques. As shown in Fig. 3.2, the enthalpy relaxation times inferred from my FSC experiments (open diamonds) are in excellent agreement with those

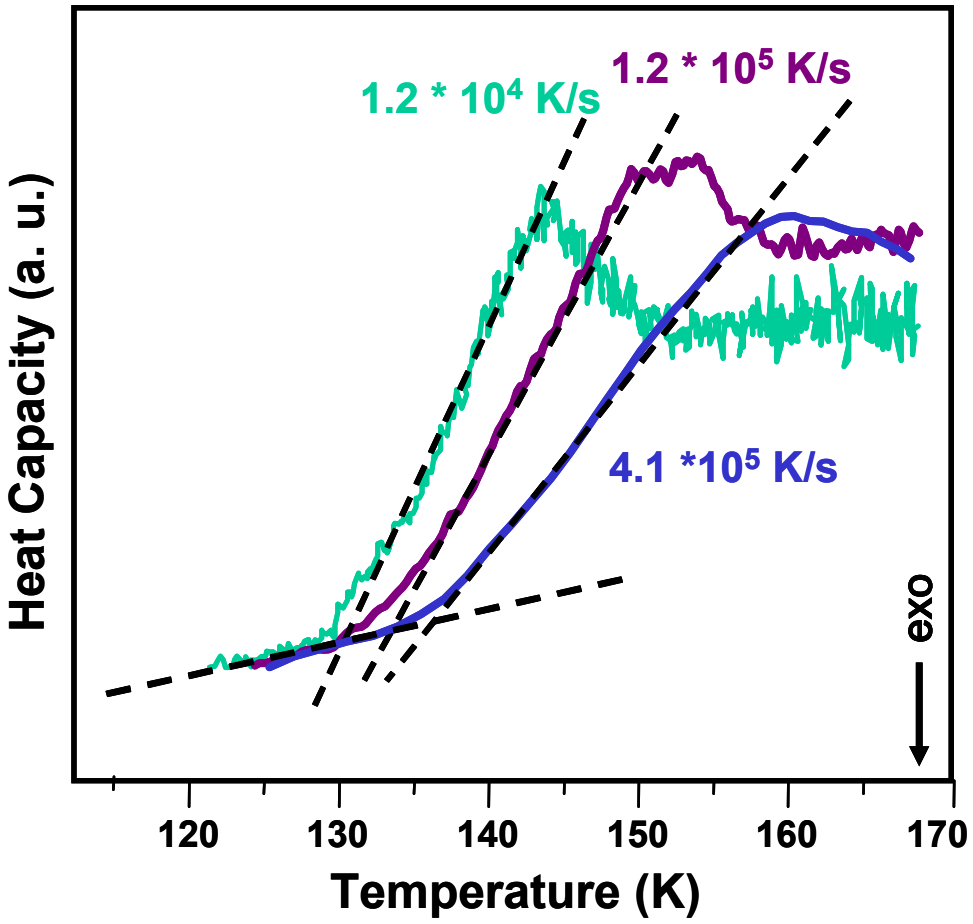

Figure 3.1. USC thermograms of toluene measured at three distinct rates. The thickness of toluene films was 1.0 ± 0.5 micrometers. The temperature of the onset of the glass transition was determined from the intersection of the dashed line. As shown in the figure, higher heating rates result in higher temperature of the glass transition.

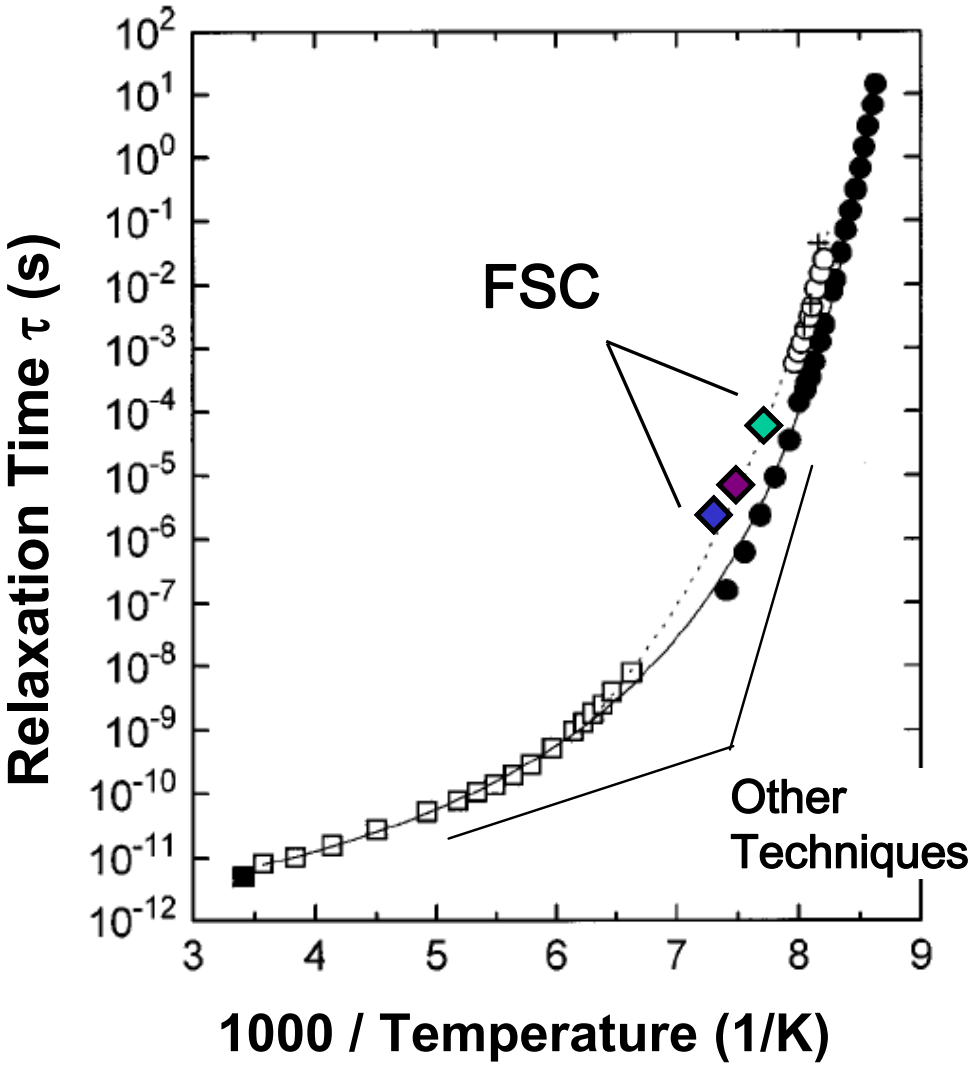

Figure 3.2. Relaxation data obtained by several techniques. Solid diamonds represent the relaxation times calculated as the inverse of the heating rates used for each of the toluene thermograms in Figure 3.1. The figure also shows the dielectric relaxation data (solid circles), deuteron spin-lattice relaxation data (open squares) as well as the relaxation data from microwave spectroscopy (solid squares). The dotted line describes the temperature dependence of τ_h obtained from diffusion and viscosity data, as well as that from deuteron spin alignment (open circles and crosses) data. Note that the figure was constructed from Figure 4 of Reference 2.

derived from viscosity, diffusion, deuteron spin alignment, and microwave spectroscopy studies (dotted line), and in good (within an order of magnitude) agreement with dielectric spectroscopy data.

In addition to my variable heating rate FSC studies of toluene, I also conducted measurements of the enthalpy relaxation time in other vitreous molecular solids for which dielectric relaxation data are available. Figure 3.3 compares FSC thermograms of 1.0 ± 0.5 micrometer thick films of 1-propanol, toluene, pentanol, decalin, and 2-ethyl-1-hexanol. The standard or *dynamic* glass transition temperatures, i.e., those corresponding to the relaxation time of approximately 10^2 seconds used in differential scanning calorimetry (DSC), and the heating rates of FSC scans are shown next to each thermogram. To ensure the formation of a pore-free, low enthalpy films, each vitreous solid was deposited on the surface of the filament at a temperature 10 – 20 degrees above its standard glass transition temperature. After deposition, the temperature of the sample was lowered to approximately 120 K and an FSC scan was initiated.

During the FSC experiments, each of the studied compounds undergoes a glass transition at a temperature significantly higher than that in conventional calorimetry scans (see Figure 3.3). Assuming that the enthalpy relaxation time at the onset of the glass transition is numerically equal to the inverse of the heating rate, I obtain a set of *dynamic* glass transition temperatures characteristic of FSC, which can be compared to those derived from dielectric spectroscopy studies.

The relaxation time data for vitreous molecular solids used in this study are shown in Figure 3.4[2-6]. From this data, the temperature at which the glass transition occurs can be

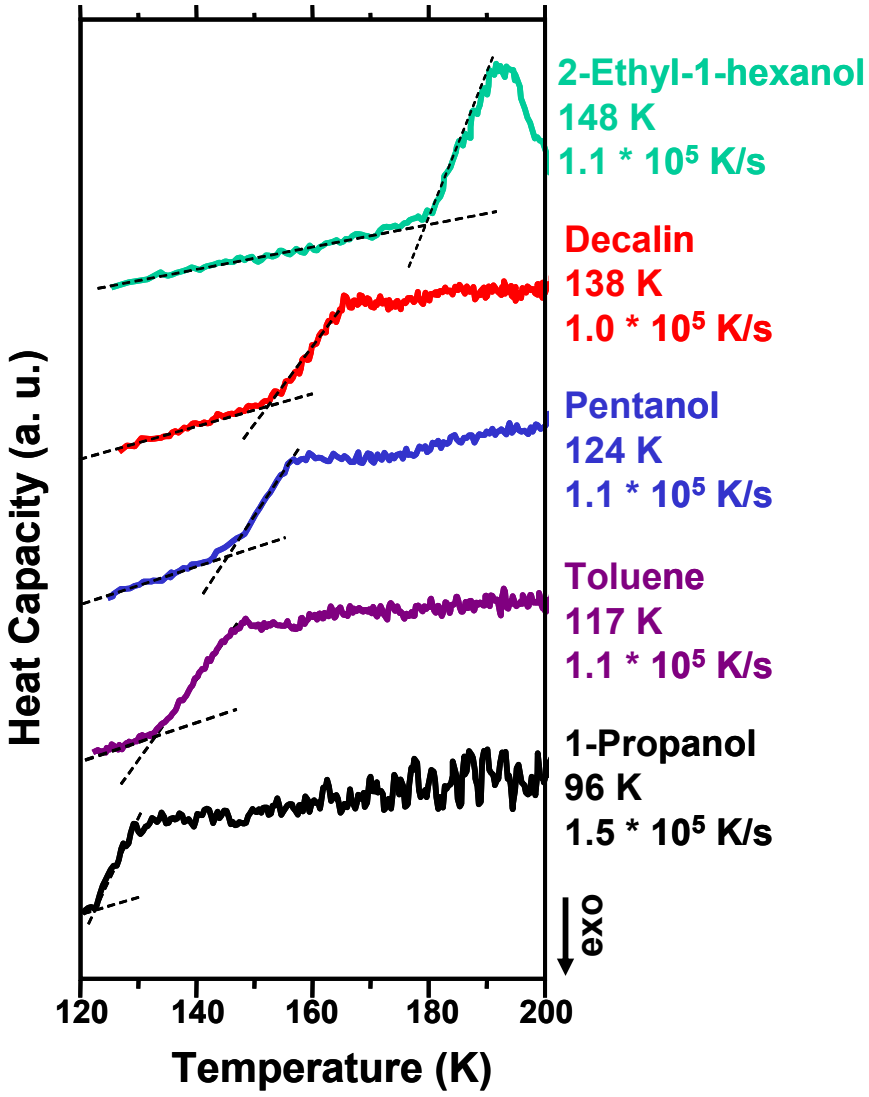

Figure 3.3. FSC thermograms of several organic glass-formers. Thin (0.5 – 1.5 μm) films were vapor-deposited on the surface of the tungsten filament at 10 – 20 degrees above their standard glass transition temperatures to ensure formation of a well-annealed, low enthalpy layers. After deposition, the temperature of the films was lowered to 120 K and a rapid calorimetry scan was initiated. The intersections of dotted lines designate the dynamic glass transition temperatures, i.e., the temperatures where the enthalpy relaxation time reaches the value numerically equal to the inverse of the heating rate. The standard glass transition temperatures, i.e., those obtained in conventional DSC experiments, are listed under the name of each compound along with the heating rate of the FSC scan.

determined by selecting the appropriate relaxation time. Since the relaxation time for our experimental approach is the inverse of the heating rate (i.e., 10^{-5} s/K), the temperature of the expected glass transition is determined as the point where each data line intersects with a relaxation time of 10^{-5} s. For example, using dielectric relaxation data for 2-ethyl-1-hexanol, the temperature where the relaxation time becomes 10^{-5} s is 178 ± 3 K[3]. A comparison of this value to the temperature of the dynamic glass transition observed in FSC experiments provides a criterion for the reliability of our technique.

Figure 3.5 shows the dynamic glass transition temperatures of various compounds measured by FSC and the corresponding temperature values derived from dielectric spectroscopy data[2-6]. The horizontal bars represent the temperature range where the dielectric relaxation time remains within an order of magnitude of the value numerically equal to the inverse of the heating rate of the FSC scan. As shown in the figure, with the exception of pentanol, the dynamic glass transition temperatures in FSC scans deviate from those derived from the dielectric spectroscopy data by less than a few degrees. Note that dielectric relaxation in pentanol is complex and may consist of up to four distinct temperature dependent processes (α_1, α_2, β and γ)[5]. If one assumes that α_2 and β dielectric relaxations are observed in scanning calorimetry experiments as a single relaxation process, where the temperature dependence is an average of the two dielectric processes, the agreement between FSC and dielectric spectroscopy is once again excellent. In short, FSC provides a reliable (within an order of magnitude) estimate of the enthalpy relaxation time at a particular temperature.

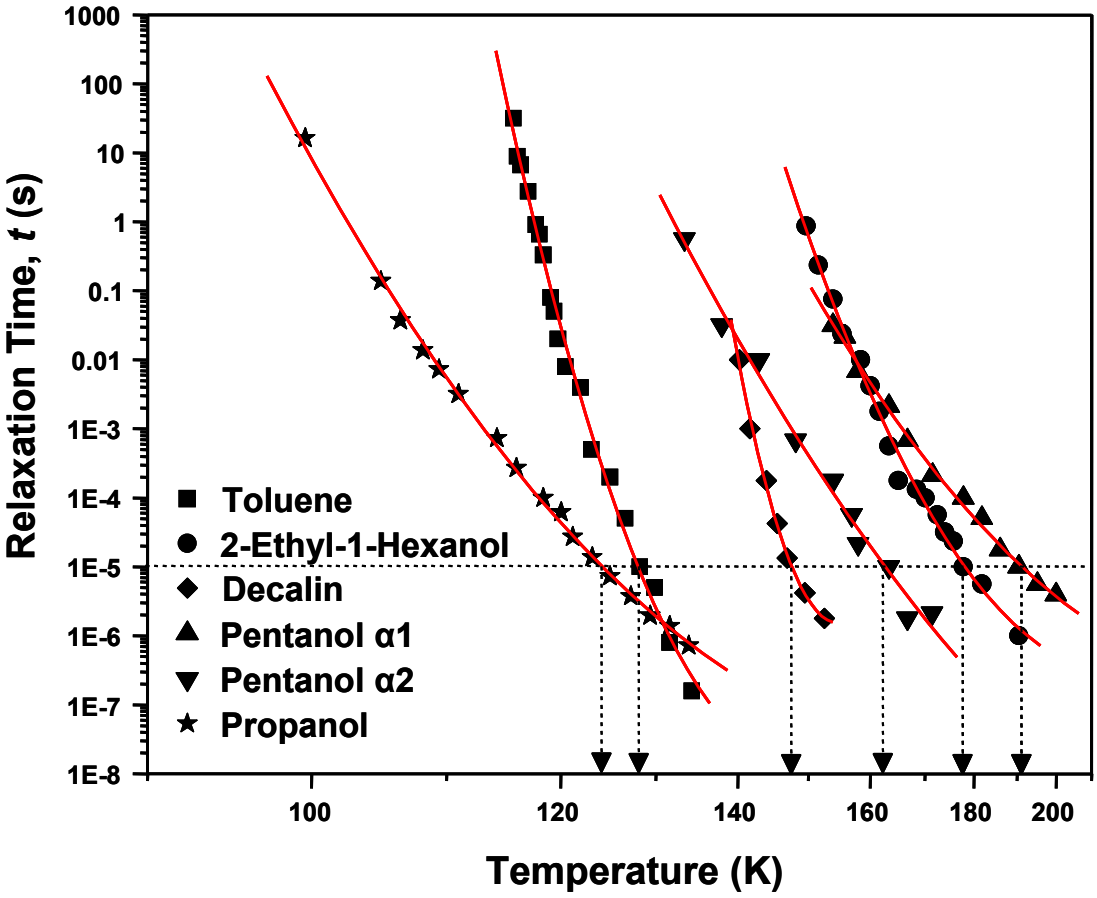

Figure 3.4. Relaxation time data for several organic glass-formers. The data shown in this figure was taken from a myriad of different dielectric spectroscopy studies (References 2 – 6). The dotted line originating at 10^{-5} s is the inverse of the typical heating rate (10^{5} K/s); therefore, the point at which the dotted line intersects with the data is the temperature of the expected glass transition using FSC.

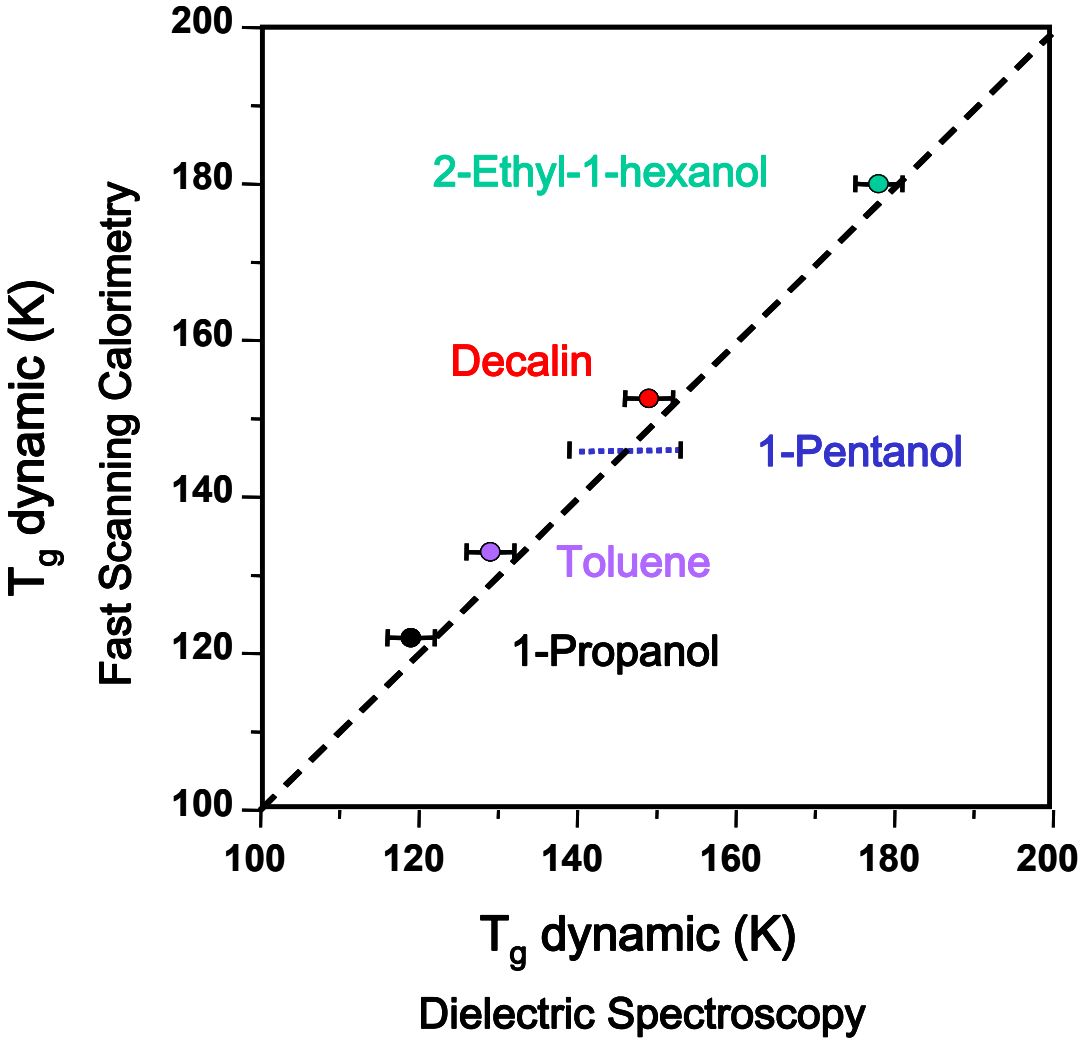

Figure 3.5. Correlation between the dynamic glass transition temperatures from FSC thermograms and those derived from the dielectric spectroscopy data. The points represent temperatures where the dielectric relaxation time is numerically equal to the inverse of the heating rate of the corresponding FSC scan. The horizontal bars mark the temperature range where the dielectric relaxation time is within an order of magnitude of the value numerically equal to the inverse of the heating rate of the corresponding FSC scan. With the exception of pentanol, the dynamic glass transition temperatures in FSC scans deviate from those derived from the dielectric spectroscopy data by less then five degrees.

3.3 Widths of Glass Endotherms

I would like to note that endotherm broadening in FSC scans is expected considering the thermal lags and gradients (refer to Chapter 2), which are undoubtedly present during rapid heating of vitreous molecular films of low thermal conductivity; however, it must be emphasized that the width of the glass endotherms in FSC scans is largely irrelevant to the discussion of the results because my estimates of the relaxation time at a particular temperature rely exclusively on detecting the *onset* of the glass transition in the FSC thermogram, and not on the endotherm's width. I must also note that any simple comparison of the width of an endotherm obtained at heating rates in excess of hundred thousand degrees per second with those obtained in standard DSC experiments is meaningless, unless the details of heat transfer in micrometer thick films are taken into account. Nevertheless, as Figure 3.5 demonstrates, the thermal lags and gradients do not prevent me from inferring the correct (within an order of magnitude) estimate of the enthalpy relaxation time. As I will explain later in this dissertation thesis (Chapter 4), such an experimental capability of the FSC technique is invaluable for studies of molecular kinetics in amorphous solid aqueous solutions.

3.4 Summary

By conducting a systematic study of the glass transitions of several physically distinct vitreous molecular solids, I demonstrate that the FSC technique is capable of providing a correct (within an order of magnitude) estimate of the relaxation time at a particular temperature. Using the relaxation time data obtained from dielectric spectroscopy, I was able to predict the temperature at which the glass transition should

occur during a fast scanning calorimetry experiment for each vitreous molecular solid studied. When these glass transition temperatures were compared to those obtained from the FSC thermograms of each compound, it was noted that the agreement between the two techniques only deviated by a few degrees. Thus, the central assumption of the FSC approach, i.e., the assumption that the inverse of the heating rate is equal to the relaxation time at the temperature where the glass transition is observed, is validated.

References and Notes

1. Chonde, M.; Brindza, M.; Sadtchenko, V. *J. Chem. Phys.* **125**, 094501 (2006).

2. Relaxation data for toluene: Döss, A.; Hinze, G.; Scheiner, B.; Hemberger, J.; Bohmer, R. *J. Chem. Phys*. **107**, 1740 (1997).

3. Relaxation data for 2-ethyl-1-hexanol: Wang, L. and Richert, R. *J. Phys. Chem. B*, **109**, 11091 (2005).

4. Relaxation data for decalin: Wang, L.; Velikov, V.; and Angell, C. A. *J. Chem. Phys.* **117**, 10184, (2002) and references therein.

5. Relaxation data for pentanol: Murthy, S. N. N. *Molecular Physics.*, **87(3)**, 691 (1996)

6. Relaxation data for propanol: Richert, R.; Angell, C. A. J. *Chem. Phys.* **108** (21), 9016, (1998), and references therein.

Chapter 4: Fast Scanning Calorimetry Studies of the Glass Transition in Doped Amorphous Solid Water: Evidence for the Existence of a Unique Vicinal Phase

4.1 Introduction

Despite decades of intense experimental and theoretical effort, development of a comprehensive picture of the relationships between various condensed phases of water (crystalline and amorphous solids, and supercooled liquid) remains an illusive goal. A vivid example of the lack of understanding in the field is the controversy surrounding a specific interpretation of a rather large set of experimental results, i.e., "the continuity conjecture"[1-3]. As shown in Figure 4.1 (dotted lines), within the framework of the continuity hypothesis, various dynamic properties of ASW such as self diffusivity, viscosity, and enthalpy relaxation time, can be related to those measured for liquid water at temperatures above 260 K via a simple Vogel-Fulcher-Tammann (VFT) equation ($T_{vogel} \approx$ 124K). In other words, water is assumed to be a *fragile* liquid over the entire temperature range from cryogenic to ambient. The cornerstone of such an interpretation of water properties is the original claim of the observation of a "calorimetric glass transition" at 136 K.

Experimental evidence, cited in support of the continuity conjecture, is substantial and includes traditional DSC experiments with pure and doped ASW[4], dielectric relaxation

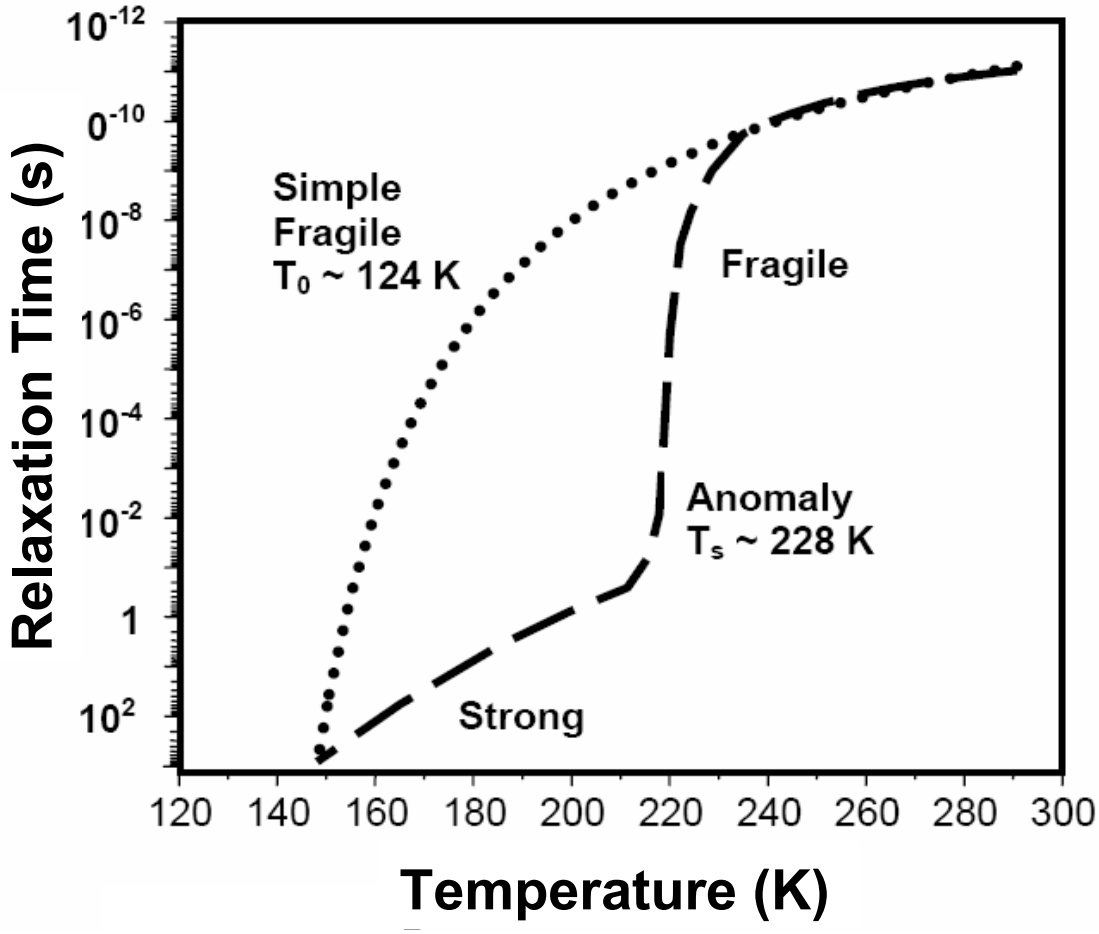

Figure 4.1. Two opposing interpretations of the state of water over the entire temperature range from cryogenic to ambient. The continuity conjecture (dotted line) follows the VFT equation where the Vogel temperature is 124 K. According to the continuity conjecture, water is assumed to be a fragile liquid at any temperature above 136 K. An alternate viewpoint (solid line) assumes a fragile-to-strong transition in the vicinity of 228 K (T_s).

time measurements of ASW in Poly (HEMA) matrix[5]; water self-diffusivity studies in ultrathin (< 30 nm) ASW films, investigations of ASW's mechanical properties[6]; and selected FTIR experiments[7]. While some of these experiments (e.g., "blunt indenter" studies of amorphous ice deformation[6]) were relatively simple, others relied on complex, state-of-the art experimental apparta and sophisticated sample preparation procedures. An example of the later approach is a recent electron spin resonance study of 4-hydroxy-TEMPO in amorphous ice obtained by flash freezing water samples in glass capillaries[8].

The continuity conjecture, along with the assignment of the glass transition to 136 K, described above has been the subject of considerable debate, primarily due to the fact that it excludes a possibility of anomalous variations in kinetic parameters (diffusivity, viscosity, relaxation time) near T_s[9]. In particular, Angell and coworkers consistently argued that water may undergo an anomalous transition from a fragile to a strong liquid in the vicinity of T_s (see Figure 4.1, dashed line), and that the postulated T_g of 136 K is incorrect and must be reassigned to a higher value[9-11]. Recent experimental results provided further basis for this alternative argument. For example, Mullins and coworkers demonstrated that abnormally high values of water self-diffusivity measured by Smith *et. al.* between 140 K and 160 K may be explained by rupturing of the ASW samples due to concurrent crystallization[12,13].

Motivated by current challenges in understanding of the fundamental properties of water, we have developed an experimental technique which makes it possible to conduct calorimetric studies of micrometer thick ASW films in the "No Man's Land" temperature range[14]. The technique, which we termed Fast Scanning Calorimetry (FSC), relies on the

heating of an ASW sample with rates in excess of 10^5 K·s^{-1} to circumvent crystallization of pure and doped ASW films at temperatures up to 200 K[15-17]. In addition to providing a way to measure the heat capacity of ASW and vitreous aqueous solutions during rapid heating between 120 and 200 K, FSC can also be used to infer quantitative information on molecular kinetics in ASW and other vitreous systems. Indeed, as we recently demonstrated[15,18], the onset of a glass transition observed in a FSC experiment occurs at a temperature where the enthalpy relaxation time becomes nearly equal to the characteristic experimental time (inverse of the heating rate). For example, an endothermic upswing with the onset at 175 K in FSC thermograms measured at a heating rate of 10^5 K·s^{-1} gives a value of $10^{-5\pm0.5}$ seconds for the enthalpy relaxation time of a vitreous solid at this particular temperature.

As shown in Figure 4.2, when heated with the rates on the order of 10^5 K/s, pure ASW does not undergo a glass transition at temperatures below 200 K, i.e., up to crystallization[15]. However, doping ASW with acetic acid brings up a strong glass transition at approximately 177 K. A cursory comparison of the data in the FSC thermogram with the relaxation time graph in Figure 4.2 shows that observation of a glass transition near 175 K is in accord with the continuity hypothesis (see Figure 4.3). The problem, however, is that the continuity conjecture seems to produce a correct prediction for T_g *only in the case of ASW heavily doped with* CH_3COOH. However, in the limit of low impurity concentration, ASW does not seem to undergo glass softening at temperatures up to 200 K[15].

Based on results of past FSC studies[15], we argued that assignment of the standard

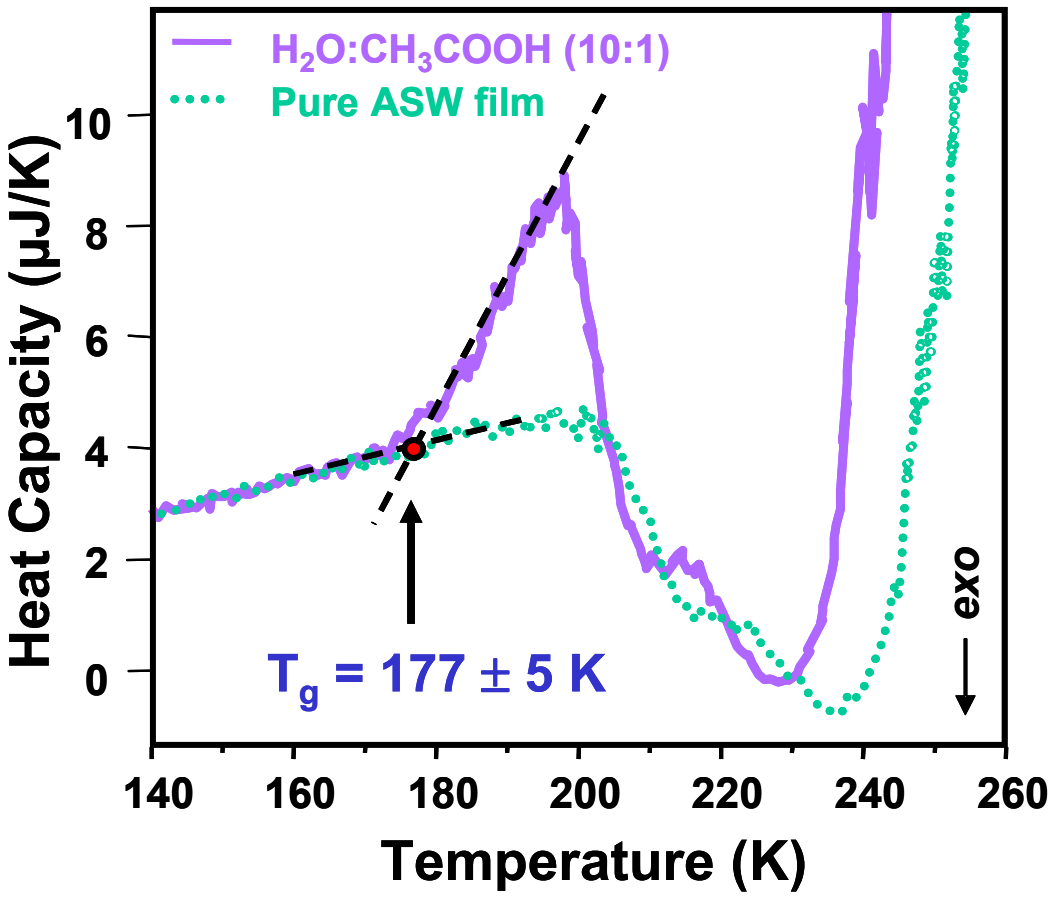

Figure 4.2. Fast scanning thermograms of pure (dotted) and doped (solid) ASW samples deposited under nearly identical conditions. Pure ASW does not undergo a glass transition at temperatures below 200 K, where it crystallizes. When doped with acetic acid, ASW shows a well pronounced glass transition at 177 ± 5 K.

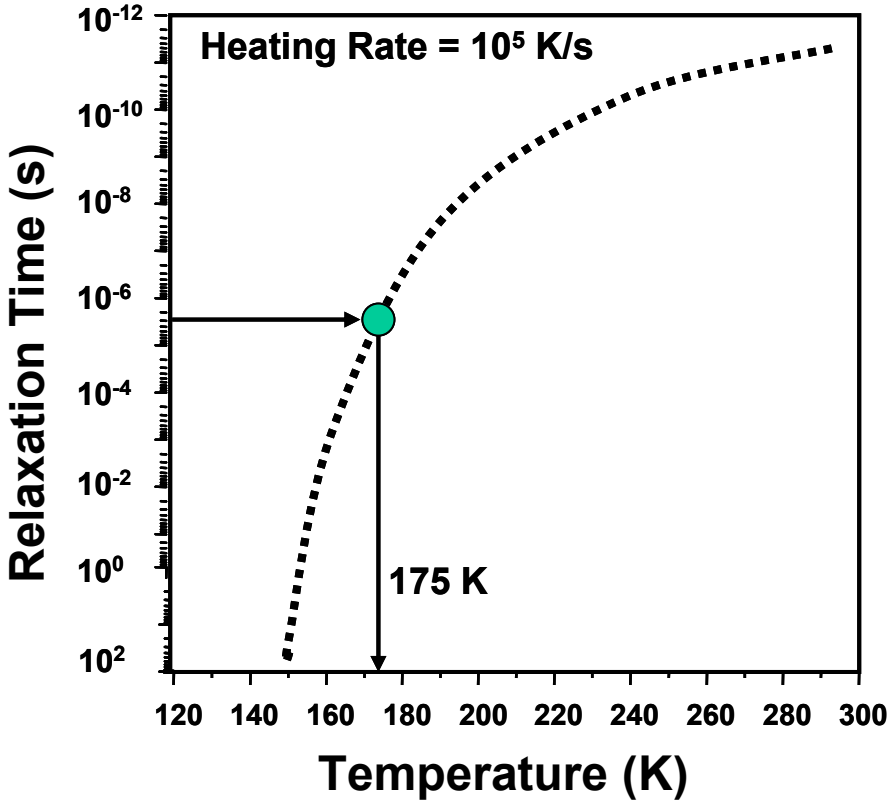

Figure 4.3. According to the continuity hypothesis (dotted line), a glass transition for pure water should be observed around 175 K when using a heating rate of 10^5 K/s. The grey circle represents the glass transition observed from the doped-ASW film from Figure 4.2. In this case, the continuity hypothesis is consistent, but only in the case of heavily doped ASW and, therefore, cannot be correct for pure ASW.

(as in "slow" DSC experiments) glass transition temperature to 136 K is incorrect in the case of pure ASW; and that pure water may exhibit an anomalous crossover from a fragile to a strong liquid. While a growing body of experimental evidence supports the existence of a strong-to-fragile transition near T_s[9], the experimental results contrast with such a view of supercooled water and cannot simply be discarded or ignored. It seems that many experiments, whose results agree with the continuity hypothesis, were conducted with vitreous water samples, which contained either impurities or large scale structural defects. To illustrate, Bhat et. al. concluded that the glass transition of *pure* ASW must occur at approximately 135 K using results from electron spin resonance studies of 4-hydroxy TEMPO in ASW[8]. Although the validity of these measurements can hardly be doubted, an important question arises about the nature of the aqueous system under scrutiny in this particular example. Because the spin probe ESR technique in Bhat's studies relied on the introduction of a probe species into ASW matrix, is it possible that the ESR spectrum variations with temperature are representative only of the molecular kinetics in ASW in the immediate vicinity of the guest molecules?

With the objective of clarifying the possible influence of guest species on molecular kinetics in ASW, we conducted careful FSC studies of pure ASW doped with acetic acid (CH_3COOH), pentanol ($C_5H_{11}OH$), ethanol (C_2H_5OH), and carbon tetrachloride (CCl_4) at levels below 0.04 (mole fraction). In the case of ASW doped with CH_3COOH, the variations in the FSC thermograms were studied for a range of impurity mole fractions (from 0.1 to 0.01). As we discuss in the following sections of this article, our recent FSC experiments provide a basis for a new outlook on the glass transition properties of dilute

amorphous solid mixtures of molecular impurities and water, and, thus facilitate reconciliation of conflicting experimental results on molecular kinetics in ASW.

4.2 Results and Discussion

4.2.1 FSC Thermograms of Doped ASW

In our previous FSC study[15], we conducted a brief investigation of the impact of impurities on molecular kinetics in ASW by doping an ASW sample with acetic acid. The mole fraction of acetic acid (X_{CH_3COOH}) in all of those experiments was approximately 0.1. Figure 4.4 shows selected results of FSC experiments where mole fraction of CH_3COOH was varied in a systematic way from 0.01 to 0.1. Each thermogram in Figure 4.4 corresponds to a doped ASW film of approximately 1 μm in thickness. The films were grown by a co-deposition of CH_3COOH and H_2O at 130 ± 2 K. The thermograms were measured at a heating rate of 10^5 K·s^{-1}. As we already mentioned, relative concentrations of CH_3COOH and H_2O in the film were verified by mass spectrometric analysis. The mole fractions of acetic acid are shown in Figure 4.4 next to each thermogram.

A cursory comparison of the thermograms of ASW films doped with distinct mole fractions of CH_3COOH shows that *first*, the temperature of the glass transition (T_g) during FSC scan is nearly independent of the concentration of CH_3COOH when X_{CH_3COOH} is below 0.04; *second*, when the mole fraction of acetic acid in ASW matrix is raised above 0.04, T_g begins to decrease with increasing CH_3COOH concentration: *third*, the magnitude of the endothermic upswing, *i.e.*, the excess heat capacity, ΔC_p, decreases almost linearly for dilute CH_3COOH/ASW films. The last conclusion is apparent from comparison of the

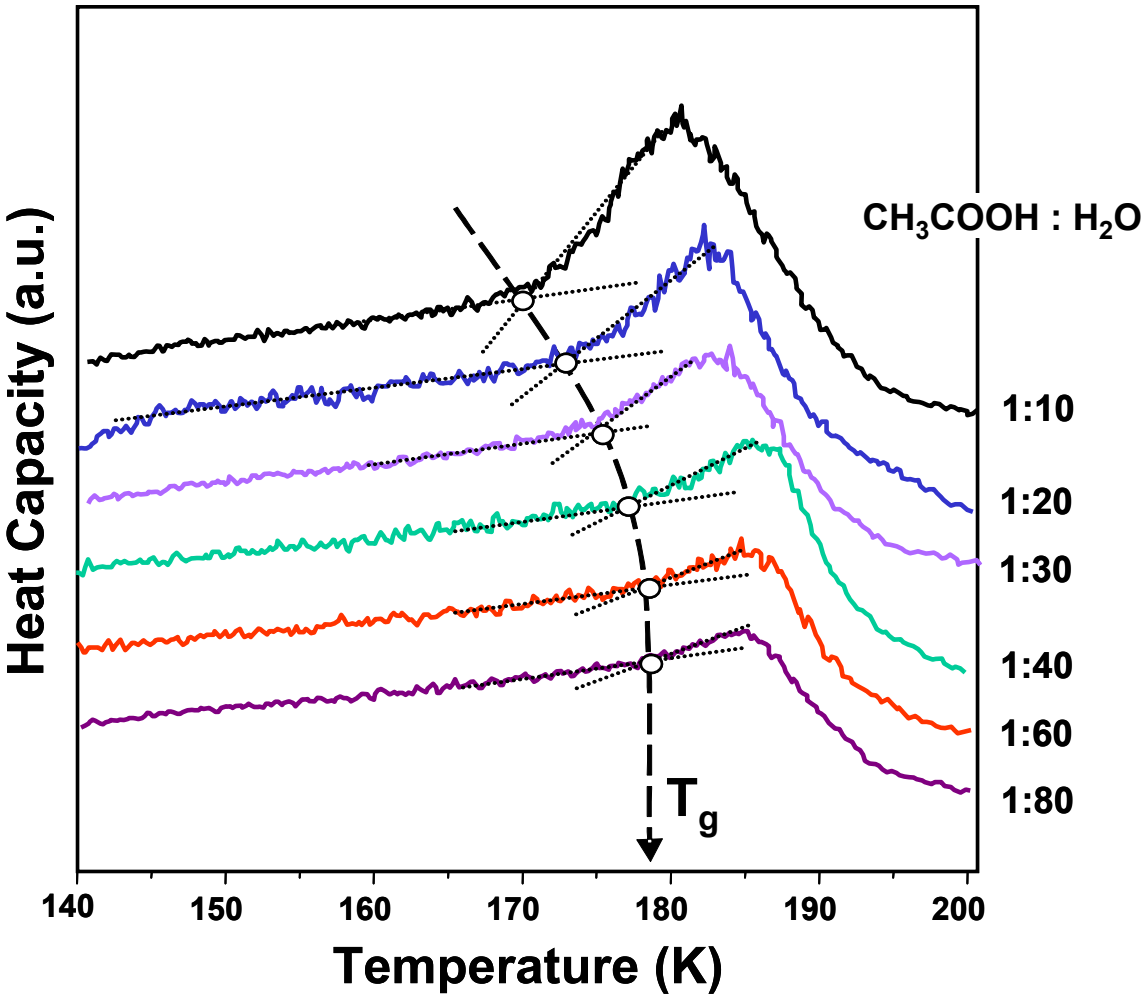

Figure 4.4. FSC thermograms of ASW doped with varying molar fractions of acetic acid. Each thermogram corresponds to a doped ASW film that is approximately 1 μm thick. The films were grown using co-deposition of water with acetic acid at 128 ± 2 K and measured at a heating rate of 10^5 K/s. A cursory comparison shows that T_g increases and the magnitude of the endothermic upswing decreases in the case of more dilute CH_3COOH/H_2O films.

endothermic upswing magnitude in the case of amorphous films with 1:40 and 1:80 ratios of CH_3COOH and H_2O. Finally, we note that at all mole fractions of CH_3COOH below 0.1, the crystallization of the doped ASW still occurs on the time scale and with enthalpy release similar to those during crystallization of pure ASW.

In order to further elucidate impact of impurities on molecular kinetics in ASW, we have conducted preliminary measurement of FSC thermograms of ASW doped with ethanol, pentanol, and carbon tetrachloride. The thickness of the doped ASW film was between one and two micrometers, and the molar fraction of dopants was near 0.04. The temperature of the filament during deposition of these doped ASW films was also 128 ± 2 K. The heating rate in experiments with different species were approximately $5 \cdot 10^4$ $K \cdot s^{-1}$. Figure 4.5 summarizes the results of these comparative studies.

As shown in Figure 4.5, FSC thermograms of ASW containing CH_3COOH, $C_5H_{11}OH$, C_2H_5OH, and CCl_4 are nearly identical at temperatures below 180 K. Although doping ASW with distinct chemical species may have an impact on kinetics of ASW crystallization, all of the thermograms show a well-pronounced glass transition near 177 ± 3 K. Small variations in T_g can be explained by variations in the heating rates of the films and by errors in the temperature measurements during rapid heating. Taking into account the differences in the structure of the guest species, the lack of distinctions in the glass transition temperatures of ASW films doped with various molecular impurities is quite remarkable. As we explain in the discussion section, the observed similarities in glass transition temperature of various weak ASW solutions justify a new model of molecular kinetics of impurity or defect-rich amorphous aqueous phase.

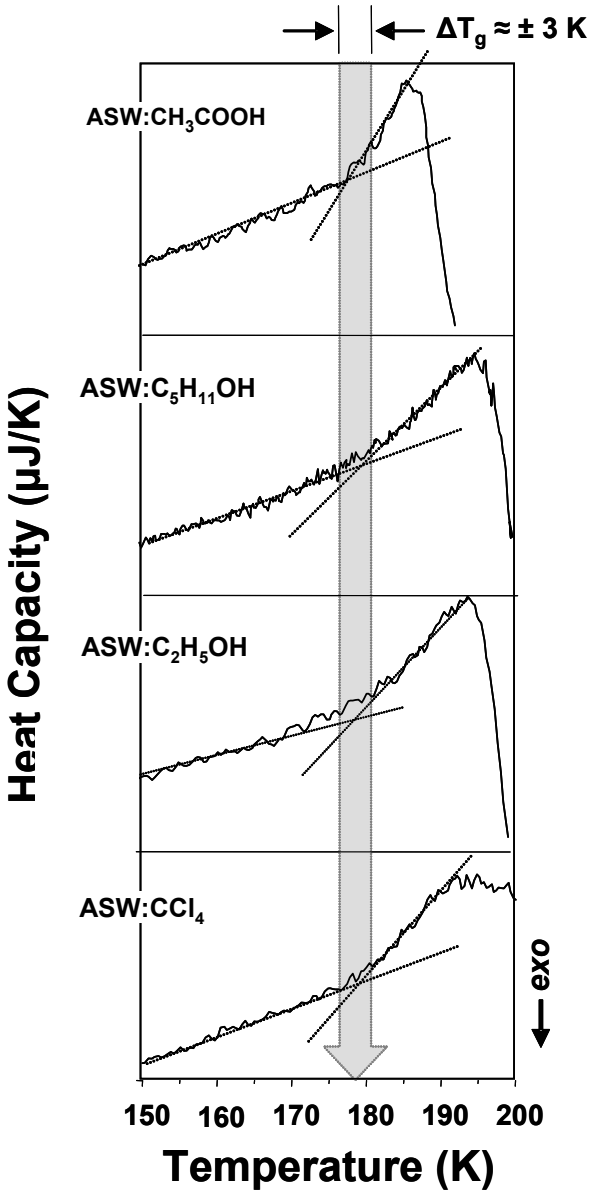

Figure 4.5. FSC thermograms of ASW doped with acetic acid, pentanol, ethanol, and carbon tetrachloride, respectively. Each thermogram corresponds to a doped ASW film that is 1-2 μm thick. The films were grown using a molar fraction of dopants near 0.04 for each impurity and measured at a heating rate of $5 \cdot 10^4$ K/s. Despite the use of such distinct chemical species as dopants, each thermogram shows a well pronounced glass transition at 177 ± 3 K.

The primary focus of the discussion of our results is the molecular kinetics in ASW doped with a variety of molecular species *at low concentrations*. Nevertheless, in order to facilitate comparison of our FSC investigations with previous dielectric spectroscopy studies of molecular kinetics in aqueous solutions, we have obtained FSC thermograms of pure acetic acid and pure pentanol. Representative results of these FSC experiments are summarized in Figures 4.6 and 4.7.

Figure 4.6 shows an FSC thermogram of a dilute solution of CH_3COOH (top panel), an FSC thermogram of a strong CH_3COOH solution (middle panel), and an FSC thermogram of nearly pure vitreous CH_3COOH (lower panel). The estimated concentrations are shown next to each thermogram. While we note that determination of a sample mass from heat capacity measurements is less reliable in the case of strong CH_3COOH solutions, we can still estimate the thickness of heavily doped ASW and pure CH_3COOH films from typical deposition times and rates of our calibrated vapor source [20]. In the case of strong aqueous CH_3COOH solutions shown in Figure 4.6 such an estimate results in values ranging between one and two micrometers for the resulting films. Due to uncertainty in the sample mass, the thermograms in Figure 4.6 were scaled to facilitate a qualitative comparison. Note that the heating rates in all thermograms shown in Figure 4.6 were approximately the same (10^5 $K \cdot s^{-1}$).

As shown in middle panel of Figure 4.6 increasing CH_3COOH mole fraction to approximately 0.3 leads to a significant (more then 10 degrees) *decrease* in the temperature of the glass endotherm. Furthermore, unlike that in the case of low CH_3COOH concentrations, crystallization of strong CH_3COOH/H_2O solution is suppressed. However,

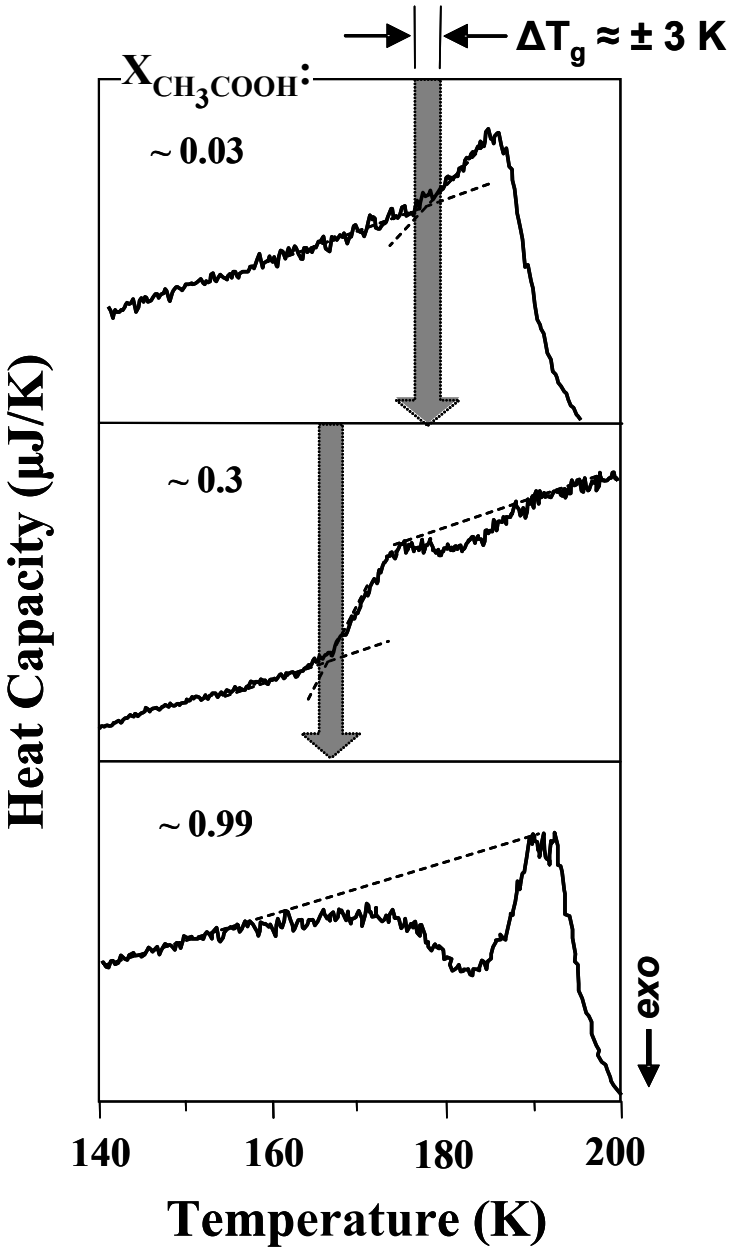

Figure.4.6. A FSC thermogram of a dilute solution of CH_3COOH (top panel), an FSC thermogram of a strong CH_3COOH solution (middle panel), and an FSC thermogram of nearly pure vitreous CH_3COOH (lower panel). The estimated concentrations are shown next to each thermogram.

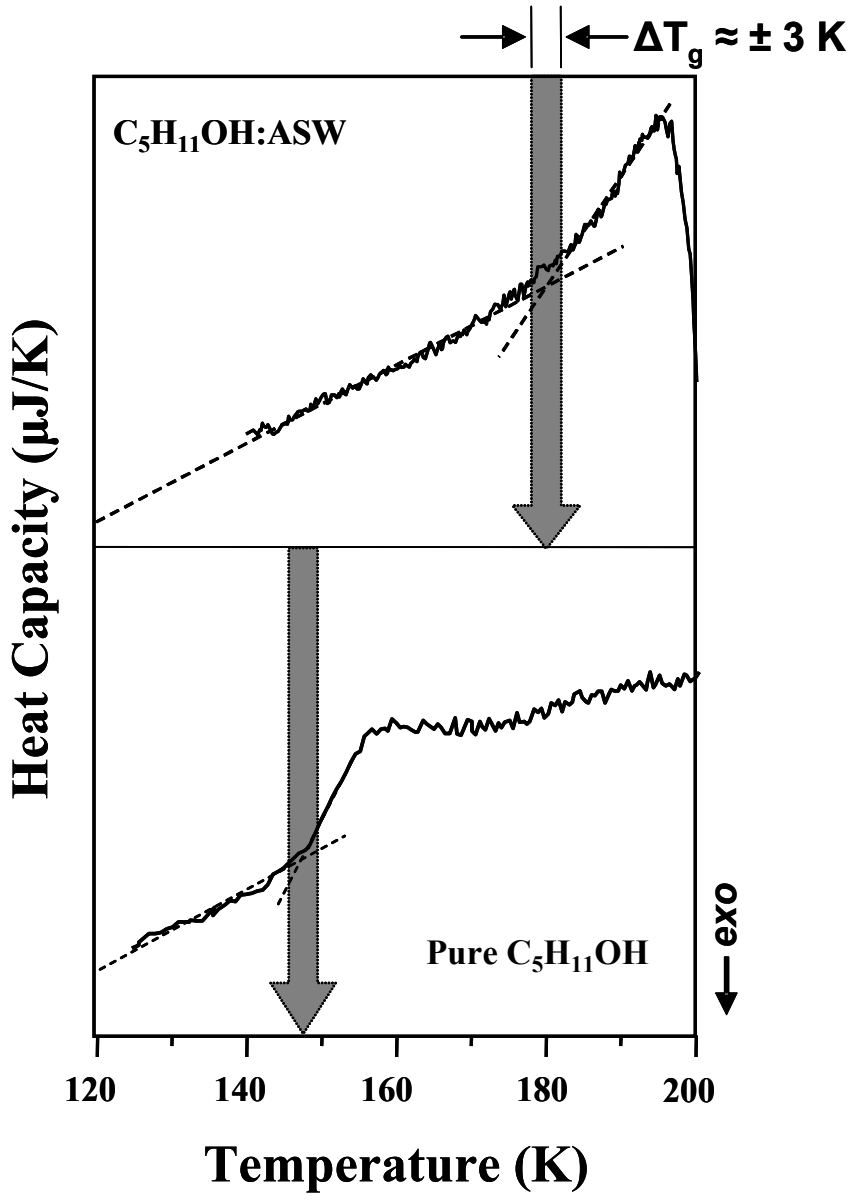

Figure 4.7. The FSC thermograms of dilute pentanol/ASW samples and pure pentanol films. As shown in figure, pure $C_5H_{11}OH$ films undergo a glass transitions at temperatures more than 30 degrees lower than $C_5H_{11}OH$ doped ASW films during rapid scans.

the crystallization of the pure acetic film is once again manifested in the FSC thermogram. Surprisingly, the thermograms of nearly pure CH_3COOH samples do not show an endothermic upswing characteristic of the glass transition. Although the lack of glass endotherms in pure CH_3COOH may seem to be in contrast with recent FSC studies of León-Gutierrez *et. al.*[22], we note that thickness of acetic films used in those experiments was on the order of 15 nm, *i.e.* [22], significantly lower than in our studies (in excess of a micrometer).

Although glass transition phenomena in vitreous CH_3COOH film of various dimensions is not completely understood at the present time, the FSC thermograms in Figure 4.6 still show that the endotherm observed in experiments with weak ASW solutions of acetic acid can not be explained by molecular kinetics in domains of pure or highly concentrated CH_3COOH. The existence of such domains is often invoked during analysis of the dielectric spectroscopy studies of a variety of binary aqueous solutions [23-29]. In the framework of the cooperative domain model [30], the endotherms observed in the FSC thermograms of weak ASW solutions must arise from the glass transition in regions of ASW film rich in impurities. Nevertheless, we emphasize that such an explanation seems unlikely due to observed differences in the thermograms of strong and dilute CH_3COOH/ASW mixtures. This conclusion is further strengthened by comparison of the FSC thermograms of pure pentanol films and dilute pentanol/ASW samples. As shown in Figure 4.7, pure $C_5H_{11}OH$ films undergo a glass transition at temperatures more then 30 degrees lower than $C_5H_{11}OH$ doped ASW films during rapid scans. In the next section of

this article we provide further arguments against a cooperative domain based interpretation of our FSC results.

4.2.2 Interpretation of the FSC Thermograms of Doped ASW from the Standpoint of the Cooperative Domain Theory

As we already mentioned, molecular kinetics in a variety of binary aqueous solutions have been studied in the past by broadband dielectric spectroscopy (BDS) [23-28]. The dielectric relaxation times were determined as functions of water content and temperature. The interpretation of BDS results is often based on a model, which assumed the existence of three types of microscopic cooperative domains (CD), i.e., CD which includes pure solute, CD which includes pure solvent, and CD which consists of both solute and solvent species. Because the CD model has provided a reasonable explanation for the BDS, we will first attempt to interpret the FSC thermograms using this approach.

In the framework of CD model[23-30], the thermograms of the dopant/ASW mixtures must be a sum of the thermograms of pure acetic acid, pure ASW, and the acetic acid/ASW domains. If the difference in heat capacities of the glassy and viscous H_2O in pure ASW domains is small, it can be argued that the main contribution to the glass endotherm in thermograms of CH_3COOH/ASW films must arise from either the pure solute or from the solute-rich ASW domains. Because, the size of these domains is proportional to the dopant concentration, and because the heat capacity is an extensive thermodynamic property, linear variation in the magnitude of the endothermic upswing upon a glass transition (ΔC_p) with dopant concentration is expected. Furthermore, the lack of variations in the glass transition temperature, *i.e.*, an effect similar to the one observed recently by Hayashi *et. al.*

in experiments with frozen water-glycerol solutions[23,27], may be rationalized by assuming that the CH_3COOH/ASW mixtures in our FSC phase-separate into pure (glassy) ASW and a strong (liquid) CH_3COOH-rich domains, where CH_3COOH content remains independent of temperature. In recent BDS experiments[23] by Hayashi *et. al.*, such a "critical" (invariant) concentration of glycerol was determined to be on the order of 40%.

While a CD model may still be used to rationalize our FSC thermograms of ASW doped with varying amounts of CH_3COOH, we would like to point out two serious inconsistencies in the scenario described in the previous paragraph.

1. The CD based interpretation described above is based on the implicit assumption that ASW/CH_3COOH mixtures in our studies phase-separate into pure ASW and dopant-rich ASW domains on the time scale of the FSC experiments. Furthermore, the dopant-rich ASW domains are required to have some "critical" (temperature invariant) concentration of the dopant species. While we do not question a possibility of phase separation of water rich homogeneous solutions of glycerol during gradual cooling in BDS studies[23,27], we emphasize that such a process is extremely unlikely in our FSC experiments where CH_3COOH/ASW films are prepared by co-deposition of homogeneous vapors on a substrate (filament) at temperatures near 130 K. Even assuming a high, liquid-like diffusivity of dopant and water molecules in ASW films (10^{-18} – 10^{-16} cm^2/s at 130 K)[31], diffusion is unlikely to result in aggregation of CH_3COOH into solute-rich domains due

to an extremely short characteristic transport scale (less than 3.5 angstroms) on the time scale of the film deposition (minutes). The phase separation of initially homogeneous CH_3COOH/ASW solution is also unlikely during rapid heating from 130 to 200 K due to a short time scale of fast calorimetry scans (fraction of a millisecond).

2. Formation of pure solute or solute-rich domains during deposition and/or during rapid heating of doped ASW films is also in contrast with the observed similarities in T_g measured in our FSC experiments for distinct guest species. If the glass endotherms for ASW films doped with acetic acid, ethanol, pentanol, and CCl_4 at levels below 0.04 (mole fraction) are due to glass transitions from pure solute or solute-rich domains, then it stands to reason that the glass transition temperatures must be different for distinct dopant species. Indeed, as shown in Figures 4.6 and 4.7, pure acetic acid and pure pentanol film solutions are characterized by dramatically different FSC thermograms. However, the observed glass transition endotherms of weak dopant/ASW solutions are virtually independent of the nature of guest species when the dopant concentrations are low (see Figure 4.5). In other words, the similarities in thermograms of weak solutions of various chemical species indicate that molecular dynamics in doped ASW are defined primarily by the solvent (H_2O) dynamics.

In summary, while providing a highly plausible explanation for the results of dielectric spectroscopy studies of strong binary solutions at temperatures above 130 K, the CD model based interpretation *fails* to provide a consistent explanation for the result of our FSC studies. This is not surprising due to the essential differences in the nature of the experiments in past BDS and in the current FSC experiments. Unlike numerous past BDS experiments with gradually cooled binary solutions, the FSC approach is characterized by a much greater degree of control over the structure of the vitreous sample due to the epitaxial deposition of doped ASW films via effusive molecular beams at cryogenic temperatures. In the following section of this article we provide an alternative explanation for the observed FSC results, which we termed the vicinal ASW hypothesis. This model not only explains the general features of the fast thermograms, but also makes it possible to reconcile seemingly contradictory results of the past studies of molecular kinetics in ASW.

4.2.3 Vicinal ASW Hypothesis

There are numerous experimental examples where the transport properties, reactivity, and structure of the condensed aqueous phase are dramatically altered by the vicinity of an interface. For instance, a liquid-like layer forms at the interface between ice and another solid at temperatures well below the normal melting point[32,33]. Furthermore, results of numerous studies of glass transition phenomena in confined systems such as thin films of microscopic pores may also be interpreted in terms of interfacial or vicinal effect on molecular dynamics in vitreous solids[34]. Taking into consideration the results of confinement on glass-formers as well as other interfacial effects in hydrogen bonded systems, we speculate that molecular kinetics in amorphous solid water in the immediate

vicinity of an impurity are fundamentally different from those of pure, bulk ASW. In particular, we hypothesize that ASW in a solvation shell around CH_3COOH undergoes a glass transition at temperatures significantly lower than that characteristic of the pure, bulk ASW. Although water in such viscous liquid shells may conform to a VFT dependence shown in Figure 4.1, ASW found in unperturbed regions of the doped films is essentially a strong glass which undergoes strong-to-fragile transition near T_s.

As illustrated in Figure 4.8, according to our conjecture, the FSC thermograms of doped films are comprised of contributions from the heat capacities of such vicinal ASW, which is a fragile liquid at temperature above 136 K, and unperturbed ASW, which is a strong glass at temperatures below 200 K. On a FSC thermogram, the unperturbed, bulk-like fraction of the doped ASW film has a heat capacity which is the same as the heat capacity of pure ASW (dashed lines). In other words, it lacks endothermic features characteristic of a glass transition. However, the vicinal fraction of the doped ASW film demonstrates a strong glass transition at 177 K (dotted lines). At any temperature, the observed heat capacity of the entire doped ASW sample is a linear combination of the heat capacities of the vicinal and bulk fractions with the contribution of each component proportional to their fractional volumes (solid lines).

The observed dependences of T_g and ΔC_{eff} (magnitude of the glass transition endotherm) on the concentration of CH_3COOH in doped ASW samples are in excellent agreement with the conjecture described above. As shown in Figure 4.8, a gradual increase in the concentration of impurities should lead to the proportional (linear) increase in the fraction of vicinal ASW as long as the concentration of impurities is sufficiently low so that

the solvation shells do not overlap. However, when the concentration becomes sufficiently high, the fraction of ASW film affected by impurities will approach its physically possible maximum, thus, resulting in a nonlinear dependence of volume of vicinal ASW on the impurity concentration.

At low dopant concentrations, i.e., when microscopic volumes of ASW film affected by interactions with impurity species do not overlap significantly, the change in the impurity concentration should not have any effect on T_g, as illustrated in Figure 4.8. In other words, when the average distance between impurity molecules is significantly greater than the effective radius of induced perturbation, the variations in the concentration of impurities must lead only to variations in the total volume of perturbed ASW and not in the character of the perturbation. Nevertheless, when the concentration of the impurities becomes sufficiently high so that the average distance between impurity molecules becomes significantly shorter than the effective radius of the perturbations induced in ASW by a single impurity molecule, the nature of perturbations is likely to change. Kinetic properties of the aqueous phase in such a strong solution may be altogether different from those in either vicinal or bulk ASW, which is emphasized by introducing "strongly perturbed" ASW in Figure 4.8.

The experimental data summarized in Figure 4.9, i.e., the observed dependences of ΔC_p, and T_g on the concentration of acetic acid, are in excellent agreement with the hypothesis. Indeed, in the limit of low concentrations, ΔC_p increases *linearly* with the concentration of CH_3COOH; however, it quickly saturates when the mole fraction of

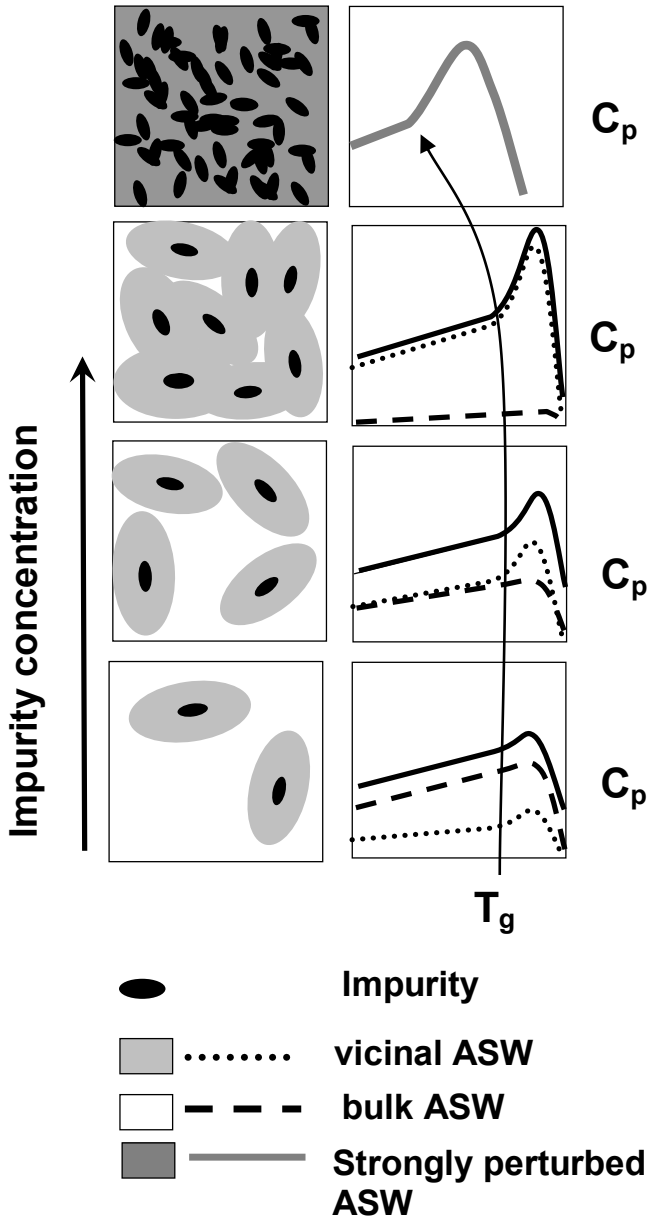

Figure 4.8. Illustration of the vicinal glass transition hypothesis. According to the hypothesis, FSC thermograms reflect a linear combination of the heat capacities from the fragile liquid which surrounds each dopant molecule (vicinal ASW – dotted line), and from the strong glass of the bulk (unperturbed ASW – dashed line). A gradual increase in the concentration of impurities leads to a linear increase in the fraction of vicinal ASW, so long as the solvation shells surrounding each molecular impurity do not overlap. This increase results in a linear increase in ΔC_P and a constant T_g. In the limit of high concentration of impurities, the solvation shells begin to overlap, resulting in "strongly perturbed" ASW (bold, solid line).

CH_3COOH exceeds 0.04. At the same time, the glass transition temperature begins to decrease from its maximum value near 178 K. Furthermore, referring to Figure 4.9, it is evident that significant changes in T_g and ΔC_p of doped ASW films occur at a molar ratio of CH_3COOH to H_2O approximately equal to 1:25. Assuming that the vicinal ASW conjecture described in the previous section is correct, there are approximately 25 molecules of water surrounding each CH_3COOH molecule at this concentration. *In other words, the local perturbations to the*

ASW matrix may extend to distances up to three water molecular diameters from the impurity.

4.2.4 Extrapolation of T_g for Pure ASW from Past Solution Studies

As we have already mentioned, standard DSC and dielectric spectroscopy experiments were conducted in the past with glassy mixtures of water and a variety of other species[26,35-38]. Variations in T_g with concentration of one of the solution components were sometimes used to infer the glass transition temperature of pure glassy water. While some of these studies relied on the Gordon-Taylor model[39] to extrapolate T_g values in the limit of extremely low guest species, others rejected its applicability in the case of glassy aqueous solutions[26,36,38]. Despite different approaches to the interpretation of the data, rather strong conclusions were often drawn about T_g values of pure vitreous water. For instance, based on the observed deviations of T_g of binary mixtures from Gordon-Tailor equation, Murthy *et. al.* once again asserted the validity of assignment of the glass-transition temperature to 136 K and argued that water is simply a fragile glass in the entire temperature range from cryogenic to near ambient[36].

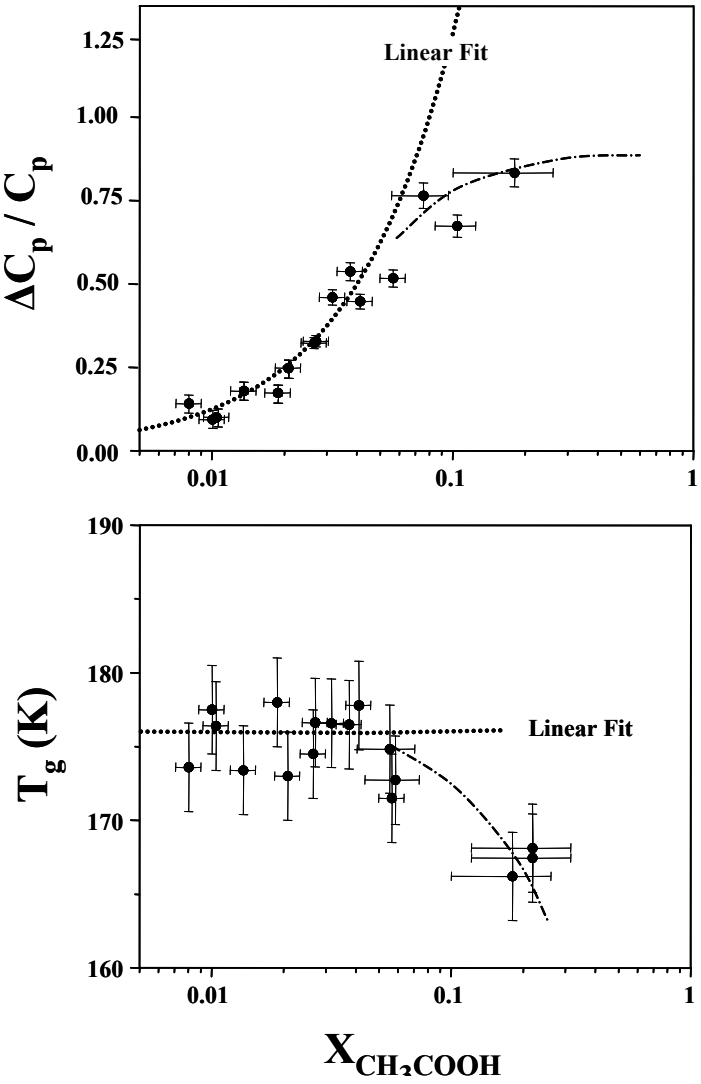

Figure 4.9. *Top panel:* The relative magnitude of the endothermic upswing ($\Delta C_P/C_p$) from doped ASW films as a function of molar fraction of acetic acid to water. In the limit of low concentrations, ΔC_P is directly proportional to the mole fraction of CH_3COOH. As the molar fraction increases beyond 0.04, the relative endothermic upswing approaches its maximum value of approximately 0.9. *Lower panel:* The glass transition temperature of doped ASW films as a function of molar fraction of acetic acid to water. As the concentration of CH_3COOH is reduced from 0.18 to 0.04, T_g increases from 167 ± 2 K to 177 ± 2 K. In the limit of low concentrations, i.e., less than 0.04 mole fraction, the glass transition temperature approaches its maximum value of 177 ± 3 K.

Taking into account the vicinal ASW hypothesis proposed in this article, the failure of the Gordon-Taylor relationship in the case of vitreous aqueous mixtures is well understood. The Gordon-Taylor model assumes that doped vitreous water is a two component mixture, *i.e.*, it does *not* take into consideration possible vicinal or interfacial effects. Nevertheless, our FSC experiments show that introducing guest species into the ASW matrix may lead to the formation of a unique viscous phase near the impurity. In short, a possible decomposition of ASW into "vicinal" and "bulk" components upon the addition of guest species makes any inference of T_g of pure water from the doped ASW data meaningless.

The likely presence of structurally distinct vicinal water in past calorimetric studies provides a ready explanation for the presence of weak endothermic features in some of the past DSC experiments with what was assumed to be "pure" vitreous water samples. Indeed, it follows from our FSC experiments that the relative change in the heat capacity of vicinal ASW upon the glass transition may be as high as 50%. Thus, an endotherm with a relative magnitude on the order of a few percent may occur as a result of glass transitions in solvation shells of impurities and/or near structural mesoscopic defects (pores and ruptures) if the volume fraction occupied by such effects is greater than 10^{-3}. In experiments where water samples are vitrified by flash-freezing of microscopic drops in the presence of secondary gases, such abundance of structural defects and impurities seems to be entirely possible.

4.3 Summary and Afterword

Fast scanning calorimetry experiments described in this article indicate that two distinct forms of water may exist in aqueous solutions at temperatures below 200 K. According to interpretation of FSC thermograms of ASW doped with acetic acid and other molecular impurities, introduction of guest species into the ASW matrix results in a perturbation of the hydrogen bond network *in the vicinity* of a guest molecule. Although the exact nature of these perturbations is not clear, their impact on the molecular kinetics consists of a significant *decrease* in the enthalpy relaxation time of ASW at a particular temperature. In other words, a guest molecule in the ASW matrix may be enveloped in viscous liquid (vicinal) water at temperatures as low as 136 K, while unperturbed ASW may remain in its glassy form at temperatures up to 228 K. According to our results, such a viscous shell contains approximately 25 H_2O molecules in the case of CH_3COOH.

The vicinal ASW conjecture described in this article has the potential to reconcile seemingly conflicting findings from a range of past studies. We argue that the past experimental results on molecular kinetics in vitreous water must be carefully re-examined while taking into account possible vicinal effects. Although such analysis may render some of these inapplicable in the case of pure bulk water, we emphasize that the results of experiments where vicinal water may come into play are of great interest from both fundamental and applied viewpoints.

References

1. Johari, G. P.; Fleissner, G.; Hallbrucker, A.; Mayer, E. *J. Phys. Chem.* **1994**, *98*, 4719.
2. Speedy, R. J.; Debenedetti, P. G.; Smith, R. S.; Huang, C.; Kay, B. D. *J. Chem. Phys.* **1996**, *105*, 240.
3. Sastry, S.; Debenedetti, P. G.; Sciortino, F.; Stanley, H. E. *Phys. Rev. E* **1996**, *53*, 6144.
4. Hallbrucker, A.; Mayer, E.; Johari, G. P. *J. Phys. Chem.* **1989**, *93*, 4986.
5. Johari, G. P. *J. Chem. Phys.* **1996**, *105*, 7079.
6. Johari, G. P. *J. Phys. Chem. B* **1998**, *102*, 4711.
7. Drobyshev, A.; Aldiyarov, A.; Zhumagaliuly, D.; Kurnosov, V.; Tokmoldin, N. *Low Temp. Phys.* **2007**, *33*, 355.
8. Bhat, S. N.; Sharma, A.; Bhat, S. V. *Phys. Rev. Lett.* **2005**, *95*, 4.
9. Angell, C. A. *Science* **2008**, *319*, 582.
10. Angell, C. A. *Annu. Rev. Phys. Chem.* **2004**, *55*, 559.
11. Giovambattista, N.; Angell, C. A.; Sciortino, F.; Stanley, H. E. *Phys. Rev. Lett.* **2004**, *93*, 4.
12. McClure, S. M.; Barlow, E. T.; Akin, M. C.; Safarik, D. J.; Truskett, T. M.; Mullins, C. B. *J. Phys. Chem. B* **2006**, *110*, 17987.
13. McClure, S. M.; Safarik, D. J.; Truskett, T. M.; Mullins, C. B. *J. Phys. Chem. B* **2006**, *110*, 11033.
14. Mishima, O.; Stanley, H. E. *Nature* **1998**, *396*, 329.
15. Chonde, M.; Brindza, M.; Sadtchenko, V. *J. Chem. Phys.* **2006**, *125*, 094501.

16. Sadtchenko, V. Fast Thermal Desorption Spectroscopy and Ultrafast Microcalorimetry: New Tools to Uncover Mysteries of Ice. In *Physics and Chemistry of Ice*; *Royal Society of Chemistry*: *Cambridge, UK*, 2007.

17. Sadtchenko, V.; Brindza, M.; Chonde, M.; Palmore, B.; Eom, R. *J. Chem. Phys.* **2004**, *121*, 11980.

18. Sadtchenko, V.; Lu, H. P.; McCartney, S. *J. Chem. Phys.* **2007**, *127*, 2.

19. Lu, H.; McCartney, S. A.; Sadtchenko, V. *J. Chem. Phys.* **2007**, *127*, 13.

20. Lu, H. P.; McCartney, S. A.; Chonde, M.; Smyla, D.; Sadtchenko, V. *J. Chem. Phys.* **2006**, *125*, 11.

21. Sadtchenko, V.; Ewing, G. E. *Can. J. Phys.* **2003**, *81*, 333.

22. Leon-Gutierrez, E.; Garcia, G.; Lopeandia, A. F.; Fraxedas, J.; Clavaguera-Mora, M. T.; Rodriguez-Viejo, J. *J. Chem. Phys.* **2008**, *129*, 4.

23. Hayashi, Y.; Puzenko, A.; Balin, I.; Ryabov, Y. E.; Feldman, Y. *J. Phys. Chem. B* **2005**, *109*, 9174.

24. Hayashi, Y.; Puzenko, A.; Feldman, Y. "Slow and fast dynamics in glycerol-water mixtures", 2006.

25. Hayashi, Y.; Puzenko, A.; Feldman, Y. *J. Phys. Chem. B* **2005**, *109*, 16979.

26. Cerveny, S.; Schwartz, G. A.; Alegria, A.; Bergman, R.; Swenson, J. *J. Chem. Phys.* **2006**, *124*, 9.

27. Puzenko, A.; Hayashi, Y.; Ryabov, Y. E.; Balin, I.; Feldman, Y.; Kaatze, U.; Behrends, R. *J. Phys. Chem. B* **2005**, *109*, 6031.

28. Sudo, S.; Shinyashiki, N.; Kitsuki, Y.; Yagihara, S. *J. Phys. Chem. A* **2002**, *106*, 458.

29. Shinyashiki, N.; Sudo, S.; Yagihara, S.; Spanoudaki, A.; Kyritsis, A.; Pissis, P. "Relaxation processes of water in the liquid to glassy states of water mixtures studied by broadband dielectric spectroscopy", 2007.
30. Matsuoka, S. *J. Res. Natl. Inst. Stand. Technol.* **1997**, *102*, 213.
31. Smith, R. S.; Dohnalek, Z.; Kimmel, G. A.; Stevenson, K. P.; Kay, B. D. *Chem. Phys.* **2000**, *258*, 291.
32. Dash, J. G.; Rempel, A. W.; Wettlaufer, J. S. *Rev. Mod. Phys.* **2006**, *78*, 695.
33. Li, Y.; Somorjai, G. A. *J. Phys. Chem. C* **2007**, *111*, 9631.
34. McKenna, G. B. *Eur. Phys. J.-Spec. Top.* **2007**, *141*, 291.
35. Murthy, S. S. N. *Cryobiology* **1998**, *36*, 84.
36. Murthy, S. S. N.; Singh, G. *Thermochim. Acta* **2008**, *469*, 116.
37. Rasmussen, D. H.; MacKenzie, A. P. *J. Phys. Chem.* **1971**, *75*, 967.
38. Cerveny, S.; Schwartz, G. A.; Bergman, R.; Swenson, J. *Phys. Rev. Lett.* **2004**, *93*, 4.
39. Gordon, J. M.; Rouse, G. B.; Gibbs, J. H.; Risen, J. W. M. *The Journal of Chemical Physics* **1977**, *66*, 4971.

Chapter 5: Insights into the Physical Nature of Vicinal Amorphous Solid Water from Variable Rate Fast Scanning Calorimetry

5.1 Introduction

In the preceding chapter of this thesis, I reported the results of fast scanning calorimetry (FSC) experiments which indicate that two distinct forms of water may exist in aqueous solutions at temperatures below 200 K, i.e., bulk and vicinal ASW phases. As I speculated in the discussion, the vicinal ASW must be characterized by a significant *decrease* in the enthalpy relaxation time at a particular temperature. In other words, a guest molecule in the ASW matrix may be enveloped in viscous liquid (vicinal) water at temperatures as low as 136 K, while unperturbed ASW may remain in its glassy (bulk) form at temperatures up to 228 K.

While the FSC thermograms reported in Chapter 4 are generally consistent with the vicinal ASW conjecture, I note that they were all measured at heating rates near 10^5 K/s. At a constant concentration of impurities, such "fixed" heating rate measurements allow only an estimate of the relaxation time at a single temperature value, i.e., at the temperature where the endothermic upswing in heat capacity of doped ASW appears in FSC thermograms measured at the particular "fixed" heating rate. The enthalpy relaxation time, however, is of course not a "fixed" parameter, but a strong function of temperature[1-3]. Thus, a systematic FSC study of the variations in glass transition temperature of doped ASW samples with the heating rate have a potential to strengthen and validate the central conclusions of Chapter 4 by demonstrating that water molecular kinetics in the vicinity of

guest species are indeed faster not only near 175 K, but also at other temperatures. In an ideal case, such variable rate FSC studies of doped ASW must be conducted for ASW films doped with a distinct amount of impurities. For instance, it would be desirable to conduct variable rate FSC measurements of CH_3COOH-doped ASW for "fixed" mole fractions of acetic acid ranging from 0.25 down to 0.01 (the range of CH_3COOH concentrations in "fixed" rate FSC studies described in Chapter 4). Unfortunately, the small magnitudes of the glass transition endotherms characteristic of ASW doped with small amounts of impurities limit the lower range of heating rates for such studies. While I am confident that further improvement in the sensitivity of the FSC technique will allow variable rate measurements of ASW doped at levels below 0.01 (mole fraction) to become possible, I used a rather high mole fraction of 0.1 of CH_3COOH to ensure a straightforward detection of the glass endotherms in FSC thermograms measured at heating rates near 10^3 K/s for the present study. As I explain in detail in the following sections of this chapter, the dependence of enthalpy relaxation time on the temperature determined in variable rate FSC studies of ASW containing 0.1 mole fraction of CH_3COOH can still be used to infer significant insights into the physical properties of hypothesized vicinal ASW despite the relatively high concentration of dopants.

5.2 Experimental Arrangement and Results

The experimental arrangement employed for variable rate FSC studies described in this chapter was essentially the same as that in Chapter 4. A single filament calorimeter was used for variable rate FSC studies. The data acquisition and vapor source were again

identical to those used in all past FTDS-FSC experiments. With the exception of introducing variations in heating rate, all of the essential procedures remained the same.

As illustrated in Figure 5.1, changes in the heating rate were accomplished by varying the biasing voltage across the single filament calorimeter from 2.0 to 9.0 volts. As shown in the figure, such an adjustment in the biasing voltage resulted in a two orders of magnitude change in the scanning rate of FSC experiments near the characteristic temperature of glass transition in CH_3COOH-doped ASW films. The heating rates were determined by calculating the first time derivative of the data summarized in Figure 5.1. Although the heating rates were not constant throughout the duration of a FSC scan, i.e., typically decreased by a factor of 2 from the onset of heating until the film crystallization, I emphasize that the heating rates immediately prior to the observed glass transition are important for the analysis of the enthalpy relaxation time dependence on temperature. Indeed, as I determined in preliminary experiments with a range of vitreous solids, only the heating rate at the onset of the endothermic upswing results in correct estimates of the enthalpy relaxation time using the Equation 5.1

$$\tau_h(T_g) = \frac{1K}{Q(T_g)} \tag{5.1}$$

where $Q(T_g)$ is the heating rate near the dynamic glass transition temperature.

The thickness of the doped ASW films was approximately two micrometers in experiments conducted at heating rates below 10^5 K/s. Such a thickness made it possible to improve the signal to noise ratio in FSC thermograms measured at low (below 10^4 K/s) heating rates while still ensuring the absence of significant thermal lags in rapidly heated

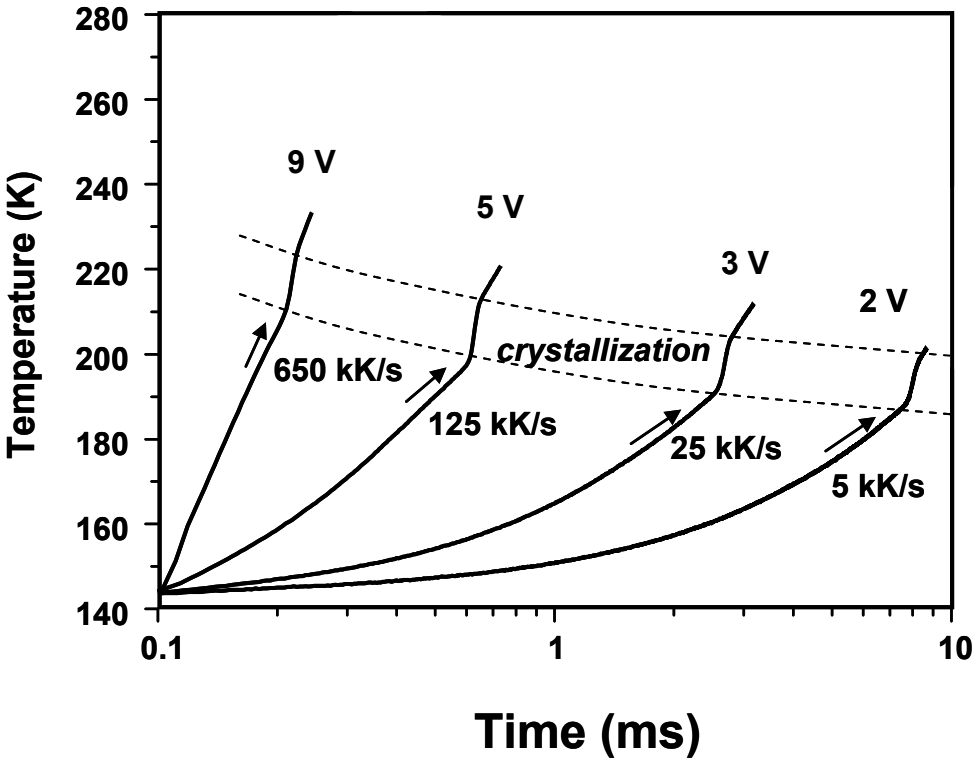

Figure 5.1. Heating curves of a ~2 μm ASW films from variable rate FSC experiments. By systematically changing the biasing voltage from 2V to 9V across the filament, the heating rates were varied from 5 kK/s to 650 kK/s; thereby, varying the onset and duration of crystallization of the ASW film.

films. As I already mentioned, the thickness of any film in an FSC experiment was chosen so that a typical thermal equilibration time would not exceed the characteristic experimental time (1K/Q). In order to satisfy this condition, the thickness of the ASW film was reduced to approximately one micrometer in the case of heating rates approaching 10^6 K/s.

5.3 Variable Rate FSC Thermograms of ASW Doped with Acetic Acid

Past FSC studies have shown that in the case of microscopic vitreous samples, the low heating rates present a challenge for sure detection of an endothermic glass transition in doped ASW samples. Low sensitivity of FSC measurements conducted with heating rates below 10^4 K/s is primarily due to electrical interference during measurements of low currents through the filament, which result in low signal to noise ratios in FSC thermograms of even relatively thick vitreous films. Further complications may arise from the temperature dependence of the endothermic upswing magnitude, i.e., the heat capacity difference (ΔC_p) between glassy and liquid states of a non-crystalline sample. For instance, it has been speculated that ΔC_p (glassy-liquid) of pure ASW may gradually decrease to extremely low values as the temperature approaches 137 K^4.

Taking into account the challenges involved in the detection of glass transition endotherms in low heating rate FSC studies, I conducted a series of experiments at the low heating rate of approximately $5 \cdot 10^3$ K/s. The current and voltage data from these experiments were averaged together in order to improve signal-to-noise ratio of the FSC thermogram. Figure 5.2 illustrates the result of this averaging approach with a thermogram

of a two micrometer ASW film that contains approximately 0.1 mole fraction of CH_3COOH dopants.

As shown in Figure 5.2, averaging the voltage and current data from 13 independent scans made it possible to improve the S/N ration in the endothermic upswing to a value near two, and facilitated the determination of T_g and ΔC_p with reasonable accuracy. According to the thermogram analysis shown in the figure, the glass transition temperature of doped ASW is 155 ± 3 K at a heating rate of approximately 5 kK/s. Such an accuracy in the determination of T_g from the thermogram is near or better than the overall systemic accuracy of temperature measurement of our FSC data acquisition system. The value of the endotherm magnitude was also determined from the thermogram. As shown in Figure 5.2, ΔC_p near 155 K is 0.4 ± 0.2 μJ/K. As I will show later in this chapter, such an estimate is important despite its relatively poor accuracy.

Figure 5.3 summarizes the results of FSC measurements conducted at heating rates varying from 25 to 600 kilo-Kelvins per second. As shown in the figure, increasing the heating rate from 5 to 600 kK/s results in a significant shift in the onset temperature of the glass transition from approximately 155 K to near 178 K, i.e., by more than 20 K. Although this is not immediately apparent in Figure 5.3, I also note that the increase in the T_g is also accompanied by an increase in ΔC_p. In summary, by varying the heating rate of FSC scans, i.e., by changing characteristic experimental time-scale of FSC measurement, it is possible to elucidate the temperature dependence of the kinetic (τ_h) and thermodynamic (ΔC_p) parameters of doped ASW. Immediately below I provide analysis and discussion of the essential results obtained in variable rate FSC experiments.

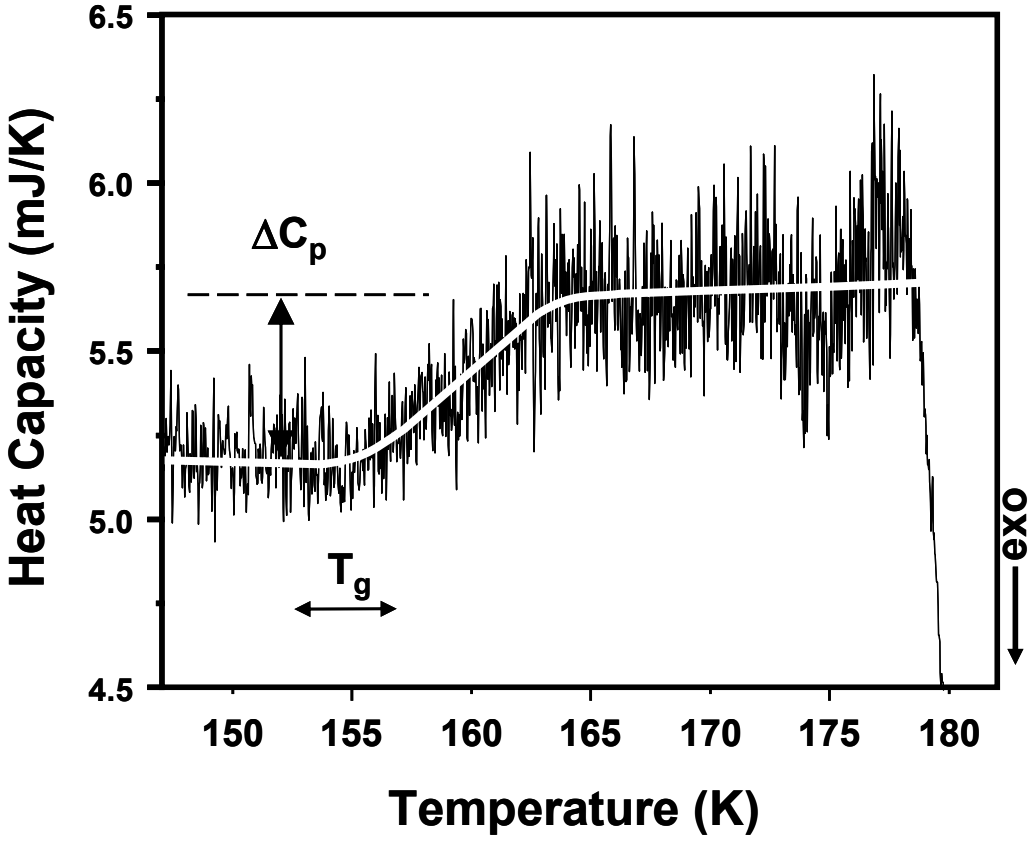

Figure 5.2. Thermogram of a ~2 μm CH3COOH-doped ASW film from a heating rate of approximately 5 kK/s (black line) and the average of thirteen thermograms of similar films, all using the same heating rate (white line). The average of the 13 scans made it possible to sufficiently improve the S/N ratio in order to more accurately determine the onset of the glass transition (T_g) to be 155 ±3 K and the jump in the endothermic upswing (ΔC_p) to be 0.4 ± 0.2 μJ/K.

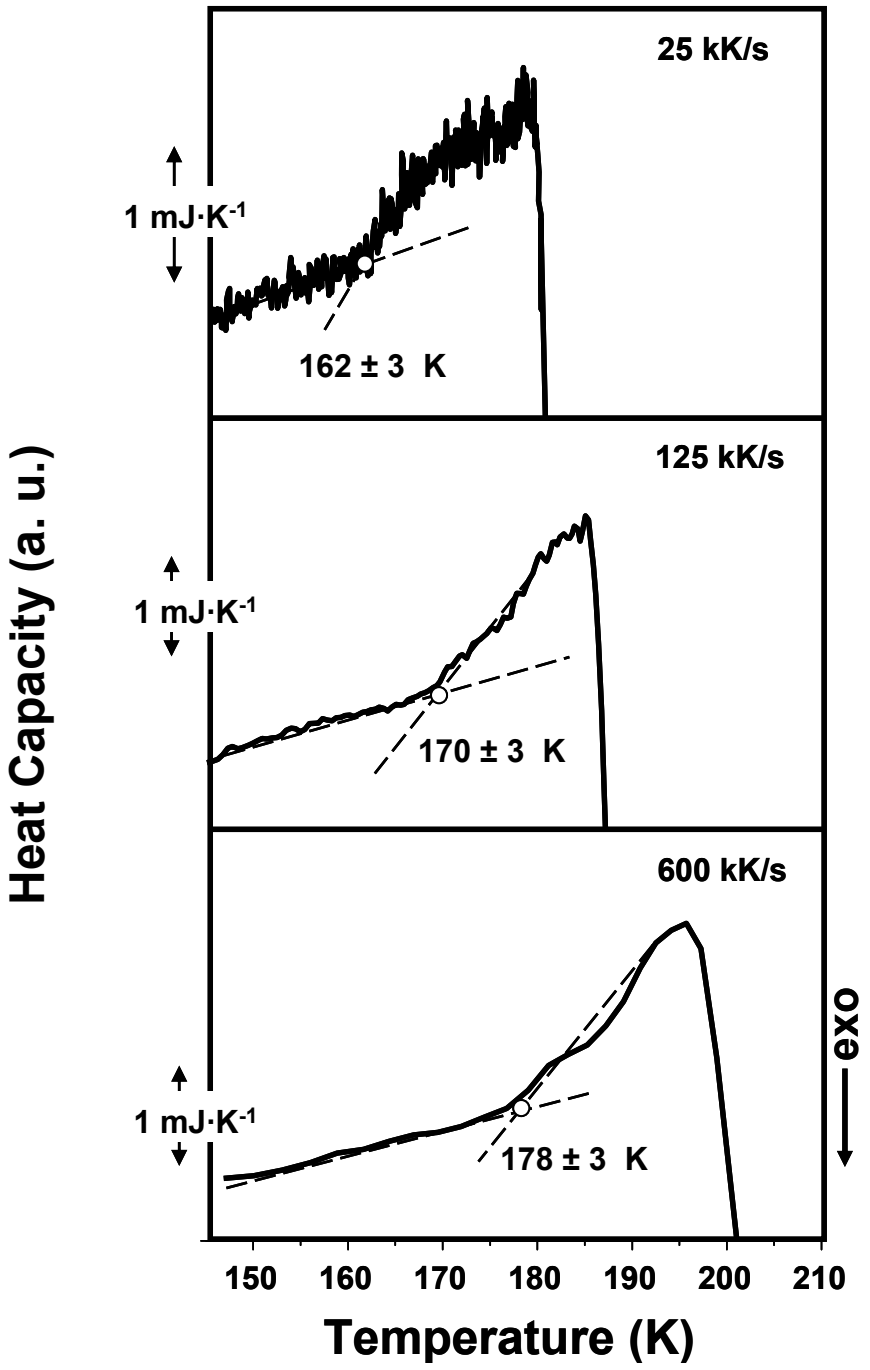

Figure 5.3. Thermograms of ~2 μm CH_3COOH-doped ASW films with heating rates varying from 25 kK/s to 600 kK/s. This increase in the heating rate results in a significant shift in the onset of the temperature of the glass transition from approximately 155 K to near 178 K and an increase in the value of ΔC_p.

5.4 Temperature Dependence of the Enthalpy Relaxation for Highly Perturbed ASW

The thermograms shown in Figures 5.2 and 5.3 along with the values of heating rates, contains a wealth of fundamental information on the thermodynamic properties of the doped ASW phase. I begin with a careful evaluation of the temperature dependence of the enthalpy relaxation time (τ_h) on temperature.

Figure 5.4 shows τ_h values for ASW doped with CH_3COOH at the level of approximately 0.1 (mole fraction). As already mentioned, the values of the enthalpy relaxation time are assumed to be numerically equal to the inverse of the heating rate. The corresponding temperatures are those of the onset of the glass endotherms in FSC thermograms measured at a particular heating rate. In addition to these data, the plot also shows the τ_h time value derived from DSC thermograms for bulk vitreous H_2O phase that was assumed to be "pure vitreous water" (open circle)[1,5].

As shown in Figure 5.4 the dependence of the enthalpy relaxation time on temperature between 155 K and 178 K closely follows the Arrhenius law. The apparent activation energy is 55 ± 2 kJ/mol. Furthermore, the Arrhenius fit of our FSC data, when extrapolated to 137 K, gives values of the enthalpy relaxation times that are close to those derived from DSC measurements. Note, however, that the DSC thermograms measured by Johari and coworkers were always assumed to be that of pure ASW. While I discuss the match between the relaxation times of doped and supposedly pure ASW near 137 K later in this chapter, I provide the analysis of the relaxation time data in the 155 K – 180 K region immediately below. This analysis is based on the Adam–Gibbs theory of kinetics near the

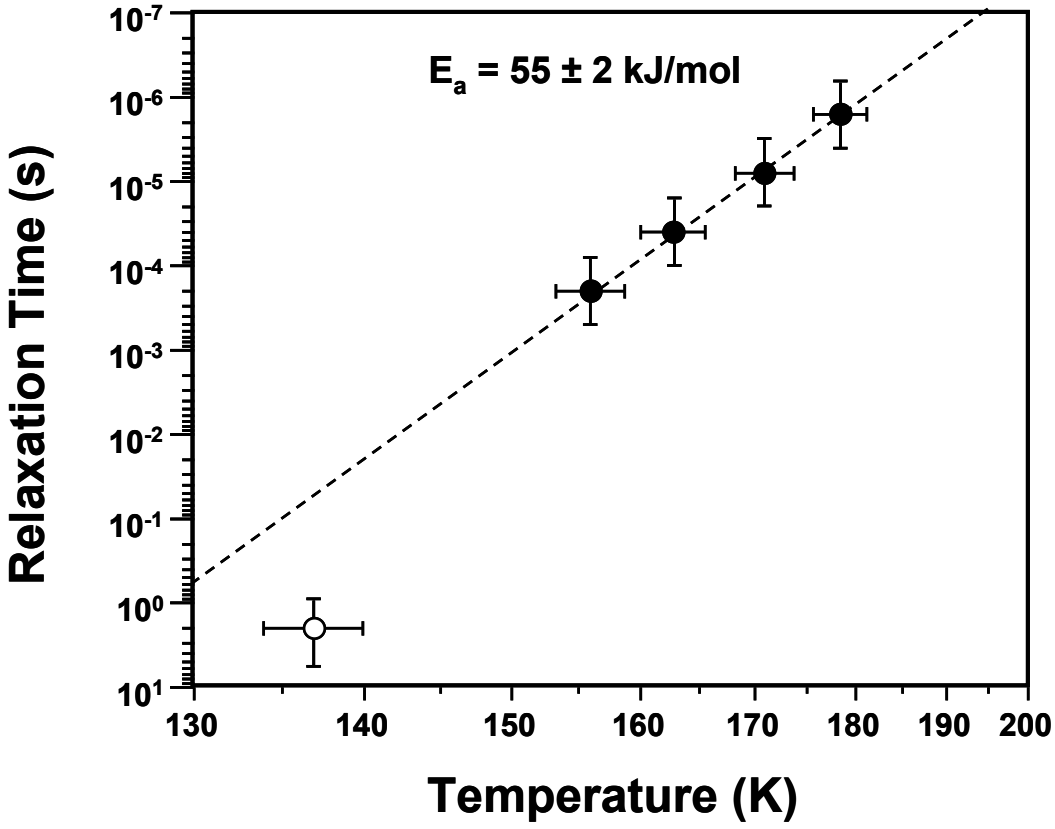

Figure 5.4. Dependence of the enthalpy relaxation time of ASW films doped with 0.1 mole fraction CH_3COOH (black circles) and a value derived from DSC thermograms for bulk vitreous H_2O phase that was assumed to be "pure vitreous water" (open circle) on temperature. The values of the enthalpy relaxation time are assumed to be numerically equal to the inverse of the heating rate. The ASW points closely follow Arrhenius law and have an apparent activation energy of 55 ± 2 kJ/mol. Furthermore, the Arrhenius fit of the FSC data, when extrapolated to 137 K, gives values of the enthalpy relaxation times, which are close to those derived from DSC measurements of supposedly pure water.

glass transition temperature, and provides further support for the Vicinal ASW conjecture introduced in Chapter 4.

5.5 Analysis of the Relaxation Data Based on the Adam–Gibbs Theory

The Arrhenius dependence of the enthalpy relaxation time observed in my FSC studies of ASW doped with acetic acid may seem surprising. Relatively few vitreous systems (pure liquids and solutions) demonstrate the so-called "strong" (i.e., Arrhenius-like) behavior of molecular kinetics on temperature. According to the Adam-Gibbs theory (AGT), the relaxation time, viscosity, and self-diffusion coefficients can be described by the modified transition state expression[6,7]:

$$\tau_h(\eta \ or \ D) \approx A \bullet e^{\frac{z^* \bullet \Delta\mu}{RT}} \tag{5.2}$$

where z^* (T) is the temperature dependent number of molecules which rearrange its molecular structure cooperatively, i.e., the size of the so-called cooperative domain; $\Delta\mu$ is the temperature-invariant energy barrier to the bond rearrangement of a single molecular entity; and R and T are the gas constant and the absolute temperature, respectively.

In so-called "fragile" liquids, the number of molecules exhibiting coherent kinetics during relaxation, i.e., the average size of the cooperative domains, z^*, is strongly temperature dependent. A rapid increase in the cooperativity of molecular motion and the corresponding increase in its effective activation energy, leads to a rapid decrease in the apparent self-diffusivity and an increase in viscosity and relaxation times. Depending on the assumptions on the temperature dependence of the cooperativity scale, Equation 5.2 can be reduced to an explicit expression such as a Vogel-Fulcher-Tammann (VFT) equation[6].

For example, according to the continuity hypothesis discussed in the Introduction and previous chapters, the kinetic parameter of ASW should exhibit strong, non-Arrhenius variations as the temperature approaches the postulated standard glass transition.

In Chapter 4 of this thesis, I argued that guest species (molecular impurities) incorporated into ASW matrix may locally change the kinetic properties of ASW, thus, resulting in a shell of viscous liquid around the impurity. The simple Arrhenius dependence of the enthalpy relaxation time on temperature observed in our experiments may seem to contradict this suggestion; however, the Adam-Gibbs theory, assumes that the growth of the cooperative domain at lower temperatures is not constrained by the size of the system. I note that this assumption of the AGT is not valid in the case of confined systems such as liquid filled nanopores or liquid nanodroplets. I also note that our vicinal ASW hypothesis assumes that the viscous shell around the impurity molecule contains approximately 25 water molecules, i.e., represent a typical case of confined system.

Although caution must be exercised while applying the Adam-Gibbs concept to condensed phase systems of microscopic dimensions, the AGT approach can still be adopted for interpreting the molecular kinetics of liquid in nanopores[8] or under other types of nanoscale confinement. Indeed, in the framework of the Adam-Gibbs approach, the molecular kinetics in a confined system differ from those in the bulk only by the dependence of cooperativity scale (z^*) on temperature. For example, in the case of ASW doped with 0.1 mole fraction of CH_3COOH, i.e., in the case of highly perturbed ASW, the maximum size of the cooperative domain is unlikely to exceed 10 H_2O molecules due to disruption of ASW's hydrogen bond network by closely spaced CH_3COOH molecules. In

other words, under conditions of confinement, the average size of the cooperative domains is "pinned down" at a temperature where the cooperative scale approaches the dimensions of the confinement. As illustrated in Figure 5.5, the "cut off" effect of the confinement would prevent a rapid slowing down of molecular motion in a fragile liquid at a certain temperature, $T_{cut\text{-}off}$ ("Cut off" or "Pin down" temperature). At temperatures below $T_{cut\text{-}off}$, the average size of the cooperative molecular domain reaches its maximum possible value, which is defined by dimensions of confinement. While molecular kinetics in unrestrained bulk liquid may continue to decrease with temperature due to an increase in the size of cooperative domains, the confined liquid would follow simple Arrhenius dependence. I emphasize that such a "cut-off" impact of confinement on the kinetic properties of water was observed in several recent studies[8]. For instance, quasi-elastic neutron scattering (QENS) measurements of the relaxation times of water in nanoporous (14 Å) silica clearly show that the fragile-like (none-Arrhenius) behavior of the relaxation time at higher temperatures change the Arrhenius dependence below 220 K.

Figure 5.6 compares the enthalpy relaxation time value of doped ASW at temperatures from 155 K to 178 K with the dielectric relaxation times of bulk water at temperatures near ambient. The dotted line is the Arrhenius fit of FSC data for doped ASW with apparent activation energy of 55 kJ/mol. The solid line shows the power law fit of the dielectric spectroscopy data, which assumes a dramatic slowdown in the molecular kinetics of water near singularity temperature of 228 K.

According to the essential conclusions of Chapter 4, τ_h measured in FSC experiments of doped ASW is the enthalpy relaxation time of water confined to a solvation

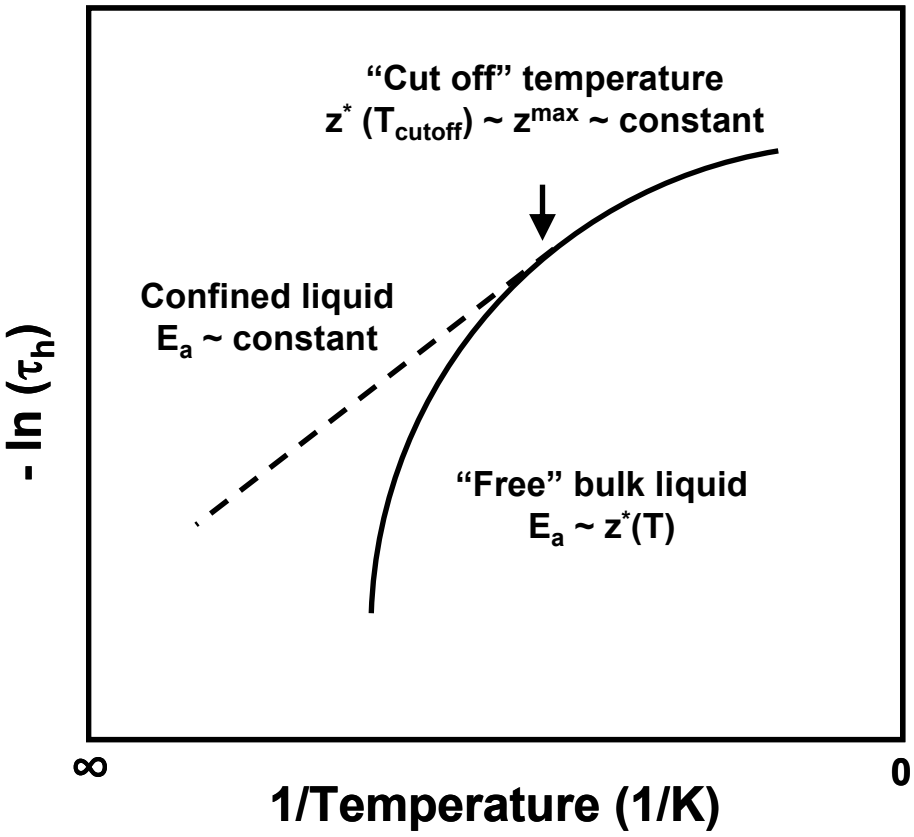

Figure 5.5. The Adams-Gibbs theory (AGT) of confinement. As the temperature of a bulk liquid increases, its relaxation time decreases to fit a Vogel-Fulcher-Tammann (VFT) equation and exhibits a strong, non-Arrhenius variation as the temperature approaches the liquid's postulated standard glass transition. In the case of a confined liquid, the relaxation time decreases identically to that of a "free" bulk liquid up to the "cut off" temperature, at which point the cooperative domain of the liquid's molecules reaches its maximum possible confinement and results in a strong Arrhenius behavior.

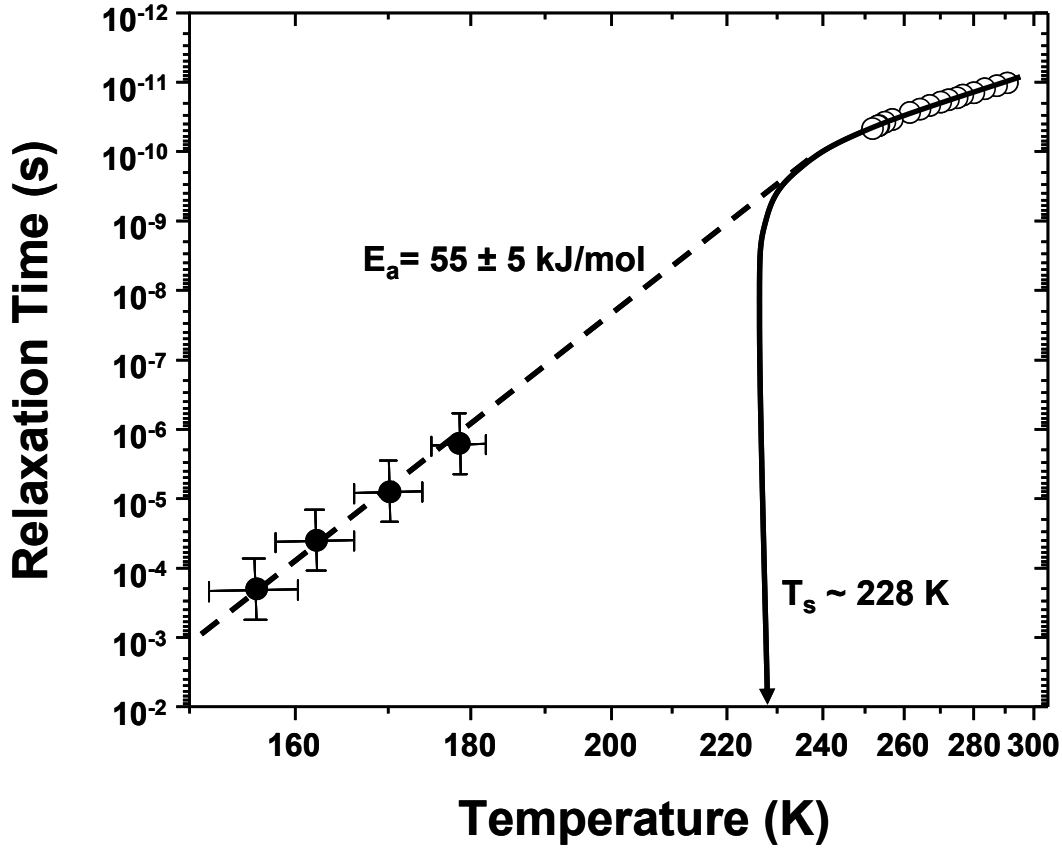

Figure 5.6. Comparison of the enthalpy relaxation time values of ASW films doped with a 0.1 mole fraction of CH_3COOH (black circles) with the dielectric relaxation time data of bulk, pure water at ambient temperatures (open circles). The doped ASW exhibits a strong Arrhenius behavior with an activation energy of 55 ± 5 kJ/mol (dotted line). The solid line represents the power law fit of the dielectric spectroscopy data. According to the Adams-Gibbs theory, the size of the cooperatively rearranging domains in our CH_3COOH doped ASW is expected to be between 8 and 3 molecules, which is similar to those of water confined to nanoscale dimensions (nanopores).

shell around the impurity. Thus, the graph in Figure 5.6 essentially represents the test of our vicinal ASW hypothesis from the standpoint of the Adam-Gibbs theory. Indeed, the ASW doped with CH_3COOH at levels above 0.1 is a good model of the highly perturbed ASW in the solvation shell of a molecular impurity in the case of arbitrary low dopant concentrations. As shown in Figure 5.6, the Arrhenius-like dependence of the enthalpy relaxation time for doped ASW can be easily extrapolated to higher temperatures, where it is tangential to the relaxation time data of bulk liquid water. In others words, the observed dependence of the enthalpy relaxation time of doped ASW is consistent with the AGT. While the bulk, pure water may undergo the dramatic increase in enthalpy relaxation time near 228 K, disruption of water's ability to form cooperative hydrogen bond network in the vicinity of impurities is likely to result in highly mobile (liquid-like) vicinal phase.

Before proceeding to the next subject of the discussion, I would like to give an estimate of the maximum possible size of the H_2O cooperative rearrangement domain in ASW doped with a 0.1 mole fraction of CH_3COOH. Such an estimate is possible if the value of $\Delta\mu$, which is defined as "…largely the energy barrier resisting the cooperative rearrangement per monomer segment"[7]. The average number of molecules capable of rearranging cooperatively under confinement can then be calculated by dividing the effective activation energy at temperatures below $T_{cut\text{-}off}$ (55 ± 2 kJ/mol in the case of doped ASW) by the energy barrier to rearrangement. Assuming that, in the case of ASW, the energy barrier to rearrangement per H_2O molecule is between 7 and 18 kJ/mol (energy of a single hydrogen bond), the size of the cooperatively rearranging domains in our highly perturbed, CH_3COOH-doped ASW is expected to be between 8 and 3 molecules. Taking

into account, the ratio of CH_3COOH to H_2O in our ASW films (1:10), such an estimate is in perfect agreement with the dimensions of the confinement imposed on the maximum cooperative rearrangement scale.

In summary, the observed enthalpy relaxation times for ASW doped with 0.1 mole fraction of CH_3COOH are in perfect agreement with our vicinal ASW conjecture and are consistent with the AGT. According to the Adam-Gibbs analysis described in this section, the molecular kinetics of the vicinal ASW phase are similar to those of water confined to nanoscale dimensions, where the cooperative relaxation at low temperatures becomes impossible.

5.6 Heat Capacity of Vicinal ASW at Various Temperatures

In addition to kinetic data (i.e., the enthalpy relaxation times, activation barrier), the FSC thermograms in Figures 5.2 and 5.3 provide information on the thermodynamic functions of doped ASW, such as its heat capacity dependence on temperature. The magnitude of a glass endotherm, ΔC_p, (see Figure 5.2) can be used to estimate the specific heat capacity of doped ASW if the mass of the sample is known. Note that in our FSC experiments mass and thickness of ASW or ice films can be determined from FSC thermograms with accuracy on the order of 10% (see Chapter 2 for details). Thus, determination of the specific heat capacity of perturbed (vicinal) ASW from the FSC thermograms becomes possible.

Figure 5.7 compares the heat capacity (solid circles) of doped ASW films employed in our FSC studies with the heat capacity of water confined in silica gel nanopores ranging from 3 to 50 nm (blue circles). The heat capacity of the nanoconfined water was measured

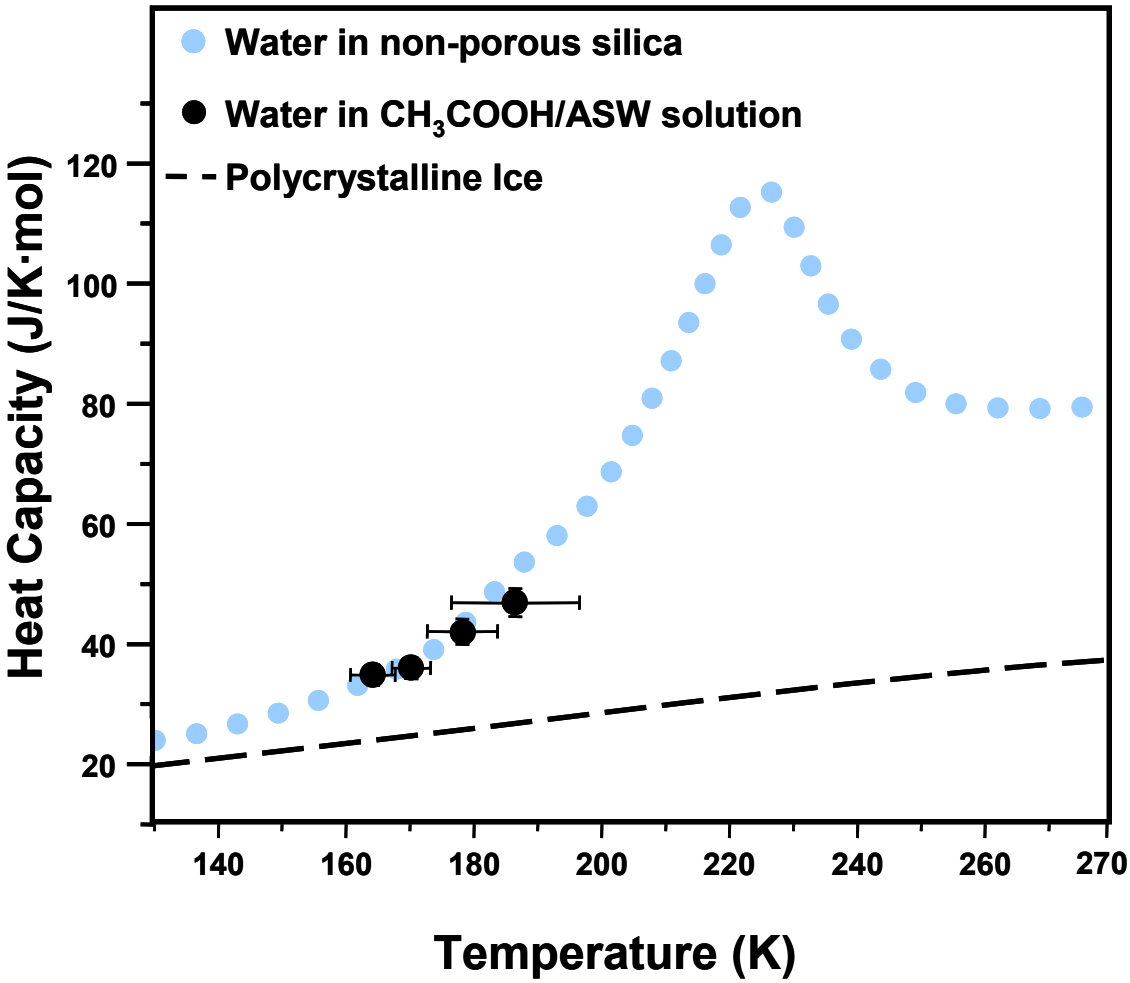

Figure 5.7. Thermogram comparing the heat capacities of doped ASW films employed in FSC studies (black circles) with the heat capacity of water confined in silica gel nanopores ranging from 3 to 50 nm (blue circles) and that of polycrystalline ice (dashed line). The most striking feature is the close match between the doped ASW films and that of the pure, confined water, which leads to the conclusion that the addition of dopants in the ASW matrix impacts the structure and kinetics of ASW in ways that are similar to those characteristic of nanoconfined water.

by the Oguni group[1,9] in careful DSC experiments. Note that due to the small pore sizes, the crystallization of water was suppressed in the entire temperature range. Using nanoporous mediums with different pore sizes, these researchers were also able to separate the properties of "surface water" from those of "internal" water in their smallest-pore samples. The main feature of the C_p curve of nanoconfined water is the peak near 228 K, which reflects the possibility of complex structural and kinetic changes near the temperature of this "singularity." Finally, the heat capacity of crystalline ice is shown in the plot (dashed line).

The most striking feature of the plots in Figure 5.7 is the close match in heat capacity of our doped ASW and water confined to nanopores. Taking into account the uniqueness of the temperature dependence of water's C_p, such a similarity in heat capacity of a CH_3COOH/ASW solution and water in nanoporous silica gel is remarkable and instantly leads to several important conclusions:

1. Based on similarities between the FSC thermograms of ASW doped with a distinct chemical species (CCl_4, CH_3COOH, C_2H_5OH, and $C_5H_{11}OH$), I have argued in Chapter 4 that the observed glass endotherms are due to the solvent (ASW) kinetics. Because the C_p values of doped ASW in Figure 5.7 were determined from the glass endotherm magnitude and because these are in excellent agreement with C_p values of water (albeit confined), this earlier conclusion is proven unambiguously.

2. I have argued in Section 5.5 of this chapter that addition (or rather "insertion") of guest species in the ASW matrix impacts the structure and kinetics of ASW in ways that are very similar to those characteristic of nanoconfined water, and can be explained in the framework of the AGT by limits imposed by confinement on the scale of water's cooperative rearrangement. The near match between C_p values of water in doped ASW and those in silica gel nanopores provides proof of this claim. Because the heat capacity of a condensed phase system is defined by its accessible structural configurations and because the structure of hydrogen bonded liquids is complex and highly temperature-variant, the match in heat capacities of water in doped ASW and in silica gel nanopores strongly implies that water's molecular structure and kinetics are similar in both environments.

5.7 Molecular Structure and Dynamics in ASW in the Case of Low Concentration of Impurities

The data and analysis present in the previous sections of this chapter and in Chapter 4 clearly show that disrupting water's ability to form extended hydrogen bond networks either by confining water to nanopores or by "implanting" dopant molecules into ASW, creates an environment where "hardening" of liquid H_2O into a glassy state is impossible. Based on this observation, I would now like to consider the special case of extremely low concentrations of dopant species.

In the case of exceedingly low concentrations of guest species, the bulk of ASW should indeed be able to undergo a rapid increase in the size of cooperatively rearranging domains characterized by an extensive coherent hydrogen bond network. Despite this assumption, the hydrogen bond network must still be disrupted in the immediate vicinity of a dopant molecule, unless its size is significantly smaller than a typical H_2O intermolecular distance (3.5 A). In the case of ASW or ice, introduction of virtually any organic molecule necessitates some hydrogen bond breaking and/or rearrangement around a guest species. Therefore, despite the fact that at low concentrations of impurities the bulk of vitreous solution may behave as pure ASW, *there must be a small volume around an impurity molecule where the number of molecules capable of rearranging cooperatively is limited*.

Before proceeding, I must stress that the vicinal volume is *not* the region where any hydrogen bonding is disrupted, but the volume where the number of H_2O molecules rearranging cooperatively is limited. Unless the "polywater" hypothesis[10] is resurrected, it is safe to assume that at temperatures near ambient, formation of an *extended* hydrogen bond networks is impossible. Nevertheless, even for water under ambient conditions, cooperative molecular motion of H_2O includes at least a few monomers. This is evident from the weakly non-Arrhenius temperature dependence of dielectric relaxation times, viscosity, and self-diffusivity between 250 and 300 K (for example, see Figure 5.6).

If the impact of impurities on the molecular structure and kinetics of ASW is similar to that induced by a confinement, then it is easy to predict variations in enthalpy relaxation times in the limit of low dopant concentrations (below mole fraction of 0.04). The essential difference between low and high impurity concentration cases is the

maximum size of the cooperatively rearranging domains. For example, at concentration above 0.04, the maximum possible size of the cooperatively rearranging H_2O domains is defined by an average distance between the impurity species, i.e., is inversely proportional to dopant concentration. However, at lower dopant concentrations (below dopant mole fraction of 0.04), the size of cooperative domains must become independent of the concentration of impurities. Figure 5.8 illustrates possible scenarios for the enthalpy relaxation time variation with temperature in the limit of low impurity concentrations.

As shown in the figure, reduction in the concentration of impurities from 0.1 to 0.04 must result in an *increase* in the maximum size of the cooperatively rearranging H_2O domains from 10 to 25 molecules. According to the Adam-Gibbs theory, such an increase in maximum size of cooperatively rearranging H_2O domains must result in an approximately two-fold increase in the apparent activation energy. If we assume that the length scale of perturbation to the hydrogen bond network by an impurity molecule is temperature-invariant, the resulting temperature dependence of τ_h in the limit of low concentrations must also be Arrhenius as for any other confined water. If, however, the effective diameter of the vicinal ASW shell is a function of temperature, some deviations from Arrhenius dependence may result.

Although I am unable to unambiguously determine whether or not the effective perturbation radius depends on temperature with the currently available FSC data, I emphasize that the concentration dependence (or rather lack thereof) of the T_g described in Chapter 4 of this thesis is in perfect agreement with predictions illustrated in Figure 5.8. Indeed, according to Figure 5.8, the τ_h should become independent of the concentration of

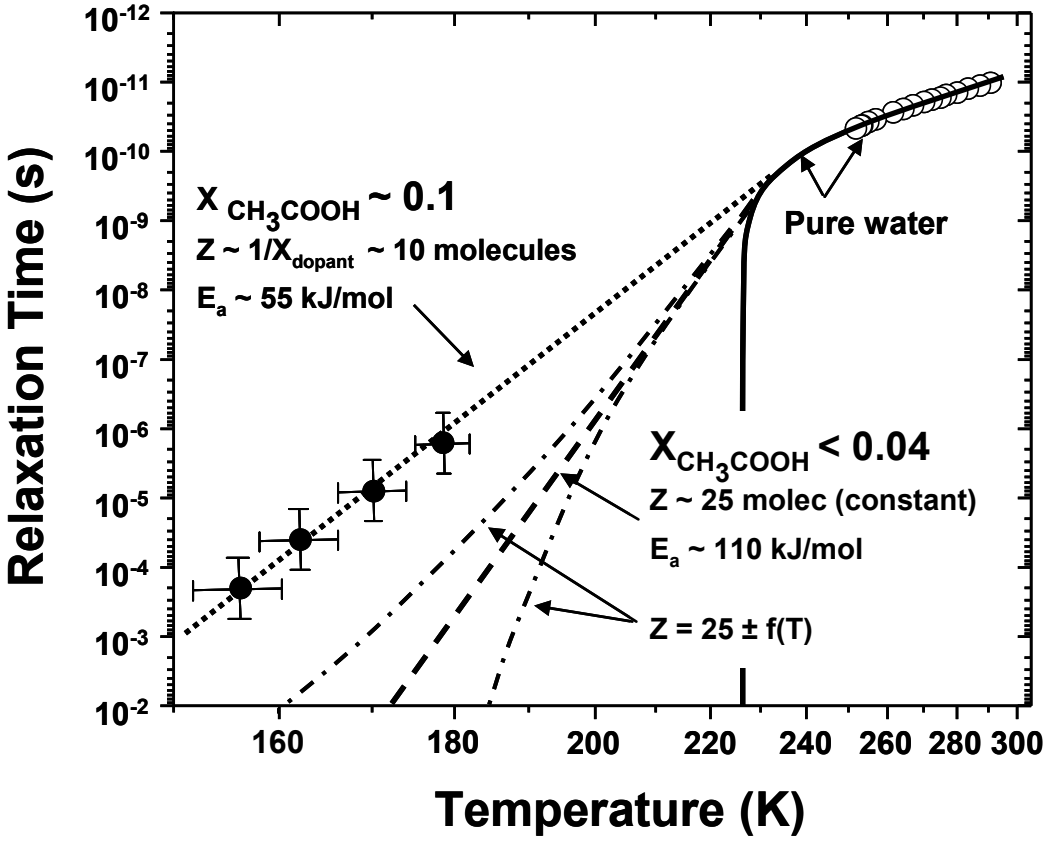

Figure 5.8. The Adams-Gibbs theory of confinement with films of dopant concentrations varying from 0.1 to 0.04 mole fraction. A reduction in the concentration of impurities must result in an increase in the maximum size of the cooperatively rearranging H_2O domains, and, according to the Adam-Gibbs theory, an increase in the apparent activation energy.

impurities when it is below 0.04 (mole fraction). This is exactly what I observed in FSC experiments described in Chapter 4. According to the central feature of the FSC approach, the concentration- invariant τ_h must result in a concentration-invariant temperature of glass transition in thermograms of doped ASW measured at a "fixed" heating rate of 10^5 K/s (see Fig 4.8 of Chapter 4).

5.8 Origins of Weak Endothermic Features in Conventional DSC Thermograms Observed at 137 K

Almost 25 years ago, in a few DSC experiments with vitrified water, Johari and coworkers observed a weak endothermic feature near 137 K, which was attributed to the glass transition of water[5]. Since then, many DSC studies have been conducted where the observation of similar endotherms sometimes results and other times it does not. The lack of consistency in the observation of a glass transition by DSC has led some to question the validity of the original and later Johari studies. Immediately below, I provide further basis for the rebuttal of the Johari's assignment of T_g for pure water to temperatures near 137 K.

According to the discussion presented in section 5.7 of this chapter, even in the case of exceedingly low concentrations of impurities, the vicinity of an impurity molecule may present an environment where water cannot solidify into a glassy state due to limitations imposed by the impurity species on the extent of the cooperative rearrangement domain. According to results described in this chapter and in Chapter 4, the region of perturbation around even small organic species (ethanol, acetic acid, pentanol, etc.) encompasses up to 25 H_2O molecules. Based on the AGT theory, I have made a few predictions on the

possible temperature dependence of τ_h for such vicinal water. It is interesting to compare some of Johari's results to these predictions.

Figure 5.9 shows the enthalpy relaxation times of vicinal ASW doped with 0.1 mole fraction of CH_3COOH (dotted line) and at mole fractions below 0.04 (solid line). Note that according to predictions of Section 5.7, the vicinal water relaxation time dependence on temperature should become independent of the concentration of impurities below 0.04 (mole fraction). Thus, the shaded region between the dotted and solid lines in Figure 5.9 represents the range of possible relaxation time values which would be expected for *a contaminated* vitreous water sample that may have an arbitrarily low number of impurity species. As shown in the figure, the most significant results of Johari's studies, i.e., the enthalpy relaxation time derived from his DSC measurements[5] and the dielectric relaxation times[11], fall neatly in the region of τ_h values characteristic of the vicinal water. I emphasize that the DSC and dielectric spectroscopy studies conducted by this researcher were never designed to test the water samples for the presence of impurities. I must also point out that the dielectric spectroscopy measurements were not even conducted with pure water but water absorbed in Poly (2-hydroxyethyl) methacrylate, which "was swollen in water for several weeks" to prevent freezing at cryogenic temperatures. In short, the results and analysis presented in this chapter provide significant evidence that the endothermic features sporadically observed in some DSC studies may originate from impurities or contaminants intentionally or unintentionally introduced into vitreous water samples.

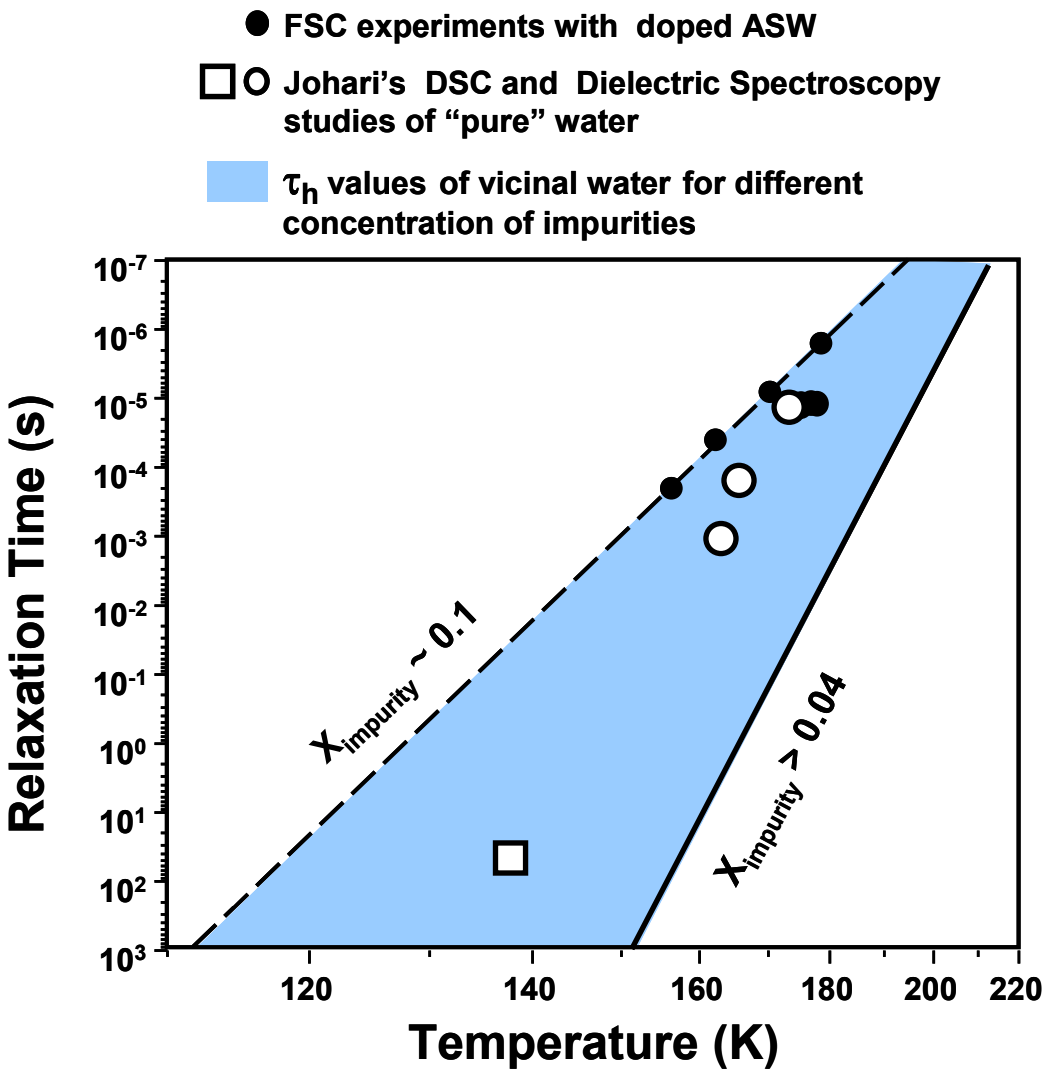

Figure 5.9. The enthalpy relaxation times of vicinal ASW doped with 0.1 mole fraction of CH_3COOH (black circles with dotted line) and at mole fractions below 0.04 (solid line). The shaded region between the two lines in the figure represents the range of possible relaxation time values which would be expected for a contaminated vitreous water sample that may have an arbitrarily low number of impurity species. The DSC (open square) and dielectric spectroscopy data (open circles) from Johari's studies of "pure" water fall neatly within the shaded region. Thus, data from "pure" water samples that sporadically display endothermic features may actually come from unintended impurities.

5.9 Summary

Based on near match in the heat capacities of ASW doped with acetic acid and water confined to nanopores of silica gel, I demonstrate that the impact of impurities on molecular kinetics and structure of the surrounding H_2O matrix is nearly identical to that of nanopores. The Arrhenius temperature dependence of water's relaxation times in doped ASW further strengthen this conclusion and indicates that the confinement and impurity effects can be well explained using the Adam-Gibbs theory. According to the AGT-based interpretation, confining water to nanoscopic dimensions and/or the introduction of impurities to the ASW matrix limits the maximum possible cooperative rearrangement scale, and, thus, prevents water's transition into a glassy state. Finally, I show that many results of previous studies, where unusually rapid molecular kinetics were observed in vitreous water samples, can be explained by impact of impurities and/or confinement introduced into a vitreous water sample either intentionally or by happenstance.

References

1. Angell, C. A. *Science* **2008**, *319*, 582.
2. Sadtchenko, V.; Lu, H.; McCartney, S. *J. Chem. Phys.* **2007**, *127*, 2.
3. Chonde, M.; Brindza, M.; Sadtchenko, V. *J. Chem. Phys.* **2006**, *125*, 10.
4. Johari, G. P.; Fleissner, G.; Hallbrucker, A.; Mayer, E. *J. Phys. Chem.* **1994**, *98*, 4719.
5. Hallbrucker, A.; Mayer, E.; Johari, G. P. *J. Phys. Chem.* **1989**, *93*, 4986.
6. Hodge, I. M. *J. Res. Natl. Inst. Stand. Technol.* **1997**, *102*, 195.
7. Gibbs, J. A. a. J. H. *J. Chem. Phys.* **1965**, *45*.
8. Mallamace, F.; Branca, C.; Broccio, M.; Corsaro, C.; Gonzalez-Segredo, N.; Spooren, J.; Stanley, H. E.; Chen, S. H. *Eur. Phys. J.-Spec. Top.* **2008**, *161*, 19.
9. Oguni, M.; Maruyama, S.; Wakabayashi, K.; Nagoe, A. *Chem.-Asian J.* **2007**, *2*, 514.
10. Rousseau, D.; Porto, S. *Science* **1970**, 167, 1715-1719.
11. Johari, G. P. *J. Chem. Phys.* **1996**, *105*, 7079.

Chapter 6: Variable Rate Fast Scanning Calorimetry Studies of Pure Amorphous Solid Water Crystallization

6.1 Introduction

In the last three chapters of this thesis, I have argued consistently that sporadic observation of liquid-like behavior (glass transition endotherms, fragile-like temperature dependence of H_2O self-diffusivity, and the dielectric relaxation time) can be attributed to the vicinal amorphous solid water (ASW) phase formed near impurities and/or structural defects in otherwise cohesive and, therefore, immobile (glassy) ASW matrix. So far, due to the absence of a detectable glass transition endotherm in fast scanning calorimetry (FSC) thermograms of pure ASW[1], my approach to demonstrating the validity of this conjecture consisted in careful FSC studies of ASW doped with distinct chemical species. Nevertheless, as I show in this chapter, variable rate FSC makes it possible to gain important insights into the nature of pure ASW at temperatures below 228 K through the analysis of temperature dependence of its crystallization rate.

As explained in the Section 1.3.5, not only the glass transition temperature but also the characteristic temperature of the onset of crystallization must vary with the heating rate of an FSC scan. As previously described, the characteristic temperature of crystallization is the temperature at which a sufficiently large fraction of ASW crystallizes so that the crystallization enthalpy release becomes detectable, i.e., where the characteristic time of crystallization (τ_{CR}) of a few percent of an initially non-crystalline sample becomes

comparable to the experimental observation time. Thus, by varying the heating rate, i.e., by varying the experimental observation time, the characteristic crystallization time at various temperatures can be estimated. Since the characteristic τ_{CR} is essentially an inverse of the crystallization rate, its dependence on temperature can be analyzed using an appropriate theoretical model of crystallization to derive important microscopic properties of ASW, such as the activation energy for H_2O self-diffusion in pure ASW. In the following sections of this chapter, I report the results and analysis of FSC studies of pure ASW crystallization at heating rate varying from $3 \cdot 10^3$ K/s to $1.6 \cdot 10^6$ K/s.

6.2. Experimental Arrangement

The experimental apparatus and procedures describe in this chapter are identical to those used in variable rate FSC studies of the glass transition phenomena in ASW doped with CH_3COOH (see Chapter 5). The obvious difference in the experiments reported in this chapter is the presence of molecular impurities in the ASW samples. While the variable rate FSC experiments of Chapter 5 were conducted with ASW containing 0.1 mole fraction of CH_3COOH, the concentration of organic impurities in ASW samples in the crystallization experiments was below the detection limits of the mass spectrometer (MS) of the FTDS-FSC apparatus. According to our estimates, the detection limits of the MS are at least 10^{-4} mole fraction for species such as CH_3^+, CH^+, Cl^+ and other fragment ions characteristic of organic species, chlorofluorocarbons, silicon based diffusion pump oil, and other potentially volatile chemical contaminants.

As illustrated in Figure 6.1, adjustment of the biasing voltage across the single filament calorimeter from 1.5 V to 10 V results in a *three orders* of magnitude change in

the scanning rate of FSC experiments near the crystallization onset temperature. Note that the crystallization of ASW is manifested in the heating curves as a sudden increase in the rate of filament heating. The onset of crystallization is marked by intersecting dashed lines on each of the heating curves in Figure 6.1.

The thickness of the ASW films in these variable rate FSC studies was between 1 μm and 2 μm. As I have previously mentioned, the thickness of the films was chosen so that the typical thermal equilibration time would not exceed the characteristic experimental time (1K/Q). This ensured the lack of any significant thermal lags and gradients in the films during the FSC scans.

6.3 Analysis and Discussion

Data shown in Figure 6.1 was used to estimate the characteristic crystallization time at various temperatures. Once again, it was assumed that τ_{CR} at the onset temperature of crystallization is within an order of magnitude of the experimental observation time. The later is postulated in FSC experiments as being numerically equal to the inverse of the heating rate (see Chapter 3).

Figure 6.2 summarizes the results of analysis of the heating curves shown in Figure 6.1. It shows the characteristic crystallization time as a function of temperature between 185 K and 215 K estimated from variable rate FSC experiments (black circles). In addition to the FSC results, Figure 6.2 also shows the characteristic time determined from past low temperature studies of ASW vaporization[2] (grey circles). In those experiments, thin

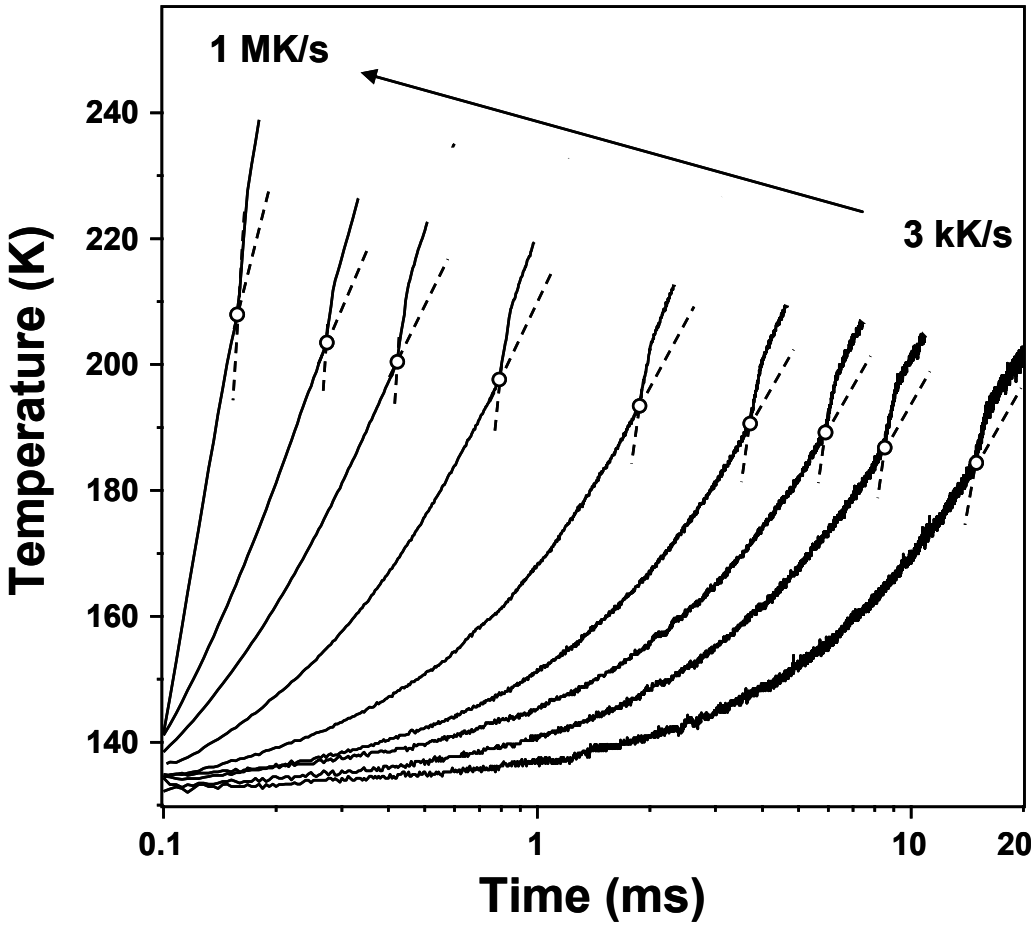

Figure 6.1. Heating curves of ASW films from variable rate FSC experiments. By systematically changing the biasing voltage from 1.5 V to 10 V across the filament, the heating rates were varied from 3 kK/s to 1 MK/s; thereby, varying the onset and duration of crystallization of the ASW film. The crystallization of each ASW film is manifested on the heating curves as a sudden increase in the temperature of the films (marked by intersecting dashed lines).

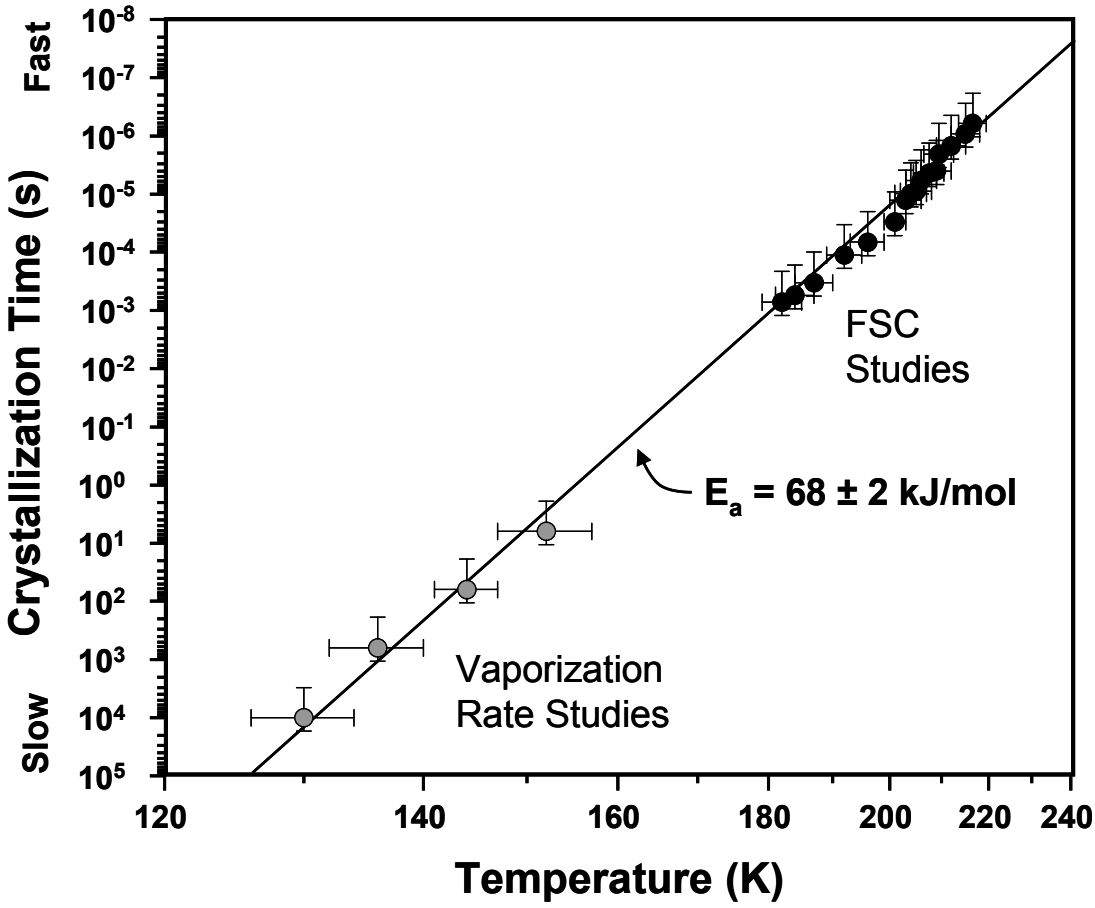

Figure 6.2. Characteristic crystallization time as a function of temperature derived from data in Figure 6.1. The black circles represent the results of FSC experiments, while the grey circles represent similar data obtained from temperature programmed desorption (TPD) experiments of thin (200 nm – 500 nm) ASW films. As demonstrated by the solid line, τ_{CR} values measured with FSC at temperatures near 200 K and those estimated from TPD experiments near 140 K, can be interpolated using a simple Arrhenius function, despite the differences between ASW sample geometry, dimensions, and the experimental techniques employed.

(200 nm - 500 nm) ASW films were subjected to liner heating in temperature programmed desorption (TPD) experiments and their vaporization rate were measured with a mass spectrometer. Due to the difference between vaporization rate in ASW and crystalline ice, the onset of initially amorphous films was manifested in TPD diagrams as a sudden decrease in the vaporization rate, making it possible to determine the crystallization onset temperature for a particular heating rate.

As demonstrated by the solid line in Figure 6.2, τ_{CR} values measured with FSC at temperatures near 200 K and those estimated from TPD experiments near 140 K, can be interpolated using a simple Arrhenius function, despite the differences between ASW sample geometry, dimensions, and the experimental techniques employed. In other words, the crystallization kinetics (τ_{CR}) do *not* show any deviations from Arrhenius law near the postulated glass transition temperature of 136 K. Furthermore, the apparent activation energy of crystallization (68 ± 2 kJ/mol) at temperatures between 185 K and 215 K is in excellent agreement with the results of previous (low temperature) measurements, which typically gave E_a a value near 67 kJ/mol[3-7].

Simple Arrhenius continuity between the two sets of crystallization rate data, which are separated by almost a 100 K, make it possible to derive important conclusions about the physical nature of pure ASW, using an appropriate crystallization model. Immediately below, I describe such an analysis.

It follows from the continuity in crystallization kinetics over the temperature interval from cryogenic to near 220 K, that the crystallization of ASW samples in my FSC experiments and in those conducted by others at lower temperatures are essentially the

same. According to extensive investigations[4,5,7], ASW crystallization is well described by the Avrami equation[8]:

$$X_{CR} = 1 - e^{-(kt)^n} \tag{6.1}$$

where X_{CR} is the fraction of the amorphous sample crystallized over the time interval, t; k is the crystallization rate constant; and n is the Avrami exponent, which characterizes the details of the process such as where crystallization occurs (bulk or interface), how the growth of crystallites proceeds (isotropic or anisotropic), etc. For instance, the crystallization mechanism, which involves spatially random bulk nucleation and isotropic three-dimensional growth of the crystallites, typically results in an Avrami exponent of four[5,8].

The characteristic crystallization time can be derived from Equation 6.1 by assuming that τ_{CR} corresponds to the crystallization of a certain fraction of the sample:

$$\tau_{CR} = \ln(f)^{\frac{1}{n}} \bullet k^{-1} \tag{6.2}$$

where f is the tabulated crystallized fraction of the amorphous sample. For instance, for the half-time of crystallization, f is set at the value of 2. Thus, as it follows from Equation 6.2, an Arrhenius plot of τ_{CR} values gives the apparent activation energy of the Avrami crystallization rate constant.

The Avrami activation energy (apparent activation energy of crystallization), E_a, is associated with two kinetic barriers: one due to the formation of crystalline nuclei, E_N, and another due to the growth of the crystalline nuclei, E_G. In a crystallization process, which proceeds via the spatially random bulk nucleation and isotropic three-dimensional growth of the crystallites, the Avrami constant, k, is proportional to $(J \cdot G^3)^{1/4}$, where J and G are the

rates of nucleation and nuclei growth respectively[5,6]. Thus, for this particular crystallization mechanism the following relationship between relevant activation energies must be true:

$$4E_a = E_N + 3E_G \tag{6.3}$$

At the present time, I cannot unambiguously verify that pure ASW crystallization in our FSC experiments does proceed via a spatially random bulk nucleation and isotropic three-dimensional growth of the crystallites, i.e., that Equation 6.3 represents the exact relationship between the relevant activation energies. Nevertheless, I emphasize that independent of the fine details of the crystallization process, the kinetics of supercooled liquid crystallization are always governed by competition between the spontaneous formation of crystalline nuclei and the molecular transport from liquid to the crystallites (i.e. crystallite growth)[6]. In other words, independent of particular details of the process, a relationship similar to Equation 6.3 for the relevant activation energies of crystallization process must exist. Taking this simple fact into consideration, I can now elucidate the meaning of the observed simple Arrhenius temperature dependence for τ_{CR} in the range of temperatures from cryogenic to near 220 K.

As shown, in Figure 6.2, the observed simple dependence of the crystallization rate is once again inconsistent with the conjecture that pure ASW is a "fragile" liquid in the temperature range from 136 K to ambient. If pure ASW is a fragile liquid above 136 K, its microscopic transport properties must vary in a non-Arrhenius fashion over the temperature range from 136 K to 220 K. In other words, the activation energy for crystallite growth, E_G, must be a strong function of temperature because the growth of crystalline nuclei is

governed by H_2O molecular transport from the amorphous phase toward the crystallite/ASW interface.

If pure ASW is a fragile liquid above 136 K, the activation energy for spontaneous formation of crystalline nuclei, E_N, must also demonstrate significant variations over the hundred degree temperature interval in Figure 6.3. Indeed, the barrier to spontaneous nuclei formation must be a function of the thermodynamic variables of the liquid phase (entropy and enthalpy). These properties are expected to vary significantly with temperature unless the liquid's configurational degrees of freedom are "frozen out", due to, a fragile-to-strong transition at 228 K (See Sections 1.3 and 1.4 for discussion). Because the apparent activation energy of crystallization, E_a, is a combination of two temperature dependent activation energies, it may (in principle) show a lack of variation over a limited range of temperatures. Nevertheless, such a case seems to be extremely unlikely, taking into account the wide range of temperatures (nearly 100 K) where the Arrhenius-like temperature dependence of the crystallization time is observed.

Let us now assume that pure ASW is a fragile liquid, i.e. that the temperature dependence of its microscopic relaxation time follows a VFT-like curve suggested in some previous studies[9,10] (see Figure 6.3). Such an assumption would of course contradict the conclusions of the FSC experiments discussed in the previous chapters, where no detectable glass transition endotherm was observed at temperatures consistent with the relaxation time plot in Figure 6.3. However, for the sake of argument, let us assume that the sensitivity of those earlier FSC measurements was not sufficient to detect the glass transition. In short, let us assume that pure ASW undergoes a transition from laboratory

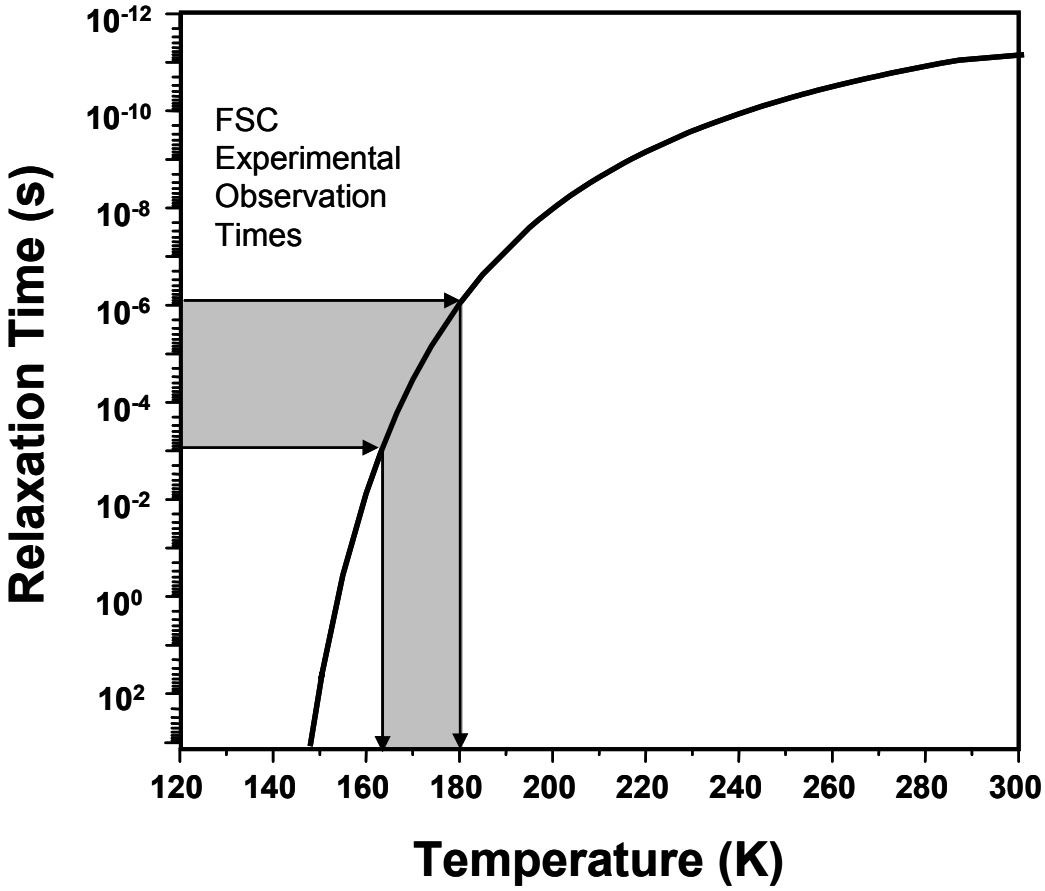

Figure 6.3. Based on the assumption of the continuity hypothesis, when using a heating rate within the range of 10^3 K/s to 10^6 K/s in an FSC experiment, the laboratory glass transition must occur over the range of temperatures from 160 K to 180 K (shaded area).

glass to laboratory supercooled liquid *before* it crystallizes.

Under this assumption, the range of temperatures above which ASW is able to assume the structure and follow the molecular kinetics characteristic of a supercooled liquid, i.e. the temperatures above which the microscopic relaxation time becomes shorter than the experimental time with heating rates from $3 \cdot 10^3$ K/s to $1.6 \cdot 10^6$ K/s, are marked in Figure 6.3 by the shaded area. Above these temperatures, the configurational degrees of freedom of ASW must be effectively "unlocked" prior to the crystallization, and the energy barrier for spontaneous formation of crystalline nuclei *and* for molecular transport from ASW to crystallites would be unaffected by the short observation time of FSC studies. Thus, due to an expected strong dependence of the apparent activation energy of crystallization on temperature, the crystallization kinetics at temperatures between 185 K and 215 K must be distinct from those observed at temperatures between 130 K and 150 K as illustrated by the dashed lines in Figure 6.4. Needless to say, no such deviations from a simple Arrhenius dependence are experimentally observed. Therefore, pure ASW is extremely unlikely to show a fragile-like dependence of its molecular kinetics on temperatures.

In summary, the remarkable result that the complex crystallization kinetics of ASW follows a simple Arrhenius law with similar apparent activation energy in two drastically different temperature ranges (between 130 K and 150 K, and between 185 K and 215 K), once again puts in question the hypothesized high fragility of ASW. Such behavior of

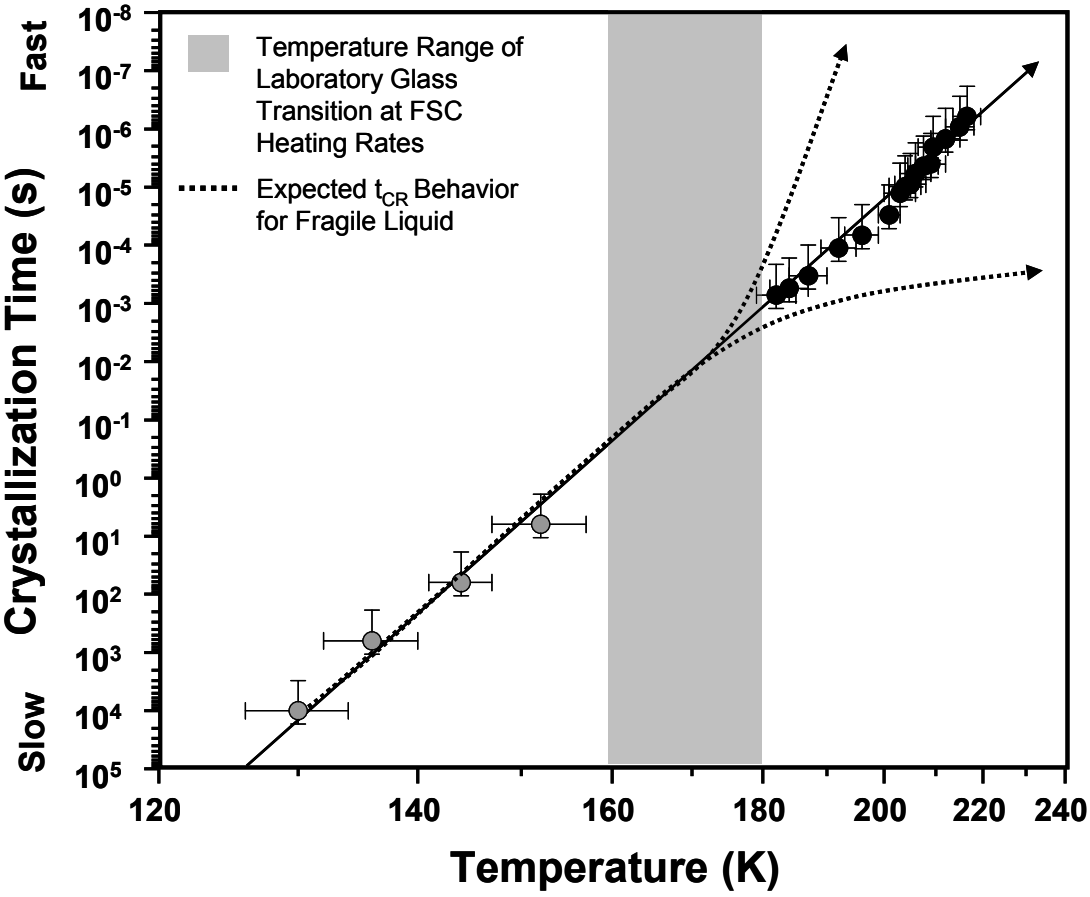

Figure 6.4. Based on the assumption that water is a fragile liquid over the temperature range from cryogenic to ambient, the existence of a glass transition in the range of 160 K to 180 K (shaded area) would cause the crystallization kinetics of ASW at temperatures above 180 K to be distinctly different from those at temperatures below150 K (dashed lines). However, the data maintains a strong Arrhenius dependence over the entire temperature range (solid line); thereby, discrediting the continuity hypothesis.

crystallization kinetics, however, is in perfect agreement with the conjecture that pure ASW undergoes crystallization prior to a glass transition, i.e., that pure ASW is a strong liquid (laboratory glass) at temperatures below 228 K.

6.4 Summary and Afterword

Using variable rate FSC, I have conducted the first ever investigation of the crystallization kinetics of pure ASW in the "No Man's Land" temperature range. The analysis of the observed temperature dependence of the characteristic crystallization time shows that the crystallization kinetics of pure ASW between 185 K and 215 K are essentially the same as those at cryogenic temperatures. This experimental finding provides further basis for a rebuttal of the notion that pure ASW is a fragile liquid over the entire temperature range from cryogenic to ambient[9]. In contrast to this notion, the crystallization kinetics of pure ASW are consistent with the conjecture that a possible fragile-to-strong transition exists at 228 K[11]. In other word, the crystallization rate data reported in this chapter supports the hypothesis that pure ASW is an ice-like, glassy phase at temperatures below 228 K.

In addition to its fundamental value, the question about the kinetic and thermodynamic properties of ASW is of certain applied importance. Current debate on the subject is partially precipitated by the suggestion that ASW at cryogenic temperatures can be used as a model for condensed aqueous system for studies of reactions and dynamics of environmental and biological relevance[12]. The essential rationale for such an experiment is that, due to the hypothesized kinetic and thermodynamic continuity between ambient water and ASW, the result of such studies can be extrapolated from cryogenic to near ambient,

i.e., to the temperatures more relevant for biological and environmental studies. However, according to my FSC studies described in this and previous chapters, a great caution must be exercised when extrapolating the results of experiments with cryogenic ASW to a temperature range near ambient. While the thermodynamic and kinetic continuity would certainly benefit many in the applied areas of research by making it possible to use the entire arsenal of high vacuum surface science techniques in the studies of relevant applied chemistry problems, its existence is unlikely.

References

1. Chonde, M.; Brindza, M.; Sadtchenko, V. *J. Chem. Phys.* 125, 10 (2006).
2. Sack, N. J.; Baragiola, R. A. *Phys. Rev. B* 48, 9973 (1993).
3. Johari, G. P.; Fleissner, G.; Hallbrucker, A.; Mayer, E. *J. Phys. Chem.* 98, 4719 (1994).
4. Lofgren, P.; Ahlstrom, P.; Lausma, J.; Kasemo, B.; Chakarov, D. *Langmuir* 19, 265 (2003).
5. Dohnalek, Z.; Kimmel, G. A.; Ciolli, R. L.; Stevenson, K. P.; Smith, R. S.; Kay, B. D. *J. Chem. Phys.* 112, 5932. (2000), and references therein.
6. Safarik, D. J.; Meyer, R. J.; Mullins, C. B. *J. Chem. Phys.* 118, 4660 (2003).
7. Smith, R. S.; Huang, C.; Wong, E. K. L.; Kay, B. D. *Surf. Sci.* 367, L13 (1996).
8. AK Jena, M. C. *Phase Transformations in Materials* Prentice Hall: Englewood Cliffs, N.J., 1992.
9. Johari, G. P. *J. Chem. Phys.* 105, 7079 (1996).
10. Smith, R. S.; Dohnalek, Z.; Kimmel, G. A.; Stevenson, K. P.; Kay, B. D. *Chem. Phys.* 258, 291 (2000), and references therein.
11. Angell, C. A. *Science* 319, 582 (2008).
12. Kay, B. D.; Smith, R. S.; Kimmel, G. A.; Dohnalek, Z.; Ayotte, P.; Stevenson, K. P. *Abstr. Pap. Am. Chem. Soc.* 220, 111 (2000).

Chapter 7: Conclusions and Future Research Projects

Long before the discovery of the "glass transition" of deeply supercooled water, intense scientific debate raged on about the nature and physical properties of water at various temperatures. In addition to its stimulating intellectual challenge, development of a comprehensive physical model of the dynamics and reactions in water at temperatures from cryogenic to ambient is of the utmost practical importance for an array of applied fields such as biochemistry and environmental science. Throughout history, elucidation of many "mysteries" of water, i.e., the development of a consistent picture of water's dynamics and structure at various temperatures, has been hampered by the lack of data on water's thermodynamic and kinetic properties near 228 K, where water demonstrates behavior distinct from other molecular liquids. In the absence of tangible data on the basic thermodynamic and kinetic variables of water (self diffusivity, viscosity, entropy, enthalpy, heat capacity etc.), in the so called "No Man's Land" temperature region of water research (160 K to 228 K), a large number of conflicting conjectures have arisen. The primary contributions to the research in this field of fundamental studies of condensed aqueous phases are summarized immediately below:

1. A new technique, fast scanning calorimetry (FSC), was introduced to the field. This relatively simple, yet versatile, technique was refined and validated in the course of my research activities. Although FSC has been

used briefly in preliminary studies of heat capacity and crystallization of pure and doped amorphous solid water at temperatures near 200 K, the experimental test and instrument development described in this thesis (see Chapter 3), made it possible to refine and validate this technique. Of particular importance are the variable rate studies describe in Chapters 5 and 6, which demonstrate that the FSC technique is capable of providing detailed information on the kinetics of microscopic relaxation and crystallization in water at various temperatures.

2. Based on extensive FSC studies of ASW doped with a variety of molecular impurities, a new hypothesis was introduced to the field. As described in Chapter 4 of this thesis, the vicinal ASW conjecture has a potential to reconcile many seemingly conflicting results from past studies of the dynamics in deeply supercooled water.

3. Surprising similarities between the kinetic and thermodynamic properties of water confined to silica ("hard-wall") nanopores and those of water in cryogenic solutions with acetic acid were discovered. Although not explicitly discussed in Chapter 5, this finding can be interpreted as evidence that the structure and dynamics of water in the solvation shell of chemicals dissolved in the ASW matrix may be fundamentally different from that in

the solvation shell of the same species in dissolved in water at near ambient temperatures.

4. Finally, the first ever studies of crystallization kinetics of pure ASW in the previously inaccessible temperature range from 185 to 215 K were conducted using FSC at heating rates in excess of one million Kelvins per second. The unique crystallization rate data obtained in these studies provided further data for resolution of one of the long standing controversies about the water character (fragile vs. strong) at temperatures below 228 K.

In summary, due to the previously unavailable experimental capabilities, which resulted from the development and refinement of new scientific method, FSC, I was able to make new, original contributions to the field of physical chemistry of the condensed aqueous phase. The primary intellectual merit of the work described in this thesis consists in closing the long-standing gaps in understanding of the basic thermodynamic and kinetic properties of water and aqueous solutions by providing new, relevant data on their properties under conditions of deep supercooling. The broader impact of the research described in this thesis is precipitated by the ubiquitous role that water plays in various biological, environmental, and industrial processes. Further impact of the work arises from the development of the scientific method (FTDS-FSC technique), which can be potentially used in studies of non-aqueous, condensed phase systems.

Although the recent FSC studies reported in this thesis have demonstrated the capabilities of this technique and have already produced an array of exciting results, the method can undergo further development. For example, the potential of the FSC approach in studies of deeply supercooled water and aqueous solutions can be significantly increased by combining it with a spectroscopic technique such as Fourier-Transform Infrared (FTIR). Because FTIR is not a particularly sensitive method, the primary obstacle to the incorporation of vibrational spectroscopy into the existing FSC set up is the microscopic physical dimensions of the ASW sample grown in past experiments on thin filaments. This limitation, however, can be easily overcome by minor modifications to the existing apparatus.

In the past, rapid scanning calorimetry thermograms of ASW were measured using a single thin filament, which acted simultaneously as a heater and a temperature sensor. The thin filament geometry of the FTDS-FSC setup was crucial for the success of FTDS studies of the vaporization kinetics, molecular transport, and reactions in polycrystalline ice near its melting point. The experiments relied on the collision-free desorption of H_2O and reaction products at temperatures up to 273 K, and, thus, required a substrate with a small surface area (thin filament). Unlike previous studies[1-4], the FSC experiments described in this thesis were designed specifically to investigate the properties of ASW at temperatures below 220 K. Thus, the small physical dimensions of the substrate are not a crucial requirement for FSC experiments. In short, in the temperature range from 120 K to 200 K, a *thin foil* can be used in the place of a single microscopic filament.

The thin foil arrangement offers several significant advantages over the thin filament microcalorimeter currently employed in our experiments with ASW films. While still facilitating rapid heating[5] of ASW films, a thin foil calorimeter/substrate is characterized by planar geometry and a high surface area. Thus, unlike ASW or ice films of thin filaments, ASW samples on a thin foil can be interrogated during rapid heating by Reflection Absorption Infrared Spectroscopy (RAIRS)[6].

The experiments described in the preceding chapters of this thesis relied on measurements of the thermodynamics and kinetic properties ASW during rapid heating. Conclusions about variations in the structure of supercooled water and aqueous solutions (or the lack of such) were made on the basis of thermodynamic and kinetic data, which is not direct and requires theoretical models for interpretation. Unlike the thermodynamic or kinetic FSC measurements, vibrational spectroscopy is a much more direct technique for the characterization of the molecular structure of the hydrogen bond network in condensed aqueous phases. Indeed, the RAIRS spectra of ASW, crystalline ice, and/or liquid water are quite distinct and can be combined with the appropriate theoretical analysis in order to elucidate the detailed structure of ASW at various temperatures during rapid heating. Although the conventional RAIRS approach is usually not a time-resolved technique, a RAIRS arrangement can be combined with a step-scan capable FTIR spectrometer in order carry out time-resolved spectroscopic studies of pure ASW at different temperatures during rapid heating. Such direct spectroscopic data will be invaluable for validation and refinement of the FSC results described in Chapters 4-6 of the thesis.

References

1. Chonde, M.; Brindza, M.; Sadtchenko, V. *J. Chem. Phys.* **125**, 10 (2006).
2. Lu, H.; McCartney, S. A.; Sadtchenko, V. *J. Chem. Phys.* **127**, 13 (2007).
3. Lu, H. P.; McCartney, S. A.; Chonde, M.; Smyla, D.; Sadtchenko, V. *J. Chem. Phys.* **125**, 11 (2006).
4. Sadtchenko, V.; Brindza, M.; Chonde, M.; Palmore, B.; Eom, R. *J. Chem. Phys.* **121**, 11980 (2004).
5. Allen, L. H.; Ramanath, G.; Lai, S. L.; Ma, Z.; Lee, S.; Allman, D. D. J.; Fuchs, K. P. *Appl. Phys. Lett.* **64**, 417 (1994).
6. Bradshaw, A. M. S.; E. In Advances in Spectroscopy. Spectroscopy of Surfaces; Hester, R. E.; Clark, R. J. H., Eds.; Wiley: New York, 1988; Vol. 16, pp 413-488.

Biography

Stephanie Anne McCartney was born and raised in Savannah, GA. After graduating with honors from Hershel V. Jenkins High School in 2000, she enrolled at the University of Georgia. Stephanie graduated Cum Laude with Honors in December of 2003 with a BS Chemistry Degree.

In August of 2004, Stephanie began her graduate career at the George Washington University and joined the lab group supervised by Dr. Vlad Sadtchenko. With her accomplishments over the next three years, she earned her Masters of Philosophy in Chemistry and began to publish several papers in the Journal of Chemical Physics. She presented posters on her research at several Gordon Research Conferences and, in December 2007, Stephanie attended the European Science Foundation: Water Interfaces in Physics, Chemistry, and Biology: A Multi-Disciplinary Approach in Obergurgl, Austria, where she gave a short talk and presented a poster on her research. The significance of her work was recognized when Stephanie was named the 2008-2009 ARCS Endowment Scholar.

After graduating with her PhD from GWU, Stephanie hopes to be come a professor at a prestigious university and teach chemistry.

List of Publications and Presentations

Journal Publications

1. McCartney, S. A.; Sadtchenko, V. "Fast Scanning Calorimetry Studies of the Glass Transition in Doped Amorphous Solid Water: Evidence for the Existence of a Unique Vicinal Phase" *J. Chem. Phys*., submitted (02/2009).
2. Lu, H.; McCartney, S. A.; Sadtchenko, V. "H/D Exchange Kinetics in Pure and HCl-Doped Polycrystalline Ice at Temperatures near Its Melting Point: Structure, Chemical Transport, and Phase Transitions at Grain Boundaries" *J. Chem. Phys*., 130, 054501 (2009).
3. Lu, H.; McCartney, S. A.; Sadtchenko, V. "Fast Thermal Desorption Spectroscopy Study of H/D Isotopic Exchange Reaction in Polycrystalline Ice near Its Melting Point" *J. Chem. Phys*., **127**, 184701 (2007).
4. Sadtchenko, V.; Lu, H.; McCartney, S. "Response to "Comment on 'Glass Transition in Pure and Doped Amorphous Solid: An Ultrafast Microcalorimetry Study'"" *J. Chem. Phys.* **127**, 157102 (2007).
5. Lu, H.; McCartney, S. A.; Chonde, M.; Smyla, D.; Sadtchenko, V. "Fast Thermal Desorption Spectroscopy Study of Morphology and Vaporization Kinetics of Polycrystalline Ice Films" *J. Chem. Phys.*, **125**, 044709 (2006).

Conference Presentations

1. "Fast Scanning Calorimetry Studies of Amorphous Solid Water" presented at The George Washington University, Chemistry Department weekly seminar, Washington, DC, December 5, 2008.
2. "Glass Transition Phenomena in Pure and Doped Amorphous Solid Water Films" presented at the Gordon Research Conference: Water and Aqueous Solutions, Holderness, NH, July 27 – August 1, 2008.
3. "Glass Transition Phenomena in Pure and Doped Amorphous Solid Water Films" presented at the European Science Foundation Research Conference: Water Interfaces in Physics, Chemistry, and Biology: A Multi-Disciplinary Approach, Obergurgl, Austria, December 8 – 13, 2007.
4. "Glass Transition Phenomena in Pure and Doped Amorphous Solid Water Films" presented at the Gordon Research Conference: Dynamics at Surfaces, Andover, NH, August 12 – 17, 2007.
5. "Fast Thermal Desorption Spectroscopy Study of Morphology and Vaporization Kinetics of Polycrystalline Ice Films" presented at The George Washington University, Chemistry Department weekly seminar, Washington, DC, November 10, 2006.
6. "Glass Transition in Pure and Doped Amorphous Solid Water: an Ultrafast Microcalorimetry Study" presented at the Gordon Research Conference: Water and Aqueous Solutions, Holderness, NH, July 30 – August 4, 2006.